Innovative structured catalysts susceptible to microwaves for the intensification of chemical processes

Eugenio Meloni

A Palma, Paolo e Martina

UNIVERSITY OF SALERNO

DEPARTMENT OF INDUSTRIAL ENGINEERING

Ph.D. Course in Industrial Engineering
Curriculum in Chemical Engineering - XXXV Cycle

Innovative structured catalysts susceptible to microwaves for the intensification of chemical processes

Supervisor
Prof. Vincenzo Palma

Ph.D. student
Eugenio Meloni

Scientific Referees
Dr. Pluton Pullumbi
Dr. Eng. Federico Brandani

Ph.D. Course Coordinator
Prof. Francesco Donsì

A.A. 2021

Acknowledgments

Arrivati alla fine di questo percorso, è giunto il momento dei ringraziamenti, pochi (come del resto è mia abitudine, purtroppo in alcune occasioni non sono per niente bravo con le parole) ma sentiti.

Le prime parole le spendo per Vincenzo Palma, il mio Prof., che mi ha spronato, convinto, supportato nel raggiungere questo traguardo in età non più giovanissima (ma mi sento più giovane di tanti ragazzi). Il suo esempio quotidiano, la passione che mette nelle cose che fa e che facciamo, il suo continuo chiedersi "perché", mi ha fatto amare "la Ricerca" (con la R maiuscola), che nel nostro caso non è mai fine a se stessa ma ha obiettivi tangibili, volta al raggiungimento di risultati che si toccano con mano. Lo ringrazio per la fiducia che mi dà attraverso il continuo e costante coinvolgimento nelle molteplici attività del laboratorio. Lo ringrazio, soprattutto, per il suo essere presente anche al di fuori della vita lavorativa, con i suoi preziosi consigli.

Un particolare ringraziamento a Federico e Pluton, i miei referees, due splendide persone che ho avuto il piacere di conoscere in questi anni. Le loro imbeccate sono state fondamentali per il raggiungimento di questo obiettivo.

Ringrazio i colleghi ed amici dei laboratori T1 e T3, Daniela, Marco, Antonio R., Concetta, Simona, Giusy, Vincenzo Vaiano, Diana, Antonella, Olga, Emilia, Laura, Giovanni, Antonio C., Giacinto, Liberato. Ognuno di loro mi ha dato tanto, spero di aver contraccambiato almeno in minima parte. Alcuni hanno intrapreso altre esperienze professionali, ma la presenza si avverte sempre.

Ringrazio, naturalmente, i miei genitori, mio fratello Marco con Teresa e Iaia, i miei suoceri, Antonio e Lucia, Andrea, i miei amici storici Marco, Mimmo e Ferdinando, che non mi hanno "preso per pazzo" quando ho comunicato loro che avrei iniziato il percorso del Dottorato di Ricerca.

È arrivato il momento di Palma, che dire. Senza di lei non sarei l'uomo che sono oggi, con i miei pregi e i miei difetti, senza di lei non avrei il continuo stimolo a migliorarmi giorno per giorno per darle tutta la felicità che merita. Grazie per l'amore che mi dimostri, che mi dai quotidianamente nelle piccole cose, anche nei momenti più difficili e complicati. Grazie per aver scelto di credere in noi, per aver scelto di affiancarmi nell'avventura della vita e per aver regalato alla nostra famiglia due gioielli: Paolo e Martina.

Publication list

Palma, V., Barba, D., Cortese, M., Martino, M., Renda S., Meloni, E. (2020) Microwaves and Heterogeneous Catalysis: A Review on Selected Catalytic Processes, *Catalysts*, **10(2), 246**; 1-58, doi:10.3390/catal10020246

Meloni, E., Martino, M., Palma, V. (2020) A Short Review on Ni Based Catalysts and Related Engineering Issues for Methane Steam Reforming, Catalysts, **10, 352**; doi:10.3390/catal10030352

Palma, V., Ruocco, C., Martino, M., Barba, D., Meloni, E. (2020) General catalyst-related issues, *In Current Trends and Future Developments on (Bio-) Membranes in Environmental Applications* (A. Iulianelli and A. Basile Eds), Elsevier, Amsterdam, Chapter 14. doi: 10.1016/B978-0-12-816778-6.00014-X

Palma, V., Cortese, M., Renda, S., Ruocco, C., Martino, M., Meloni, E. (2020) A Review about the Recent Advances in Selected NonThermal Plasma Assisted Solid–Gas Phase Chemical Processes, *Nanomaterials*, **10**, 1596-1652. doi: 10.3390/nano10081596

Meloni, E., Martino, M., Pullumbi, P., Brandani, F., Palma, V. (2021) Intensification of TSA processes using a microwave-assisted regeneration step, *Chem. Eng. Process.*, **160**, 108291. Doi: 10.1016/j.cep.2020.108291

Meloni, E., Martino, M., Ricca, A., Palma, V. (2021) Ultracompact methane steam reforming reactor based on microwaves susceptible structured catalysts for distributed hydrogen production, *Int. J. Hydrogen Energy,* **46**, 13729 – 13747. doi: 10.1016/j.ijhydene.2020.06.299

Martino, M., Ruocco, C., Meloni, E., Pullumbi, P., Palma, V. (2021) Main Hydrogen Production Processes: An Overview. *Catalysts*, **11**, 547. Doi: 10.3390/catal11050547

Renda, S., Cortese, M., Iervolino, G., Martino, M., Meloni, E., Palma, V. (2022) Electrically driven SiC-based structured catalysts for intensified reforming processes, *Catal. Today,* **383**, 31 – 43. doi: 10.1016/j.cattod.2020.11.020

Meloni, E., Martino, M., Iervolino, G., Ruocco, C., Renda, S., Festa, G., Palma, V. (2022) The Route from Green H_2 Production through Bioethanol Reforming to CO_2 Catalytic Conversion: A Review, *Energies*, **15**, 2383. Doi:10.3390/en15072383

Meloni, E., Iervolino, G., Ruocco, C., Renda, S., Festa, G., Martino, M., Palma, V. (2022) Electrified Hydrogen Production from Methane for PEM Fuel Cells Feeding: A Review, *Energies*, **15**, 3588. https://doi.org/10.3390/en15103588

Meloni, E., Martino, M., Pierro, M., Pullumbi, P., Brandani, F., Palma, V. (2022) MW-Assisted Regeneration of 13X Zeolites after N_2O Adsorption from Concentrated Streams: A Process Intensification, *Energies,* **15**, 4119. doi: 10.3390/en15114119

Meloni, E. (2022) Electrification of Chemical Engineering: A New Way to Intensify Chemical Processes, *Energies*, **15**, 5469. Doi: 10.3390/en15155469

Meloni, E., Martino, M., Palma, V. (2022) Microwave assisted steam reforming in a high efficiency catalytic reactor, *Renew. Energy,* **197**, 893 – 901. Doi: 10.1016/j.renene.2022.07.157

Summary

Chapter 1 1
1. Brief Overview on Microwave Chemistry 1
  1.1 Brief Overview on Microwave Chemistry 1
  1.2 The Different Microwave Heating Phenomena............................. 3
  1.3 Microwave Heating Applications in Heterogeneous Catalysis 9
    1.3.1 Microwave Heating Due to the Electric Field...................... 13
    1.3.2 Microwave Heating Due to the Magnetic Field 14
  1.4 New Challenges in the Design of a Microwave Reactor System . 15
Chapter 2 17
2. H_2 production – Methane Steam Reforming 17
  2.1. Hydrogen as a green energy vector 17
  2.2. Hydrogen production methods 18
  2.3. Methane Steam Reforming.. 20
  2.4. Aims of this work 24
Chapter 3 25
3. State of the art.. 25
  3.1. The catalysts for Methane Steam reforming................................ 25
    3.1.1. Monometallic Ni-based powder catalysts............................ 26
    3.1.2. Polymetallic Ni-based powder catalysts.............................. 35
    3.1.3. Deactivation studies... 39
  3.2. Ni-based structured catalysts.. 41
    3.2.1 Micro-structured Catalytic Reactors..................................... 44
    3.2.2 Structured Catalytic Reactors 45
  3.3 MW-assisted reforming processes... 58
Chapter 4 61
4. Experimental 61
  4.1. Catalysts preparation 61
  4.2. Catalysts characterization... 62
    4.2.1 X-ray Fluorescence (XRF) 63
    4.2.2 X-ray Diffraction (XRD)... 63
    4.2.3 Hg-intrusion porosimetry 63
    4.2.4 Scanning Electron Microscopy (SEM)................................ 63
    4.2.5 Ultrasound adherence test... 63
    4.2.6 N_2 physisorption at -196°C.. 64
  4.3. Laboratory plants.. 64
    4.2.1 First lab plant configuration 64
    4.2.2 Second lab plant configuration.. 67
  4.3 Measurements of the temperature profile in the SiC monolith when irradiated by microwaves 69
    4.3.1 SiC monolith radial profile.. 71
    4.3.2 SiC monolith axial profile 71

4.4 MW-assisted catalytic activity tests 71
4.5 Kinetic measurements 73
Chapter 5 76
5 CFD Modelling 76
5.1 CFD modelling of the catalytic reactor for the MW-assisted tests 76
5.1.1 ELECTROMAGNETIC WAVE, FREQUENCY DOMAIN (EMW) 78
5.1.2 LAMINAR FLOW (SPF & SPF2) 79
5.1.3 HEAT TRANSFER IN SOLID (HT) 80
5.2 Validation of the CFD modelling activities 82
Chapter 6 84
6 Results and discussion 84
6.1 Results of catalysts characterization 84
6.2 Results of MW-assisted tests by using the first plant configuration 92
6.3 Results of CFD modelling of the second reactor configuration ... 99
6.3.1 CFD modelling results 99
6.3.2 Validation of the CFD modelling 101
6.4 Results of the MW-assisted catalytic activity tests by using the second plant configuration 105
6.4.1 Evaluation of the kinetic parameters 110
6.5 Comparisons 111
Chapter 7 118
7 Conclusions 118
References 122

Index of Figures

Figure 1: The role of microwave radiation in microwave chemistry [8]....... 3
Figure 2: The effect of an electric field **E** on the dipoles of a polar molecule [8]. 4
Figure 3: *Difference between microwave and conductive heating [8].*......... 8
Figure 4: *Synthetic sketch of the heat transfer pathways in a microwave-assisted heterogeneous catalytic system [8].*.. 9
Figure 5: *Microwaves and solids, (**a**) conductors, (**b**) dielectric lossy materials, (**c**) insulators [8].* 12
Figure 6: *Graph of PtX conversion routes. DME = dimethyl ether. MeOH = methanol [40].*.. 18
Figure 7: *Methane Steam Reforming Process.* 21
Figure 8: *temperature profile in a conventional steam reformer [42].*....... 22
Figure 9: *main disadvantages of the conventional MSR process.* 23
Figure 10: *temperature profile inside a structured catalyst in the conventional (left) and MW-assisted process (right).* 24
Figure 11: *Packing shapes considered in the work of Buwa et al. [63].*..... 42
Figure 12: *Stainless honeycomb monolith [63].*... 46
Figure 13: *two different views of the sample NiWSiC1 prepared for the microwave-assisted methane steam reforming.*.. 62
Figure 14: *first configuration of the experimental plant used for the microwave-assisted methane steam reforming process.*.............................. 64
Figure 15: *magnetron and stainless-steel reactor, (a) with the gas inlet and oulet, (b) with the quartz glass specification, and (c) the SiC monolith placed in the reactor.* 66
Figure 16: *a) reactor configuration; b) magnetron and coupler to the reactor, and c) catalyst NiWSiC1 inside the reactor.*.................................. 67
Figure 17: *(left) second configuration of the lab plant for the MW-assisted catalytic tests, (middle) reactor and magnetron, (right) coupler to magnetron and closing flange.* 68
Figure 18: *Top view of the monolith and highlighted positioning of the optical fibers.*.. 70
Figure 19: *Isometric projection of the SiC monolith. (a) inlet, (b) mid, (c) outlet positions.* 71
Figure 20: *Isometric projection of the SiC monolith. INLET, MID, OUTLET acquisition position (AXIAL).*.. 71
Figure 21: *xy representation of the entire geometry uploaded to the COMSOL Multiphysics software, with the evidence of the SiC monolith inside the reactor (left).*... 77

Figure 22: *NIST properties data summaries of Silicon Carbide* 81
Figure 23: *XRD analysis for the NiWSiC samples.* 84
Figure 24: *Hg-intrusion porosimetry, pore distribution vs pore diameter.*. 86
Figure 25: *Hg-intrusion porosimetry, cumulative volume vs pore diameter.* 87
Figure 26: *N_2 adsorption-desorption isotherms for the structured catalyst NiWSiC for each preparation step.* 88
Figure 27: *porosimetric features of the NiWSiC catalyst after each preparation step, calculated through BJH method.* 89
Figure 28: *SEM image of some frontal channels of the NiWSiC1 sample.* . 89
Figure 29: *SEM images at various magnitudes for the bare SiC monoliths (a and b) and for the NiWSiC1 monolith (c and d).* 90
Figure 30: *SEM image and distribution of elements, as obtained by EDS element mapping, for a NiWSiC1 monolith.* 91
Figure 31: *Weight loss percentage of the prepared washcoated sample.* ... 92
Figure 32: *preliminary microwave-assisted heating test of the catalytic monolith NiWSiC1.* 93
Figure 33: *microwave-assisted catalytic test, detail of the heating phase.* . 94
Figure 34: *results of the microwave-assisted catalytic activity tests (GHSV = 3300 h^{-1}) in terms of a) CH_4 conversion and b) H_2 yield vs temperature*. 95
Figure 35: *effect of GHSV on the microwave-assisted catalytic activity tests for: a) catalyst NiWSiC1 in terms of CH_4 conversion vs temperature, b) catalyst NiWSiC2 in terms of CH_4 conversion vs temperature.* 97
Figure 36: *Electromagnetic field in the whole reactor expressed in V/m. Microwave generator is on the left.* 99
Figure 37: *temperature and velocity field distribution inside the overall system.* 100
Figure 38: *temperature distribution along the SiC monolith during the microwave- assisted heating phase: the curves are parametric in the time.* 101
Figure 39: *Experimental results of T radial profile inside the SiC monolith. Ar flow rate 2 NL/min.* 102
Figure 40: *Experimental results of T radial profile inside the SiC monolith. Ar flow rate 2 NL/min.* 103
Figure 41: *comparison of the modelling (curves) and experimental (dotted points) results.* 104
Figure 42: *Preliminary microwave-assisted heating test of the catalytic monolith NiWSiC1, obtained with two different reactor configurations.* ... 105
Figure 43: *Results of the microwave-assisted catalytic activity tests (GHSV = 5000 h^{-1}) in terms of CH_4 conversion vs temperature for the NiWSiC1 catalyst in two reactor configurations.* 106
Figure 44: *Results of the microwave-assisted catalytic activity tests (GHSV = 5000 h^{-1}) in terms of H_2 yield vs temperature for the NiWSiC1 catalyst in two reactor configurations.* 107

Figure 45: *Microwave power (PMW) vs temperature during the catalytic activity tests performed in the old and new reactor configuration, 5000* h^{-1}. 108
Figure 46: *energy efficiency for the MW-assisted steam reforming by using the new and the old reactor configuration.* 109
Figure 47: *Comparison of the experimental and kinetic model results for the structured catalyst NiWSiC1, GHSV = 3300* h^{-1}. 110

Index of Tables

Table 1: summary of preparation procedures and operative conditions used in monometallic catalysts and related publications. 31
Table 2: summary of preparation procedures and operative conditions used in polymetallic catalysts and related publications. 37
Table 3: main performances of the packed bed reactors and of the catalysts supported on metallic carriers. 50
Table 4: Summary of the main performance of the catalysts supported on ceramic carriers. 57
Table 5: geometric characteristics of the bare monoliths used for the preparation of the structured catalysts. 61
Table 6: Test performed for the thermal characterization of the system. 70
Table 7: operating conditions of the microwave-assisted catalytic activity tests 73
Table 8: Crystallite sizes as calculated by XRD analysis. 85
Table 9: Chemical composition (wt%) and textural properties. 85
Table 10: energy consumption among the microwave-assisted steam reforming and different kinds of electrolysers for H_2 production. 98
Table 11: comparison between modelling and experimental results in terms of temperature of the SiC monolith. 104
Table 12: Kinetic parameters for the structured catalyst. 110
Table 13: comparison of different Ni-based structured catalysts performance in MSR. 111
Table 14: comparison of different Ni-based catalysts performance in electrified reforming processes... 112
Table 15: energy consumption among the microwave-assisted steam reforming and different kinds of electrolysers for H_2 production. 115

Index of Equations

(Equation 1).. 4
(Equation 2).. 4
(*Equation 3*).. 5
(*Equation 4*).. 5
(*Equation 5*).. 5
(*Equation 6*).. 5
(*Equation 7*).. 5
(*Equation 8*).. 6
(*Equation 9*).. 6
(*Equation 10*).. 6
(*Equation 11*).. 6
(*Equation 12*).. 7
(*Equation 13*).. 7
(*Equation 14*).. 7
(*Equation 15*).. 13
(*Equation 16*).. 19
(*Equation 17*).. 19
(*Equation 18*).. 20
(*Equation 19*).. 20
(*Equation 20*).. 63
(*Equation 21*).. 72
(*Equation 22*).. 72
(*Equation 23*).. 72
(*Equation 24*).. 72
(*Equation 25*).. 73
(*Equation 26*).. 73
(*Equation 27*).. 74
(*Equation 28*).. 74
(*Equation 29*).. 74
(*Equation 30*).. 74
(*Equation 31*).. 74
(*Equation 32*).. 78
(*Equation 33*).. 78
(*Equation 34*).. 78
(*Equation 35*).. 79
(*Equation 36*).. 79
(*Equation 37*).. 79
(*Equation 38*).. 79
(*Equation 39*).. 79
(*Equation 40*).. 79
(*Equation 41*).. 79

(*Equation 42*) 80
(*Equation 43*) 80
(*Equation 44*) 80
(*Equation 45*) 80
(*Equation 46*) 80
(*Equation 47*) 80
(*Equation 48*) 81

ABSTRACT

Since the late 1980s, the scientific community has been attracted to microwave (MW) energy as an alternative method of heating, due to its peculiarity to be a volumetric process in which heat is generated within the material itself, and, consequently, it can be very rapid and selective. Application of the MW heating technique to a chemical process can lead to both a reduction in processing time as well as an increase in the production rate due to chemical reactions enhancing, so resulting in energy saving. The synthesis and sintering of materials by means of MW radiation has been used for more than 20 years, while future challenges will be, among others, the intensification of existing chemical processes aiming at achieving lower greenhouse gas (e.g., CO_2) emissions. A natural choice in such efforts would be the combination of catalysis and MW radiation, but the selection of the proper material is fundamental for having a successful MW-assisted heterogeneous catalytic reaction/process.

In this Ph.D. thesis the feasibility to intensify chemical processes by using MWs has been investigated. As a reference case for the endothermic reactions, the methane steam reforming (MSR) process has been studied. The main critical issue of the methane reforming reactions is represented by the enormous thermal duty required for the feed heating and for the reaction endothermicity, so involving a very high temperature heating medium ($T > 1100°C$) as well as special steels for the heat transfer to the catalyst. Nevertheless, the heat transfer process is the rate limiting step, corresponding to very large reactor volume and very slow transient behavior. In addition, the thermal constrains of this system limit the maximum temperature achievable in the catalytic bed, and consequently the hydrocarbons conversion is usually lower than 85%. This complexity results in high fixed and operative costs, and, in turn, in a reduction of the overall process efficiency.

In order to overcome the previously discussed critical issues of the reforming reactor, the application of a structured catalyst susceptible to microwaves aims to realize the direct heating of the catalyst due to microwave radiation. In this way, it could be possible to remove the rate limiting step of the heat transfer and the related negative drawbacks. The possibility to fast and directly provide the heat inside the catalytic volume allows to realize a simpler reactor design, a dramatic reduction of the reaction volume, shorter start-up times and the use of cheaper materials. In particular, by selecting the catalyst's carrier with the right chemical-physical

properties, in terms of MW-loss factor and thermal conductivity, a very uniform temperature profile could be achieved, resulting in a more effective and selective exploiting of catalyst surface, minimizing the catalyst mass, making the system more attractive in terms of cost and compactness. In this Ph.D. thesis the material constituting the carrier selected for the preparation of the structured catalysts has been silicon carbide (SiC), due to its well-known dielectric properties.

Two reactor configurations ((i) a simple cylindrical reator, and (ii) an optimized configuration with a restriction of the middle section (where the structured catalyst could be placed) with respect to the inlet and outlet sections, in order to intensify the microwaves electric field in that zone) for performing the MW-assisted reactions have been designed and set up, as well as a dedicated lab plant has been implemented.

The first experimental tests have been devoted to verifying the effective heating of the bare SiC monoliths when exposed to MWs. The results of the tests, performed at various flow rates by feeding N_2 at the fixed power supplied by the microwave generator of 600W and 400 W in the classical and optimized reactor, respectively, evidenced the beneficial effect of the new reactor configuration. In fact, the same monolith can be heated up to the reaction temperature (about 800 °C) with a lower MW power in all the investigated flow rate values.

The optimized reactor configuration was also modelled by using the COMSOL Multyphics software (release 5.6) in order to predict the distribution of the electric field and the temperatures inside the monoliths when the microwave's heating system is on. The developed model was validate by means of properly designed experimental tests. The comparison among the modelled and experimental data evidenced the very good agreement among the former and the latter, mainly in terms of temperature distribution inside the SiC monolith.

Regarding the catalytic activity tests, starting from previous studies, in which SiC was used as catalyst carrier both in endothermic reactions for its high thermal conductivity and in MW-assisted soot oxidation for its good dielectric properties, the structured catalysts were prepared by depositing a CeO_2-Al_2O_3 washcoat and Ni as active species on commercial SiC monoliths. In particular, two different Ni-based catalysts, differing from each other by the Ni loading (7 and 15 wt% with respect to the washcoat) were prepared, characterized and tested in the MW-assisted methane steam reforming reaction by using the two reactor configurations. The catalytic activity tests were performed by supplying a feeding stream with a Steam/Carbon ratio of 3 and Nitrogen/Carbon ratio of 3, at gas hourly space velocities (GHSV) of 3300 and 5000 h^{-1} (calculated as the ratio between the volumetric flow rate and the overall volume, included the monolith). The results highlighted how the optimized reactor configuration positively influenced the system performance: higher both CH_4 conversion and H_2 yield may be obtained. In fact, with the new reactor configuration, the catalyst with the lower Ni loading approaches the CH_4 conversion thermodynamic equilibrium at about 750°C, showing, in whatever case, a CH_4 conversion higher than 80% for temperature higher than 700°C. The same catalyst has shown a significantly lower both CH_4 conversion and H_2 yield in the tests performed in the old reactor configuration. In particular, this catalyst was not able to approach the thermodynamic equilibrium values in all the investigated temperature range.

Moreover, the energy efficiency of the MW-assisted MSR performed in the new reactor was of about 73% with an energy consumption of 2.5 kWh/Nm^3 of produced H_2. The same data obtained by using the old reactor configuration were 50% and 3.8 kWh/Nm^3 of produced H_2. In particular, it is very important to note that, besides the intrinsic energy efficiency of the magnetron (about 50-60%), the developed MW-assisted high efficiency catalytic reactor is able to allow an energy consumption (2.5 kWh/Nm^3H_2) very close to the one of the best resistive MSR (2 kWh/Nm^3H_2). This result is noteworthy since the latter process is not affected by any intrinsic energy losses (the catalyst is directly heated through Joule effect, without any other devices for energy generation). Therefore, when driven by renewable electricity, the proposed reactor configuration promises a high potential to address the decarbonization challenge in the near-term future.

INTRODUCTION

Even if for more than twenty years Process Intensification (PI) has been only identified as a kind of technological "toolbox" containing some spectacular examples of process improvement, it is one of the most important areas of progress for modern chemical engineering [1]. In 2009, Van Gerven and Stankiewicz [2] proposed a fundamental view on PI, with the definition of four basic principles and four domains, which must be considered if the aim is the intensification of a chemical process: spatial, thermodynamic, functional, and temporal. The thermodynamic domain focuses primarily on energy, and the main question for PI is the way in which a source can transfer energy to a recipient in the required form, in the required amount, at the required moment, and at the required position. Among these, the way of correctly transferring the energy in a process from the source to the recipient was ascribed to the thermodynamic domain, and the main challenges for PI are that energy must be transferred (i) in the right form, (ii) in the required amount, (iii) at the required moment, and (iv) at the required position. The fulfilment of these requirements assures that the energy is used in an optimized way, thus limiting any dissipation losses.

A chemical process is conventionally energized by means of conductive heating with a steam boiler as a typical heat source. Nevertheless, a large variety of other forms of energy can be applied for PI, including ultrasounds (for reactions or crystal nucleation), light (in photocatalytic processes), electric fields (in extraction or for orientation of molecules), or microwaves (MWs). The microwave (dielectric) heating of materials has been known for a long time, and microwave ovens have been developed from more than 60 years. The studies by Gedye et al. in 1986 and 1988 [3, 4] opened a period of very intensive investigation of the microwave effects on chemical reactions in homogeneous systems. Since then, hundreds of research papers have been published, and research has also expanded toward heterogeneous catalysis and its related chemical processes.

The main critical issue of the methane reforming reactions is represented by the enormous thermal duty required for the feed heating and for the reaction endothermicity, so involving a very high temperature heating medium ($T>1100°C$) as well as special steels for the heat transfer to the catalyst. Nevertheless, the heat transfer process is the rate limiting step, corresponding to very large reactor volume and very slow transient behavior. In addition, the thermal constrains of this system limit the maximum temperature achievable in the catalytic bed, and consequently the hydrocarbons conversion is usually lower than 85%. This complexity results in high fixed and operative costs, and, in turn, in a reduction of the overall process efficiency.

In order to overcome the critical issues of the reforming reactor previously discussed, the application of a structured catalyst susceptible to microwaves aims to realize the direct catalyst microwave heating, removing the rate limiting step of the heat transfer and the related negative drawbacks. The possibility to fast and directly provide the heat inside the catalytic volume allows to realize a simpler reactor design, a dramatic reduction of the reaction volume, shorter start-up times and the use of cheaper materials. In particular, by selecting the catalyst carrier with the right chemical-physical properties, in terms of MW-loss factor and thermal conductivity, a very uniform temperature profile could be achieved, resulting in a more effective and selective exploiting of catalyst surface, minimizing the catalyst mass, making the system more attractive in terms of cost and compactness.

Chapter 1

1. Brief Overview on Microwave Chemistry

1.1 Brief Overview on Microwave Chemistry

Microwave electromagnetic radiation is situated between 300 MHz and 300 GHz, the radio and infrared frequencies, with this corresponding to wavelengths in a vacuum of about 1 m to 1 mm. Current legislation makes the frequencies of 915 MHz, 2.45 GHz, and 5.85 GHz the most commonly available for chemical processes and Industrial Scientific and Medical (ISM) bands, in order to avoid any interference with broadcast and communications bands [1]. The frequency of 2.45 GHz is used as a source of heating commonly found in domestic microwave ovens. In 1946, the melting of a chocolate bar in the pocket of Percy Spencer while he was walking past an open radar waveguide, gave him the idea that powerful interactions between microwave radiation and materials (for example, foods) were possible [5]. Consequently, in 1952 the first commercial microwave oven was developed and patented by the Raytheon Company [6]. Before the advent of microwaves, high frequency induction heating was commonly used, and as an example, the patent for dielectric heating by means of high frequency induction was issued in 1933 [7].

In contrast to communication purposes, in which the microwaves typically have a well-defined wave in terms of frequency, phase, and amplitude in order to carry the information, for heating purposes microwave output power and efficient irradiation apparatus are important factors. In this case, the composition and fabrication of microwave devices are highly different, which calls attention to the combining of various technologies and competences.

MWs are electromagnetic waves and travel at the speed of light in a vacuum. If a material has polar, conducting, and magnetized properties, it can be directly heated by microwaves.

In this sense, the possibility of carrying out chemical reactions using the microwave heating technique has been studied in detail by numerous researchers in many scientific fields over the last twenty years [8]. These efforts have made the use of microwaves in different areas of the chemical field rather common, including organic chemistry, analytical chemistry, biochemistry, polymer chemistry, catalysis, photochemistry, and the inorganic chemistry of materials. The studies carried out directly in industry on the application of microwave radiation have been particularly important, since they have allowed obtaining high-quality microwave-assisted synthesis, even if these processes need further improvements in order to be used for the preparation of significant quantities of high-value chemicals.

In 2014, Horikoshi and Serpone in a minireview on the role of microwaves in heterogeneous catalytic systems [9] proposed the division of microwave chemistry into four main categories, summarized in **Figure 1**. The division was made by analysing the role of microwave radiation in microwave chemistry as follows: (i) a substance is heated directly by microwaves so that, the chemical synthesis can be coupled to some automated robot technology, such as for microwave heating in domestic ovens (operating mode); (ii) microwaves have beneficial effects in green chemistry since they shorten reaction times even in synthesis involving no solvents and catalysts (green chemistry applications); (iii) microwaves enhance the kinetics of many chemical reactions, by varying the microwave frequency and other phenomena (chemical reactions applications); and (iv) microwaves are used not only as a heat source, but also in the manufacturing of different new materials (specific heating). Naturally, this division of the use of microwave radiation in chemistry and catalysis is not exhaustive. In general, heating up by using microwave radiation in microwave chemistry must be investigated by examining the electric and magnetic radiation fields, and in this sense, it is of extreme importance to understand the difference between the heating phenomenon of microwaves and classical heating methods. In this field, there are thousands of studies reporting the use of microwaves as a heat source in chemical reactions, but only a few reports the characteristics of microwave radiation. In the last years some researchers have focused their attention on the specific microwave effects in the field of heterogeneous catalysis, as described in greater detail in the next chapters [9].

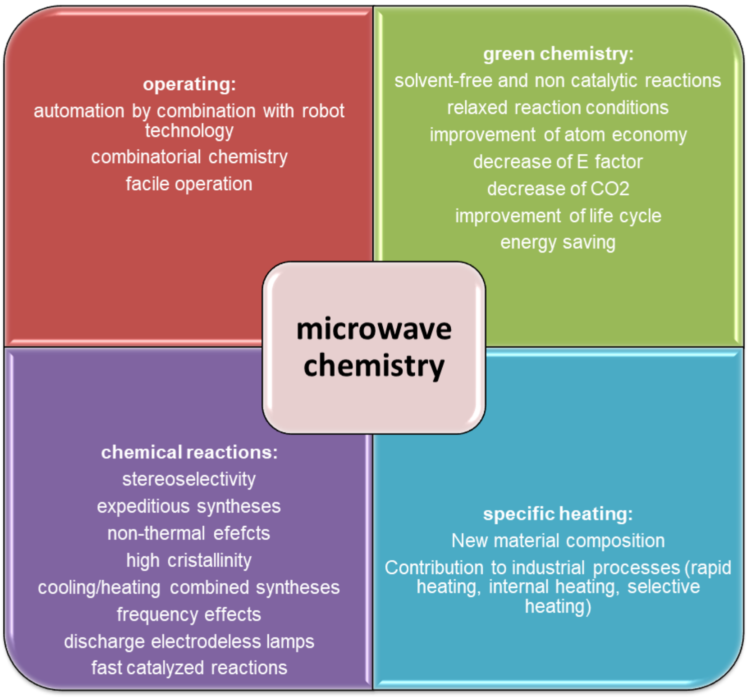

Figure 1: *The role of microwave radiation in microwave chemistry [8].*

1.2 The Different Microwave Heating Phenomena

Since the wavelengths of microwave radiation (1 m to 1 mm) are sensibly different from the ones of the UV range, visible and infrared (from 200 nm to 1000s of nm), the effect that they have on molecules exposed are also different. As a starting point, a useful initial classification to understand how microwaves heat a sample is between liquids and solids. In the first case, when a medium with permanent dipole moments (for example, water) is placed in an external electric field **E**, the dipoles tend to orientate in the **E** direction (Figure 2). If the electric field **E** has an alternating nature, like microwave radiation, the dipoles can rotate with **E**, and, in a similar way, the ions are subjected to rapid translational movements. Due to these rotational or translational movements inside the polar medium, an “internal friction” occurs, thus causing the heating of the medium [10].

Regarding solid materials, depending on their interaction with microwaves, they are usually divided into four categories: (i) materials that reflect microwaves from their surface (metals or graphite): ***perfect conductors***; (ii) materials that are transparent to microwaves (polypropylene or quartz glass): ***insulators***; (iii) materials that absorb microwaves and are heated by them (for example silicon carbide): ***“dielectric lossy materials”***; materials in which magnetic losses occur in the microwave region (for example the case of metal oxides such as ferrites and other magnetic materials): ***“magnetic lossy materials”.***

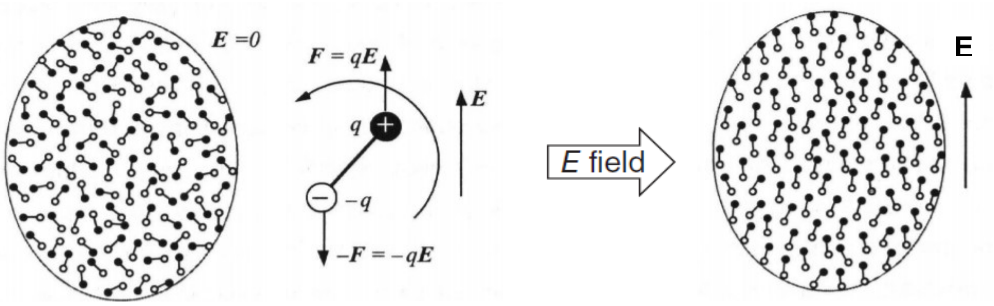

Figure 2: *The effect of an electric field* ***E*** *on the dipoles of a polar molecule [8].*

The first aspect to consider in the understanding of the interaction between a material and microwaves is the definition of two important properties of the material: the complex permittivity, ε^*, and the complex permeability, μ^*.

In a static case, or if the electric field variation is slow enough to not produce losses resulting from the motion of molecules, the ε is real, which effectively means that the alignment of the dipole moments with the electric field is proportional to the electric field. The displacement rate of the charges, which is called a “displacement current” is proportional to the change rate of the electric field in respect to time. In the case of microwave irradiation, the electric field changes rapidly with time, and the complex permittivity, ε^*, and the complex permeability, μ^*, are expressed as follows:

$$\varepsilon^* = \varepsilon' - j\varepsilon'' \qquad \text{(Equation 1)}$$

in which: ε' (the real part), represents the dielectric constant, and is a representation of the ability of the material to store electrical energy, ε'' (the imaginary part) represents the loss factor and reflects the ability of the material to dissipate electrical energy.

$$\mu^* = \mu' - \mathrm{j}\mu'' \qquad \text{(Equation 2)}$$

in which: μ' (the real part) is the amount of magnetic energy stored within the material, μ'' (the imaginary part) represents the amount of magnetic energy which can be converted into thermal energy.

In general, microwave heating is due to three phenomena: (i) dielectric heating, (ii) magnetic heating, and (iii) conduction loss heating [11]. The properties above described are responsible for the first two phenomena, but for the third phenomena, the material electrical conductivity must also be considered. The thermal power P produced per unit volume originating from microwave radiation can be estimated from the following equation:

$$P = \frac{1}{2}\sigma|\mathbf{E}|^2 + \pi f \varepsilon_0 \varepsilon_r''|\mathbf{E}|^2 + \pi f \mu_0 \mu_r''|\mathbf{H}|^2 \qquad (Equation\ 3)$$

in which |**E**| and |**H**| indicate the strength of the microwaves electric and magnetic fields, respectively; σ is the electrical conductivity; f is the frequency of the microwaves; ε_0 is the permittivity in vacuum; ε''_r is the relative dielectric loss factor; μ_0 is the magnetic permeability in vacuum; and μ''_r is the relative magnetic loss.

In the above reported equation, the three terms have the following meaning: the first one is the expression of the conduction loss heating; the second one is the expression of the dielectric loss heating, and the third one is the expression of the magnetic loss heating. These phenomena are described in the following sub-sections.

Moreover, in the case of conductive materials, also the electrical conductivity must be considered, and (Equation 1 becomes:

$$\varepsilon^* = \varepsilon' - j\left(\varepsilon'' + \frac{\sigma}{\omega\varepsilon_0}\right) = \varepsilon' - j\varepsilon''_{eff} \qquad (Equation\ 4)$$

in which σ is the conductivity and ε_0 is the free space permittivity.

Therefore, it is now clear that the microwave heating of materials depends on the electrical, dielectric, and magnetic properties. In this regard, an important parameter to describe the ability of a material to convert electromagnetic energy into heat at a given frequency and temperature is determined by the so-called loss factor tanδ. This loss factor is expressed as follows:

$$\tan\delta = \frac{\varepsilon''}{\varepsilon'} \qquad (Equation\ 5)$$

Another parameter that describes the interaction of a material with microwaves is the magnetic loss tangent ($\tan\delta_\mu$), expressed as follows:

$$\tan\delta_\mu = \frac{\mu''}{\mu'} \qquad (Equation\ 6)$$

The frequency dependence of ε' and ε'' is described by the Debye equation, that describes a dielectric response with a single relaxation time constant. By adding the ohmic losses to the simple Debye equation, the following expression can be written [12]:

$$\varepsilon^* = \varepsilon_\infty + \frac{\varepsilon_s - \varepsilon_\infty}{1 + j\omega\tau} - \frac{j\sigma}{\omega\varepsilon_0} \qquad (Equation\ 7)$$

in which ε_∞ is the dielectric constant at frequencies much higher than the relaxation frequency, $f_r = 1/(2\pi\tau)$, at which the polar molecules do not have time to contribute to the polarization, ε_s is the static dielectric constant, τ is the relaxation time, which is usually determined by an experiment, σ is the conductivity, and ε_0 is the free space permittivity

From (Equation *7*, the dielectric constant and loss factor for a single relaxation time can be written as follows:

$$\varepsilon' = \varepsilon_\infty + \frac{(\varepsilon_s - \varepsilon_\infty)}{1 + \omega^2\tau^2} \qquad (Equation\ 8)$$

$$\varepsilon'' = \frac{(\varepsilon_s - \varepsilon_\infty)\omega\tau}{(1 + \omega^2\tau^2)} + \frac{\sigma}{\omega\varepsilon_0} \qquad (Equation\ 9)$$

in which ε_s is the static dielectric constant, ε_∞ is the high frequency constant, ω is the angular frequency ($\omega = 2\pi f$), τ is the relaxation time characterizing the rate of build-up and decay of polarization, σ is the conductivity, and ε_0 is the free space permittivity. Debye described the simplest form of the relaxation rate for independent molecular dipoles suspended in a viscous medium. In this case, the dipoles are free to adopt any orientation in the absence of an electric field [12]. When the molecular dipoles in the fluctuation reach a state in which the net dipole density is zero, each individual dipole has the same rotation speed depending on the viscosity, η, of the medium. In this case the rotation speed influences the relaxation time of the dipole density fluctuation [13]. The relaxation time of a molecular dipole with an effective length a can be expressed as follows:

$$\tau \propto \frac{\eta a^3}{k_B T} \qquad (Equation\ 10)$$

in which η is the viscosity of the medium, a is the effective length of the molecular dipole, k_B is the Boltzmann constant, and T is the temperature [13].

From (Equation *10*, the dependence of the relaxation time from the viscosity of the medium and the dimension of the molecular dipole is evident: a high viscosity of the medium, or a big molecular dipole, imply a slow rotation speed and a consequent slow relaxation of a fluctuation. The result is a net dipole moment.

For an ideal solid in which each dipole has several equilibrium positions, the Boltzmann statistics can be used for the calculation of the relationship between τ and a dielectric constant [1]:

$$\tau = \frac{e^{\frac{U_a}{k_B T}}(\varepsilon_s + 2)}{\eta(\varepsilon_\infty + 2)} \qquad (Equation\ 11)$$

in which ε_s is the static dielectric constant, ε_∞ is the high frequency constant, η is the viscosity of the medium, k_B is the Boltzmann constant, T is the temperature, $\mathbf{U_a}$ is the potential barrier separating dipole positions.

Once having defined the main characteristics of the microwave heating, one more important parameter must be introduced: the penetration depth. This parameter (D_p) is defined as the depth where the microwave power drops to e^{-1} (about 37%) of the initial value. If the microwaves penetration depth is not high, even if a material has a high dielectric loss, the heating efficiency is sometimes low. In general, D_p can be estimated as follows [9]:

(*Equation 12*)

$$D_p = \frac{1}{2\omega}\left(\frac{2}{\mu'\mu_0\varepsilon_0\varepsilon'}\right)^{\frac{1}{2}}\left[\left(1+\left(\frac{\varepsilon''_{eff}}{\varepsilon'}\right)^2\right)^{\frac{1}{2}}-1\right]^{\frac{-1}{2}}$$

In terms of the free space wavelength, if μ’ = 1, (Equation *12*) can be expressed as

(*Equation 13*)

$$D_p = \frac{\lambda}{2\pi(2\varepsilon')^{\frac{1}{2}}}\left[\left(1+\left(\frac{\varepsilon''_{eff}}{\varepsilon'}\right)^2\right)^{\frac{1}{2}}-1\right]^{\frac{-1}{2}}$$

where λ is the wavelength of the radiation, λ (2.45 GHz) = 12.24 cm in vacuum. From the above reported equation, it is evident that the penetration depth, besides depending on the frequency, changes with an increase in temperature, because the dielectric constant and the dielectric loss, both dependent from the temperature, are present in the equation [5].

For example, in the case of water, at 25 °C, the penetration depth is about 1.8 cm, at 50 °C it increases to 3.1 cm, and at 90 °C, it is 5.4 cm [14]. The penetration depth of the microwaves into almost all nonpolar solvents is very deep when compared to polar solvents. On the other hand, if ions are added to water, the penetration depth then decreases, since dielectric loss increases depending on the conductivity σ, as evident from (Equation *4*. For example, Horikoshi et al. studied the microwave-assisted heating (2.45 GHz) characteristics of aqueous electrolyte solutions (NaCl, KCl, $CaCl_2$, $NaBF_4$, and NaBr) of varying concentrations in ultrapure water [15]. In their work, they reported a diagram in which the penetration depth vs temperature is have shown for an ultrapure water sample containing NaCl at various concentrations. From this diagram, it is possible to observe that when NaCl (0.25M) is added to pure water, the penetration depth into this saline solution changes from 1.8 cm (pure water) to 0.5 cm at ambient temperature [15]. A vigorous stirring is mandatory in the case of ions containing solutions, to avoid the hotspots at the surface of the reactor generated by microwave heating [5].

In the case of low loss dielectric materials, characterized by ratios $\varepsilon''_{eff}/\varepsilon' < 1$, D_p can be described as follows:

(*Equation 14*)

$$D_p = \frac{\lambda}{2\pi}\frac{\sqrt{\varepsilon'}}{\varepsilon''_{eff}}$$

The increase of the frequency results in the penetration depth decrease [16]. At a fixed frequency, a low penetration depth is a characteristic for a material with a high capability to convert the microwave energy into heat, while a large penetration depth can be observed in materials with low loss factors. Under certain conditions, some materials, such as quartz glasses, characterized by low loss factors, have a very large penetration depth, and are passed through by microwaves (these materials are transparent to microwaves) [16]. On the other hand, when the penetration depth is much smaller than the sample dimension, penetration of microwave energy will be limited, thus making uniform heating impossible. The processed substance can be heated effectively by microwaves when the penetration depths are correspondingly comparable to the sample dimensions.

Metals reflect the electromagnetic waves, and in the case of microwaves, they reflect most of them when they are irradiated [5]. An important effect occurring in metals is called *skin effect*, in which an alternating electric current is distributed in such a way that near the surface (*skin*) the current density is larger, and it decreases with the depth increase [5]. The electric current flows starting from the outer surface up to a level identified as skin depth, resulting in the increase of the effective resistance of the conductor at higher frequencies where the skin depth is smaller, with the consequent reduction of the effective cross section of the conductor [5]. The alternating current generates a changing magnetic field that induces opposing Eddy currents, responsible of the skin effect [5].

In conclusion, an optimal microwave heating is obtained by studying the heating efficiency and the penetration depth of microwaves into a substance. It is now clear how microwave heating is fundamentally different from the conventional conduction-based heating, since when microwaves penetrate the material to supply energy, heat is generated in the whole volume and "volumetric heating" occurs (Figure 3). Volumetric heating minimizes the processing time, lowers the consumption of power and improves the diffusion rate: microwave heating is attractive from the PI point of view [17].

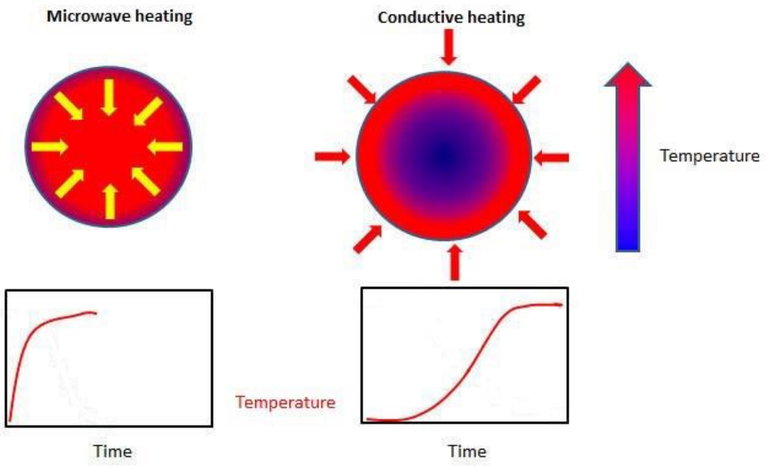

Figure 3: *Difference between microwave and conductive heating [8].*

1.3 Microwave Heating Applications in Heterogeneous Catalysis

Microwave heating or (pre)heating has several applications in almost every field of chemistry, due to the advantages that this technology offers compared to traditional heating methods. The main applications of microwave heating are in the attenuation of environmental pollution, medical uses, food processing, agriculture, ink and paint industry, and wood treatments [18]. Regarding material processing and microwave chemistry, microwave heating is applied to organic and analytical chemistry, biochemistry, catalysis, photochemistry, inorganic materials, and metal chemistry [18].

In the field of organic synthesis, the use of microwaves as a heating medium has increased in recent years, due to the reported observation of large accelerations in reaction rate enhancements. In this area, several articles and books have reviewed the studies carried out [9, 10, 19 - 24].

The better performance of the microwave-assisted heterogeneous catalysed reaction systems in terms of reaction rate and selectivity, with respect to the conventional heating methods, has led to an increasing amount of attention of the scientific community on these processes [9, 25 - 28]. Moreover, microwaves can selectively heat the catalyst, thus resulting in a potential heating medium for high-temperature industrial processes, in which the reaching of the temperature required for the reaction to occur is possible.

A synthetic sketch to explain the heat transfer pathways in a microwave-assisted heterogeneous catalytic system is shown in Figure 4.

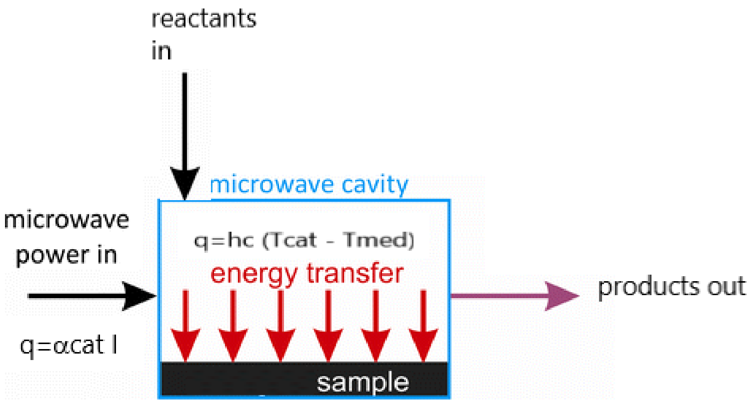

Figure 4: *Synthetic sketch of the heat transfer pathways in a microwave-assisted heterogeneous catalytic system [8].*

The solid catalyst irradiated by microwaves increases its temperature, depending on the magnitude of the radiation intensity (I) and the absorption cross-section of the catalyst material (α_{cat}). In the case of a reaction occurring in a liquid medium, the heating of the solution is dependent on the absorption cross-section (α_{med}) and the intensity of the radiation (I). In addition, the solution will also be heated indirectly by convective heat transport from the solid catalyst to the medium (*hc*). In this last case, if the medium is a good absorber of microwaves, a little temperature difference between the catalyst and the solution ($T_{med} \approx T_{cat}$) occurs, meaning that a little difference between convective and microwave heating is obtained, since the driving force of the reaction is only the temperature. On the contrary, in a gas–solid reaction, $T_{cat} \gg T_{med}$, since the gas is not heated by microwaves ($\alpha_{med} = 0$), and convective heat flow from the catalyst to the surroundings (*hc*) will be significantly less than in a condensed phase reaction. In this case, the heating assisted by microwaves is very selective, and a huge energy saving is possible if compared to convective heating.

In the scheme of Figure 4, the potential advantage is that further reactions are avoided since the rapid activation of the substrate at the hot surface of the catalysts allows for the ejection of the products from the hot surface to the cooler medium due to the imparted kinetic energy [14]. Moreover, especially in the case of a gas-solid reaction, a proper defined set of operating conditions (included catalyst and surrounding temperatures) allows for a higher product selectivity [14].

Despite the presence of such a significant amount of literature, there are still some issues regarding the intrinsic nature of microwave irradiation on chemical reactions and peculiarly on heterogeneous gas-phase catalytic reactions [26]. The main discussion in the scientific community is if the enhancements observed in the presence of microwave irradiation are due to purely thermal effects, that traditionally include inverted temperature gradients, overheating, hot-spots, selective heating, or if they are connected to the so-called specific or non-thermal microwave effects (the influence of the electromagnetic radiation) [27]. Regarding the thermal effects, many research groups investigated the role of the hot-spots in microwave-assisted chemical reactions [27]. The hot spots, that are originated by the inhomogeneity of the field distribution along the sample may have positive or negative effects on the reactions, and they can be detected using several techniques, such as digital cameras or IR thermography. Different factors may influence the hot spots, such as the particle size or the field intensity. The increase in the particle size at a fixed microwave power may result in the increase of the electric discharge, as in the case of Mg particles in benzene. On the other hand, a low field intensity may have a positive effect, as in the reaction for the formation of Grignard reagents, since a high field density may result in solvent decomposition, thus disabling the Grignard reagent formation [27]. The hot spots may also be responsible for a considerable reorganization of the catalyst under microwave irradiations, as reported by Zhang et al. [28]. The authors reported the existence of hot-spots and demonstrated that their temperature was 100 – 150 K higher than the bulk temperature of the catalytic bed. This hypothesis based on the role of the “hot-spots” has been considered for many years as the mechanism responsible for microwave-accelerated heterogeneous gas phase catalytic reactions. However, this well-accepted mechanism has been recently questioned because the formation of hot spots on a catalyst surface can be, as stated, sometimes deleterious to microwave catalytic reactions [28]. The interesting study of Xu et al. [26] reported for the first time that microwaves have an intrinsic catalytic effect, since they allow for the lowering of the apparent activation energy: the authors gave a new interpretation, based on experimental evidence, of the microwave-acceleration of heterogeneous gas-phase catalytic reactions, not only due the presence of “hot-spots”. In the field of the organic synthesis, the studies performed allowed concluding that in the reactions characterized by the electron transfer as the main factor, such as the photochemically assisted reactions, the electromagnetic field may have a positive influence (non-thermal effects) since a higher conversion can be obtained using higher microwave power. The case of the reactions where the main factor is the thermal energy is different: in this case, the increase of the microwave power does not result in reaction enhancement since the microwave power delivers an amount of energy smaller than the thermal energy [27]. Computational methods may be a useful tool since the concepts and properties that influence thermal and non-thermal effects and that cannot be determined experimentally can be calculated separately. For example, the determination of the properties that influence a reaction through thermal effects, such as the polarity of the species, the activation energy, and the enthalpy of the reaction, can allow for the design of reactions that must be improved with the microwaves through the development of a predictive model. Regarding the non-thermal effects, the calculations proved that properties such as the polarizability of transition states and the stabilization of radicals and triplet state influence the reactivity by means of non-thermal effects. In the case of fixed bed flow reactors, an interesting study was carried out by Haneishi et al. [29], whose studies allowed to conclude that the generation of local heating at the contact points between the catalyst particles is a key factor for enhancing fixed-bed flow reactions under microwave irradiation. The authors, in the case of the dehydrogenation of 2-propanol over a magnetite catalyst, reported the generation of local high temperature regions between catalyst particles under microwave heating. The results of their tests highlighted an increase of the reaction rate of 17- (at 250 °C) to 38- (at 200 °C) fold when heated with microwave irradiation rather than an electrical furnace. Moreover, the authors demonstrated the existence of microwave-generated specific local heating by means of a coupled simulation of the electromagnetic fields and heat transfer as well as in situ emission spectroscopy. They reported that the generation of specific high temperature regions occurs at the vicinal contact points of the catalyst particles due to the concentrated microwave electric field, and they directly observed local high temperature regions at the contact points of the particles during the microwave heating of a model silicon carbide spherical material using in situ emission spectroscopy.

Whatever the case, for a complete knowledge of the microwave-assisted catalytic heterogeneous reactions, it is important to understand the fundamental physical processes through which microwaves interact with various catalyst materials.

There are several different classes of heterogeneous catalytic materials, each of which will have different microwave absorption processes. As stated in Section 2, solid materials can be divided into three categories, based on their microwave's absorption behaviour (Figure 5).

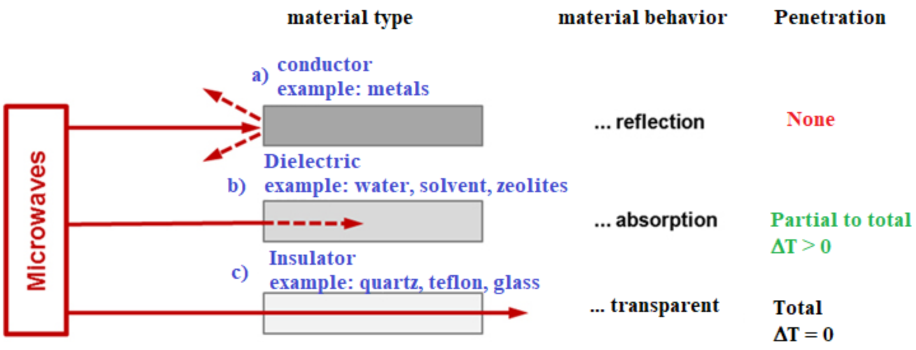

Figure 5: *Microwaves and solids,* ***(a)*** *conductors,* ***(b)*** *dielectric lossy materials,* ***(c)*** *insulators [8].*

A general classification proposed in literature [9], divided the heterogeneous catalysts field into three big areas:

Solid oxide catalysts: this area includes any bulk oxide used to catalyse a reaction at its surface. Typical examples are the simple binary oxides such as SiO_2, Al_2O_3, TiO_2, and ZrO_2, and ternary oxides such as spinels and perovskites. Other materials falling into this area are also porous silicate and alumino-silicate materials such as zeolites and templated mesoporous sieves.

Metals: this area includes all the metal surfaces that are used in catalytic commercial processes. Typical examples are late transition metals such as Ni, Cu, and Ag.

Supported catalysts: this area includes the so-called supported catalyst, defined primarily as an oxide support with an active site deposited on the surface that performs either all or part of the catalytic function. The active site can be an isolated transition metal ion or complex or a metal particle.

All the materials falling into the three areas defined above have different microwave absorption processes, originating from different loss processes. Based on the classification of Figure 5, the choice of the proper material as the catalyst or support is fundamental for having a successful microwave-assisted heterogeneous catalytic reaction/process. An understanding of what kind of loss process, due to the interaction of the electric field component and the magnetic field component with the material, and how it affects chemical reactions on the surface of the catalyst is also important.

1.3.1 Microwave Heating Due to the Electric Field

The electric field component (**E**) of microwaves is responsible for the dielectric heating of a material (heating through dielectric loss). This heating mechanism, in the frequency range of microwaves, is caused by two primary mechanisms, (i) dipolar polarization and (ii) ionic conduction [30]. In the polarization mechanism, the dipole will try to align itself with the field by rotation due to its sensitivity to external electric fields. Under a high frequency electric field, the dipoles are not able to respond to the oscillating field, and in consequence of this phase lag, the dipoles mutually collide as they attempt to follow the field and power is dissipated to generate heat in the material [16].

The dipolar polarization mechanism only concerns polar compounds, for example, water, methanol, ethanol, which possess a permanent dipole moment [31]. Dipolar polarization, $\mathbf{P_d}$, occurs on a timescale of the order of those associated with microwaves. Hence, when a dielectric is subjected to an external electric field of strength E, the polarization is related to the intrinsic properties of the material through the relation expressed as follows [32]:

$$\mathbf{P_d} = \varepsilon_0(\varepsilon_r - 1)\mathbf{E} \qquad \text{(\textit{Equation 15})}$$

where ε_0 is the permittivity in free space and εr is the relative permittivity of the material.

In the conduction mechanism, the movements of any mobile charge carriers back and forth through the material under the influence of the microwave E-field, induces an electric current: heating is so caused by these induced currents that allow for the collisions of charged species with neighbouring molecules or atoms. In some systems, such as the ones in which a conducting material is included in a non-conducting medium, these two mechanisms cannot be separated from each other and work together in microwave heating.

The dielectric heating of a solid sample has different features if compared to that of a liquid sample. In the case of liquid samples, since they have molecules with a high mobility, their heating efficiency is affected by their dielectric parameters. In the solid samples, characterized by crystalline units, the heating is possible only by the motion of these crystalline units, and the heating efficiency may be different even if the same type of solid substance is heated by the same microwave equipment, since solid samples may have a different crystallinity [5]. In solids, the conduction losses are in some cases temperature dependent since they tend to be slight at ambient temperature but can change by increasing the temperature. A typical example is alumina (Al_2O_3) whose dielectric losses are negligibly small ($\sim 10^{-3}$) at ambient temperature but can reach fusion levels (high dielectric loss) in a microwave cavity in a few minutes. This is due to a strong increase in conduction losses associated with the thermal activated migration of electrons from the oxygen's 2p valence band to the aluminium's 3s3p conduction band [5]. Moreover, conduction losses in solids are usually enhanced by defects in materials, that help in reducing the energy needed to generate electrons and holes in the conduction and valence bands, respectively.

1.3.2 Microwave Heating Due to the Magnetic Field

As stated in the previous paragraphs, magnetic loss processes can occur through the interactions of the magnetic moment of the materials with the magnetic field component of the radiation. Such loss processes generate heat with the magnitude of the loss being measured by the real (μ') and imaginary (μ'') component of the permeability and the associated loss tangent. Differently from the electric field heating, there are not many papers ascribing the microwave heating effect to the magnetic field (**H**) component. In the paper by El Khaled et al., some interesting results on studies carried out to verify the effect of the magnetic field in the microwave heating were reported [17]. In particular, (i) the studies of Cheng et al., published in the first years of the twentieth century, proved that some magnetic dielectric materials are more efficiently heated by the microwave magnetic field rather than the electric field; (ii) the studies by Zhiwei et al., published in 2012, gave a relevant importance to the magnetic component of the electromagnetic field and presented its main advantages over electric field heating described earlier in a larger number of publications. Moreover in 2016, Rosa et al. reported how the microwave heating of ferromagnetic powders presents a strong contribution by the **H** field interaction with matter, which, in regions of predominant magnetic field, can result significantly higher than the electric field related contribution [33]. In terms of catalysis, the effect of the **E** and **H** fields on the Pd-catalysed Suzuki–Miyaura coupling reaction for the synthesis of 4-methylbipyridine was investigated by Horikoshi and Serpone [34]. The authors used a microwave apparatus with a single mode cavity TE_{103} that was able to separate the **E** and **H**-field. It was found that the yield dramatically increased in the **H**-field. This was attributed to the generation of by microwave **E**-field that, in this reaction, lead to degradation of the product [34].

Up to recent findings, mechanisms of multiple losses can contribute to the microwave magnetic heating, among which eddy current losses, hysteresis, magnetic resonance, and residual losses are mentioned.

Eddy currents losses occur when induction currents are established in a conducting material by the oscillating magnetic field, which causes resistive heating of the solid. The eddy current density can be expressed as $\mathbf{J} = \sigma\mathbf{E}$, where σ is electric conductivity, and $\mathbf{E}$ is the electric field induced by the alternating $\mathbf{H}$ field.

When magnetic materials are subjected to an alternating magnetic field, the magnetic dipoles will oscillate as the magnetic poles change their polar orientation every cycle. This rapid flipping of the magnetic domains causes considerable friction and heating inside the material: heating due to this oscillation mechanism is known as ***hysteresis loss***. Hysteresis losses occur only in magnetic materials such as ferrous material, steel, nickel, and a few other metals.

Magnetic resonance losses are primarily induced by domain wall resonance and electron spin Resonance (ESR). For example, magnetite (Fe_3O_4) is rapidly heated by microwaves, but this is not the case of hematite (Fe_2O_3) since the latter is not a magnetic material [35]. Moreover, since transition metal oxides (e.g., iron, nickel, and cobalt oxides) have high magnetic losses, they are usually added to induce losses within those solids for which dielectric loss is too small.

Summarizing: (i) microwave heating of a broad range of conductor and semiconductor materials is mainly due to the eddy current loss, (ii) hysteresis loss occurs inside ferrous magnetic materials, (iii) when ferrite and other magnetic materials are exposed to an alternating magnetic field, magnetic resonance loss/residual loss contributes to their induction heating. In some cases, when some conductive magnetic materials (e.g., ferrite materials) are exposed to an alternating magnetic field, the three mechanism of eddy current loss, hysteresis loss and residual loss, can together contribute to their heating [16].

1.4 New Challenges in the Design of a Microwave Reactor System

In the scaling up of a microwave-assisted process, it is important to assure a good microwave flow inside the cavity [36]. In the last years, different research groups compared, also by means of dedicated software simulations, different types of microwave applicators, multi-mode, single-mode (or mono-mode), and traveling-wave microwave reactors (TWR) [37]. In the multi-mode applicators, the microwaves are reflected by the internal walls and by the sample, resulting in a non-homogeneous microwave field and, consequently, in non-uniform heating profile and hot-spots formation [36]. The low field density compared to the high generated microwave power (1000 – 1400 W) is another problem of these applicators, and the result is a weak performance in the case of small-volume samples. Even if they are characterized by these problems, the multi-mode applicators are often used in industry, due to their low cost, simplicity of construction, and versatility. The mono-mode applicators have only one mode, and they generate a standing wave inside the cavity. The sample to irradiate by the microwaves is placed where the electromagnetic field has the maximum intensity. The main limitations of the mono-mode applicators are (i) the limited volume of the sample (max 200 mL) that can be irradiated, (ii) the dependence of the microwave field pattern inside the cavity on frequency changes, as well as on the position and dielectric properties of the heated sample. One advantage of these cavities is that they can provide a higher field strength with less energy consumption [36]. The stated problems of the two above-described applicators make their use critical if controlled chemical reactions must be carried out. Differently from the multi or mono-mode cavities, the TWR, if properly designed so that the microwave field inside the reactor travels in only one direction, can assure a more uniform microwave heating, since it avoids reflections and resonant conditions [36]. In this way, non-uniform electromagnetic interference patterns and non-uniform heating along the reactor are avoided. Microwave chemistry applications have been investigated for more than three decades, and the TWR can be used for a process scale up [37]. One of the newest proposals in this sense is the coaxial structure traveling-wave microwave reactor of Sarabi et al. [37]. Their studies, based also on simulation performed by means of dedicated software, demonstrated that, working at the frequency of 2.45 GHz, the overall structure had a reflection coefficient of −20 dB (≈%1), proving the absence of any standing wave generated along the structure. Furthermore, their simulations demonstrated that also the catalyst loading inside the reactor is important in order to minimize the microwave reflections, and a uniform temperature distribution is assured when the reactor is partially filled with the catalyst. Whatever the case, in order to obtain a successful scale up of a microwave-assisted catalytic process, a multidisciplinary approach, and collaboration among different skills and competencies, such as catalysis, material sciences, electrical and chemical engineering, are necessary.

Further details regarding the challenges in the development of a reactor for MW-assisted tests will be given in the chapter of CFD modelling.

Chapter 2

2. H_2 production – Methane Steam Reforming

2.1. Hydrogen as a green energy vector

The need for an energy transition is widely understood and shared; however, the implications and challenges that must be resolved need a concerted effort. Hydrogen has the potential to be a powerful enabler of this transition, as it offers a clean, sustainable, and flexible option for overcoming multiple obstacles that stand in the way of a resilient and low-carbon economy [38 - 39].

Regarding PI, the European Commission promoted electricity-based processes, known as power-to-X (PtX) processes, to obtain other energy carriers and valuable chemicals through the conversion of the excess electric energy. These technologies include power-to-gas (PtG), power-to-chemicals (PtC), power-to-electricity (PtE), power-to-heat (PtH) and power-to-liquids (PtL), as shown in Figure 6 [40]. The main PtH applications are in the fields of heat generation and/or steam generation in electric boilers replacing natural gas fired boilers. These solutions, which allow for the substitution of natural gas, are low-carbon measures, and are currently also used in large chemical industries, since their flexibility allows for the use and valorisation of the low-cost intermittent power supply from renewables. This connection can be perceived as an element of industrial symbiosis between the chemical industry and the energy sector.

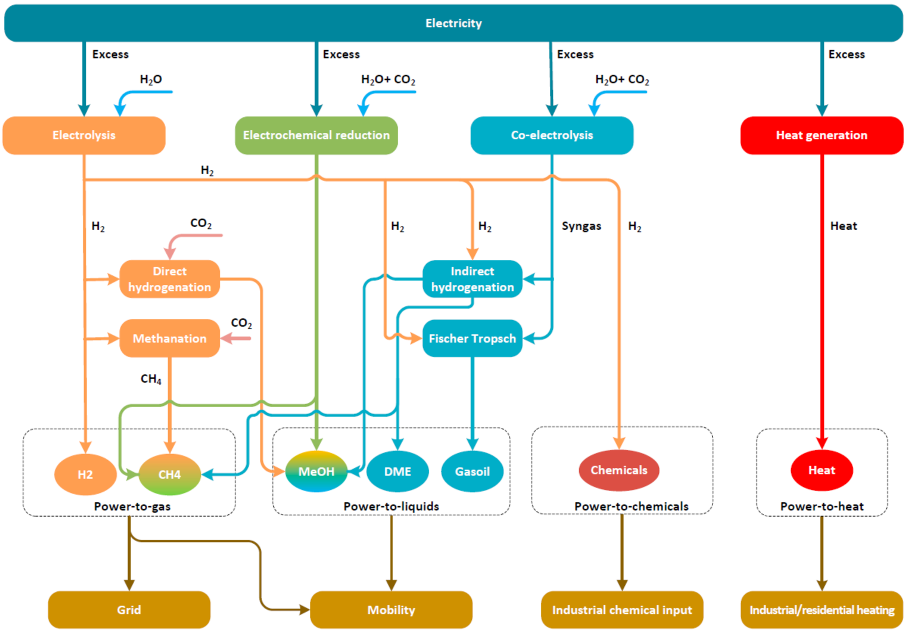

Figure 6: *Graph of PtX conversion routes. DME = dimethyl ether. MeOH = methanol [40].*

Renewable energy sources, such as solar and wind, play a fundamental role in the decarbonization of electricity, and their use is increasing [41]. Their effective use in the chemical industries could have a significant impact on global carbon dioxide emissions, since these industries are large consumers of energy and, consequently, greatly contribute to global greenhouse gas emissions. The electrification of the industry using renewable sources is a possible step toward reducing the carbon footprint of chemicals. However, this ambitious objective can be only reached if clear targets for chemical processes that could have a large impact at the energy-carbon nexus are identified. One of the targets can be the use of a green energy vector. Hydrogen is a potential green energy vector. However, it has a substantial CO_2 footprint since the heating of the reforming processes commonly used for its production is obtained by burning hydrocarbons [42].

2.2. Hydrogen production methods

Hydrogen is an important raw material in the chemical industry, and in the last years its importance as alternative energy carrier has increased due to the depletion of fossil fuels and increasing environmental concerns. An important consideration about hydrogen is that, since it is an energy carrier and not an energy source, it must be first produced, and then it can be used. Hydrogen can be produced through different processes, such as, natural gas or biogas reforming, gasification of coal and biomass, water electrolysis, water splitting by high temperature heat, photo electrolysis and biological processes [43]. Some published statistical researches have speculated that every year a 6% increase or more in hydrogen production will be reached [44]. Currently, among the above cited processes, the conventional large-scale production of hydrogen is mainly obtained by two different processes, both fully developed at industrial level: reforming of fossil fuels and water-electrolysis, even if this last process concurs for only 5% of hydrogen produced [43]. The reforming processes include steam reforming, partial oxidation, dry reforming, and auto-thermal reforming [45]. Among the reforming processes, the Methane Steam Reforming (MSR) technology is the oldest and the most feasible route to convert CH_4 into H_2. It is normally described as the result of the reforming (*Equation 16*) and the Water Gas Shift (WGS) reactions (*Equation 17*),

$$CH_4 + H_2O \leftrightarrows CO + 3H_2 \qquad \Delta H^\circ_{298K} = 206\ \text{kJ/mol} \qquad (\textit{Equation 16})$$

$$CO + H_2O \leftrightarrows CO_2 + H_2 \qquad \Delta H^\circ_{298K} = -41\ \text{kJ/mol} \qquad (\textit{Equation 17})$$

The produced syngas is in a high H_2/CO ratio, 3:1. The high endothermicity of the reforming reaction requires operating temperatures higher than 700°C, and Steam-to-methane ratios of 2.5-3.0 are commonly used in order to reduce coke formation. So, the MSR process is carried out in industrial furnaces and sustained by burning some portion of the natural gas; as a consequence, high temperature operation results in cost disadvantages including the expensive tubular reformer and large energy consumption [46]. The most common catalyst used for MSR is nickel, supported on ceramic oxides or oxides stabilized by hydraulic cement. Although other group VIII metals are active, they have some disadvantages: iron, for example, is oxidized rapidly, cobalt cannot withstand the partial pressures of steam, and the precious metals (rhodium, ruthenium, platinum, and palladium) are too expensive for commercial operation. The commonly used supports include α-alumina, magnesia, calcium aluminate or magnesium aluminate.

As said, MSR is a highly energy-intensive process, and alternative processes to produce synthesis gas include partial oxidation, dry reforming and auto-thermal reforming. Among these alternatives, the catalytic partial oxidation to produce synthesis gas from methane (CPOM) is more energy efficient since it has fast kinetics and it is exothermic, thus avoiding the need of large reactors and large amounts of superheated steam [47]. Moreover, the stoichiometry of the partial oxidation (*Equation 18*) produces a synthesis gas with an H_2/CO ratio of 2:1, which enables its direct utilization for methanol or Fischer-Tropsch synthesis without additional adjustment.

$CH_4 + 1/2\ O_2 \leftrightarrows CO + 2\ H_2 \qquad \Delta H^\circ_{298K} = -\ 35.7\ kJ/mol$ (*Equation 18*)

Nickel is one of the most widely used active phases for CPOM, supported on different oxide substrates (Al_2O_3, CeO_2, La_2O_3, MgO, and ZrO_2) [45].

Hydrogen production from dry reforming of methane has attracted much attention in recent years [48], due to the capability of the process to use two green-house gases (CO_2 and CH_4, (*Equation 19*) to generate valuable feed-stocks with a more desirable H_2/CO for the Fischer-Tropsch synthesis or methanol synthesis to gain high-valuable chemical products.

$CH_4 + CO_2 \leftrightarrows 2CO + 2H_2 \qquad \Delta H^\circ_{298K} = 247\ kJ/mol$ (*Equation 19*)

Nickel catalysts possessing reasonably high catalytic activity and cheap cost have been widely used in methane dry reforming, supported on many metal oxides, such as Al_2O_3, MgO, CeO_2, or La_2O_3 [49]. As reported, Ni-based catalysts in dry reforming are prone to sinter at high temperature and suffer from carbon deposition, which may result in their deactivation during the reaction. Several studies have demonstrated that the threshold nickel nanoparticle size affects the carbon formation, for non-noble metals in fact, the rate of methane dissociation exceeds the rate of the oxidation bringing to the carbon formation on the metal as filaments. The rate of carbon formation is proportional to the nickel particle size so, for a size below 2 nm the carbon formation significantly slows down [50]. In literature, different methods were proposed to suppress sintering of nickel nanoparticles and carbon deposition, including the use of anatase TiO_2 nanosheets with high-energy (001) facets [49] or dealuminated FAU type Y and BEA zeolites [51] as support, or improving dispersion of active metal nanoparticles [52], adding promoters [53]. Some researchers proposed catalysts novel configurations, including Ni-vanadate oxides nanostructures [54], microchannel reactor with thin films of Ni/Al_2O_3 coated on stainless steel [55], or Titanium nitride (TiN) promoted nickel catalysts [56].

Autothermal methane reforming (ATR) is an important process to generate synthesis gas (syngas), a combination gas of CO and H_2, through the combination of adiabatic steam reforming and non-catalytic partial oxidation [57]. Ni catalysts are used for this process, but they encounter the activity loss by sintering and coke formation and deposition, so they must be supported on metal oxides, such as CeO_2 [57].

2.3. Methane Steam Reforming

In the last years, the role of H_2 as energy vector raised over its usual role as an industrial feedstock, primarily for the production of ammonia, methanol, and petroleum refining [58, 59].

Regarding this role, H_2 has many positive features, including high energy density, combustion products without pollutants [60], as well as renewability, making it a potential substitute to fossil fuels [61].

Among the different available processes for hydrogen production, the steam reforming process of fossil fuels seems to be one of the most interesting in terms of energy efficiency and environmental impact. A conventional Steam Reforming process is based on at least 4 main units (Figure 7): fuel hydrodesulphurization, steam reforming (SR) unit, water-gas shift (WGS) unit and several purification stages (for example, PROX, PSA).

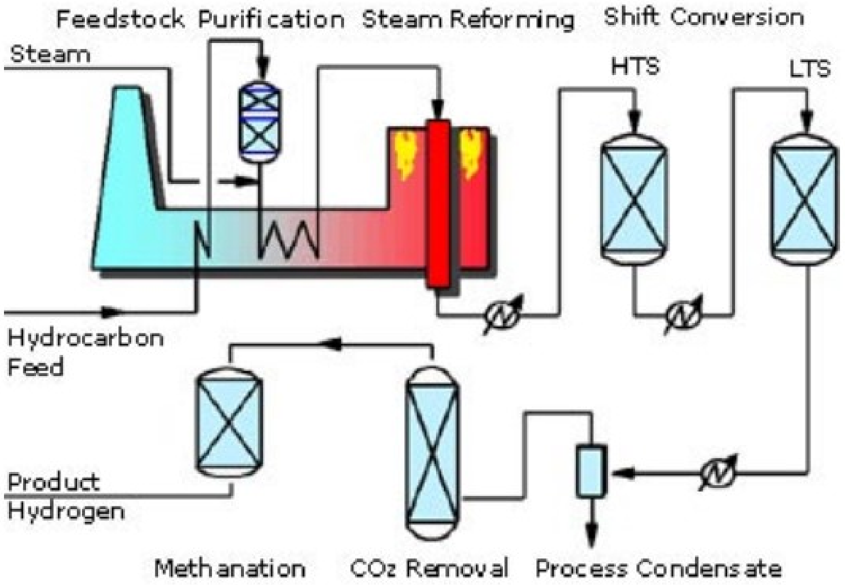

Figure 7: *Methane Steam Reforming Process.*

As mentioned in the previous section, Methane Steam Reforming (MSR) is usually described as the result of the reforming (*Equation 16*) and WGS (*Equation 17*) reactions. The first step of the SMR process involves methane reacting with steam at 750-800°C to produce a synthesis gas (syngas), a mixture primarily made up of hydrogen (H_2) and carbon monoxide (CO). In the second step, the carbon monoxide produced in the first reaction is reacted with steam over a catalyst to form hydrogen and carbon dioxide (CO_2). This process occurs in two stages, consisting of a high temperature shift (HTS) at 350ºC and a low temperature shift (LTS) at 190-210ºC. Hydrogen produced from the MSR process includes small quantities of carbon monoxide, carbon dioxide, and hydrogen sulphide as impurities and, depending on use, may require further purification. The primary steps for purification include:

- **Feedstock purification** – This process removes poisons, including sulphur (S) and chloride (Cl), to increase the life of the downstream steam reforming and other catalysts.
- **Product purification** – In a liquid absorption system, CO_2 is removed. The product gas undergoes a methanation step to remove residual traces of carbon oxides. Newer MSR plants utilize a pressure swing absorption (PSA) unit instead, producing 99.99% pure product hydrogen.

Steam reforming of natural gas offers an efficient, economical, and widely used process for hydrogen production, and provides near- and mid-term energy security and environmental benefits. The efficiency of the steam reforming process is about 65% to 75%, among the highest of current commercially available production methods. Natural gas is a convenient, easy to handle, hydrogen feedstock with a high hydrogen-to-carbon ratio. Anyway, this process has different disadvantages. A typical industrial plant for SR is essentially a large furnace in which more than 100 tubular reactors with a length from 10 up to 14 m are placed, and the gas burners are in such a way to obtain a homogeneous heating temperature among the reactor tubes [62]. The heating medium outside the tubes must reach a temperature higher than 1000°C, otherwise the necessary internal heat flux is not assured, and the temperature profile shown in Figure 8 occurs [63].

Temperature profile in a conventional steam reformer

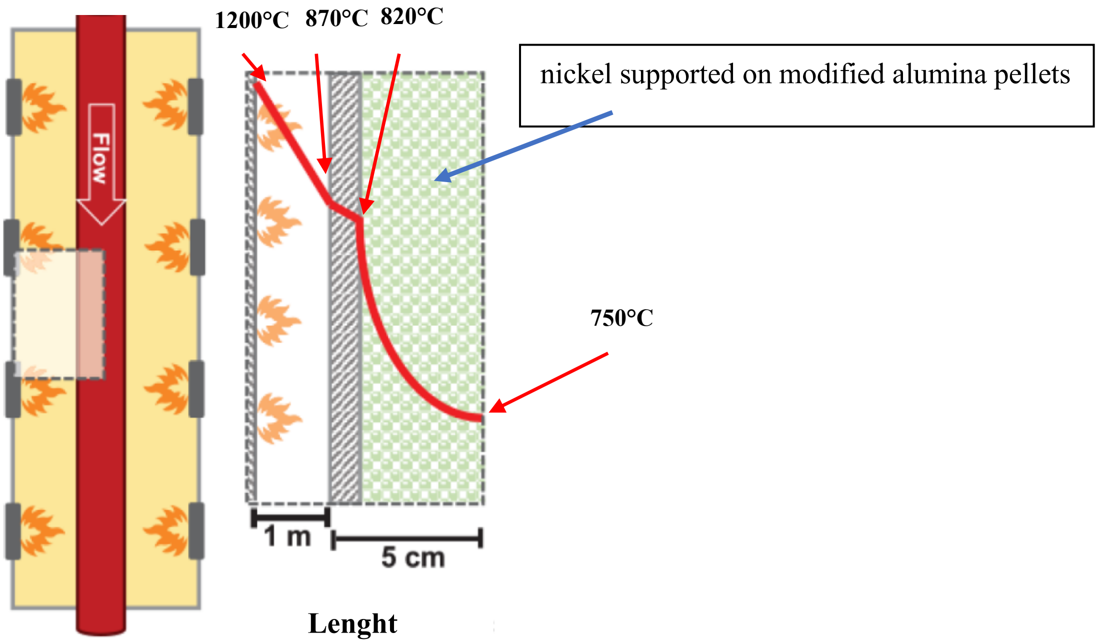

Figure 8: *temperature profile in a conventional steam reformer [42].*

The main critical issue of the methane reforming reactions is represented by the enormous thermal duty required for the feed heating and for the reaction endothermicity, so involving a very high temperature heating medium (T > 1100°C) as well as special steels for the heat transfer to the catalyst. Nevertheless, the heat transfer process is the rate limiting step, corresponding to very large reactor volume and very slow transient behaviour. In addition, the thermal constrains of this system limit the maximum temperature achievable in the catalytic bed, and consequently the hydrocarbons conversion is usually lower than 85%. This complexity results in high fixed and operative costs, and, in turn, in a reduction of the overall process efficiency. The main disadvantages of the conventional MSR process can be summarized in Figure 9.

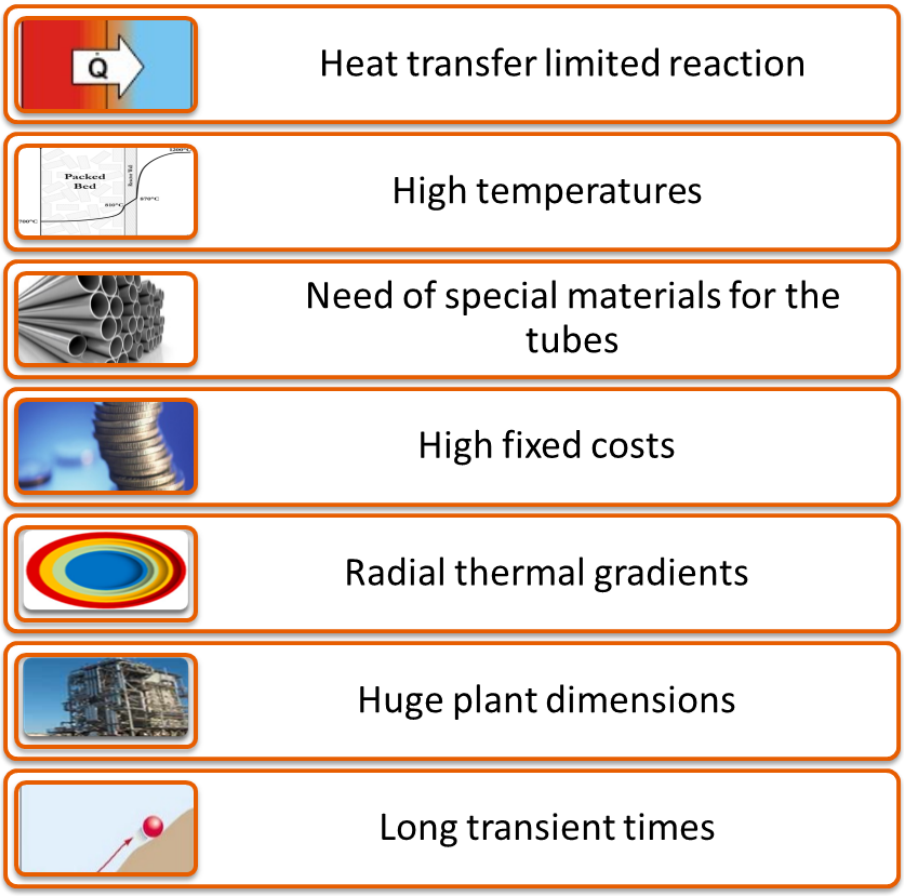

Figure 9: *main disadvantages of the conventional MSR process.*

2.4. Aims of this work

In order to overcome the critical issues of the reforming reactor previously discussed, the application of a structured catalyst susceptible to microwaves aims to realize the direct catalyst microwave heating, removing the rate limiting step of the heat transfer and the related negative drawbacks. The possibility to fast and directly provide the heat inside the catalytic volume allows to realize a simpler reactor design, a dramatic reduction of the reaction volume, shorter start-up times and the use of cheaper materials. In particular, by selecting the catalyst carrier with the right chemical-physical properties, in terms of MW-loss factor and thermal conductivity, a very uniform temperature profile could be achieved, resulting in a more effective and selective exploiting of catalyst surface, minimizing the catalyst mass, making the system more attractive in terms of cost and compactness. In fact, by coupling the above reported features of the catalyst carrier and the peculiarities of the MW heating reported in the previous chapters (selective and direct heating, dependent only by the dielectric properties) the inversion of the heat flow may be obtained with respect to the conventional process (Figure 3), and a different temperature profile inside the catalytic bed (Figure 10).

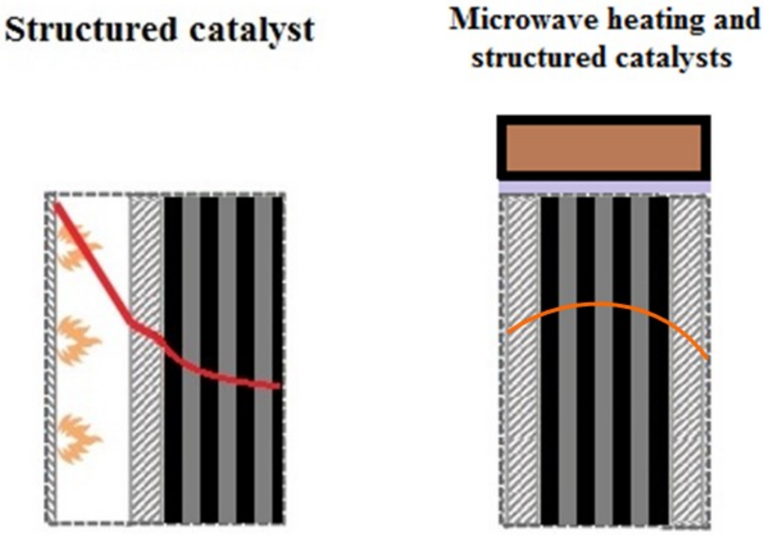

Figure 10: *temperature profile inside a structured catalyst in the conventional (left) and MW-assisted process (right).*

Chapter 3

3. State of the art

3.1. The catalysts for Methane Steam reforming

In general, steam reforming catalysts must meet stringent requirements, such as high activity, reasonable life, good heat transfer, low pressure drop, high thermal stability, and excellent mechanical strength. In addition, the necessity of reducing the costs made the development of methane steam reforming processes operating at low temperature mandatory, so avoiding, for example, the use of special steel alloy. The development of new catalysts with well-defined properties is fundamental in order to reach this objective: in fact, the catalyst must activate methane at low temperature, it must drive its conversion up to equilibrium values at short contact times, and, in addition, it must be resistant to deactivation factors (including carbon formation, which is favoured at low temperature, and preferential oxidation, which occurs at low temperature mainly for Ni catalysts). Nickel is one of the most widely used active phases for CPOM, being supported on different oxide substrates (Al_2O_3, CeO_2, La_2O_3, MgO, and ZrO_2). In the following sub-sections, the recent advances in Ni based catalysts for methane steam reforming are given, also considering the innovative structured catalysts that have been studied.

3.1.1. Monometallic Ni-based powder catalysts

Ali et al. developed a nickel nanoparticle-based catalyst, by dispersing the Ni-nanoparticles on silica/alumina support; the resulting $Ni/SiO_2Al_2O_3$ catalyst have shown good thermal stability, hydrogen selectivity, and coke resistance [64]. The performance of this catalyst, in methane steam reforming reaction (MSR), was also compared to those of a catalyst that was obtained by wet impregnation, with the same chemical composition. The nickel nanoparticle-based catalyst have shown higher CH_4 conversion than the conventionally prepared catalyst, for all the studied temperatures; moreover, the time on stream test have shown the excellent stability of the former. The better performance was attributed to the difference in the physicochemical properties; the nickel-based nanoparticle catalyst was characterized by smaller particle size, better dispersion, and reducibility of the active species. Katheria et al. studied the effect of calcination temperature on the stability and activity of $Ni/MgAl_2O_4$ catalyst in MSR [65]. The results have shown that the catalytic activity increases with the calcination temperature till 850 °C and decreases with a further increase of the temperature. This trend was related to the extension of the metal oxide support solid solution formation and anchoring of the nickel to the support, which increases with the calcination temperature, until 850 °C. The decrease of the activity of the catalyst calcined at 1000 °C was attributed to the formation of nickel aluminate. The stability of the catalysts was also related to the pressure; in general, the increase in pressure from 1 to 10-bar resulted in a decrease in stability, while an increase of the calcination temperature resulted in a decrease of the deactivation rate, due to a decreasing of the mean nickel crystallite size. Rogers et al. reported the preparation of nickel aluminate catalysts [66] by means of Pechini synthesis [67], with the compositions $NiAl_4O_7$, $NiAl_2O_4$, and $Ni_2Al_2O_5$ for dry reforming and the steam reforming of methane. In the Pechini method, the metal precursors are incorporated into the polymeric resin, which reduces differences in the chemical reactivity of the metal ions during the oxide formation, thus minimizing the mixed oxide segregation. The study revealed that reduced $NiAl_2O_4$ and unreduced/reduced $Ni_2Al_2O_5$ show high and stable activity in MSR, and the nickel particles were identified as the active specie. Khani et al. published the results a work in which the activity in MDR, MSR and combined MDR/MSR of three $M/ZnLaAlO_4$ (M = 10%Ni, 3%Pt, 3%Ru) nanocatalysts and 10%Ni/γ-Al_2O_3 were compared [68]. The support was obtained by means of the gel combustion technique, while the catalysts were obtained by means of wet impregnation. The FE-SEM and TEM analysis revealed the nanometric structure of the supports. The MSR catalytic activity tests highlighted the best performance of 3%Ru/$ZnLaAlO_4$, both in terms of CH_4 conversion and coke formation. Fang et al. have shown the effect of the preparation method of the $Y_2Zr_2O_7$ support on the activity of $Ni/Y_2Zr_2O_7$ in the MSR reaction [69]. The $Y_2Zr_2O_7$ pyrochlore supports were prepared by co-precipitation (CP), glycine-nitrate combustion (GNC) and hydrothermal (HT) methods and impregnated with nickel nitrate to prepare the three catalysts. The characterization results revealed that the hydrothermal method provided the highest surface area, while the co-precipitation provided the lowest one. The H_2-TPR results have shown a stronger interaction of nickel with the glycine-nitrate combustion derivate support than with the other two; moreover, this catalyst have shown the highest activity and stability in a time on stream test at 800 °C and 20 atm for 200 h. Thalinger et al. studied the effects of the metal-support interaction, in two Ni/perovskite catalysts (Ni–$La_{0.6}Sr_{0.4}FeO_{3-\delta}$, Ni–$SrTi_{0.7}Fe_{0.3}O_{3-\delta}$, in methane steam reforming and methanation reaction [70]. The catalysts reduction in hydrogen treatment caused the Ni-Fe alloy formation, which is related to the reducibility of the perovskite and much more pronounced with lanthanum-based support. The higher the degree of reducibility of the support, the higher the degree of formation of the Ni-Fe alloy. A comparison of the catalytic activity of these catalysts, with respect to a Ni/Al_2O_3 reference catalyst, in methane steam reforming, have shown similar behaviour between the latter and Ni–$SrTi_{0.7}Fe_{0.3}O_{3-\delta}$, which is characterized by a less degree of alloy formation. On the contrary, the Ni–$La_{0.6}Sr_{0.4}FeO_{3-\delta}$ catalyst have shown a suppressed catalytic performance. Yoo et al. studied the effect of the butyric acid in the preparation of Ni/γ-Al_2O_3 catalysts for steam reforming of natural gas, containing 92 vol % of methane and 8 vol% of ethane [71]. The catalysts were obtained by the impregnation of alumina with a nickel nitrate solution, to which was previously dropped butyric acid, in a molar ratio Ni/butyric acid 0–1. All of the prepared catalysts have shown a mesoporous structure, and they contained a nickel aluminate phase; the nickel dispersion was related to the amount of butyric acid that was used in the preparation, and the higher dispersion was related to the higher methane adsorption capacity. The best performance, in terms of natural gas conversion and hydrogen yield, were obtained with the catalyst that was prepared with a molar ratio Ni/butyric acid of 0.25. Iglesias et al. reported a comparative study on nickel-based catalysts that were supported on ceria and ceria doped with 5 wt % of Zr, Pr or La [72]. The catalysts were obtained by coprecipitation by means of the urea method, and then calcined at three different temperatures (600, 750, and 900 °C). All the doped catalysts have shown a higher oxygen mobility; the Zr-doped have shown the highest oxygen mobility and nickel availability. The catalysts calcined at 600 °C were tested at 600 °C with a water/methane ratio below 3; all the doped catalysts have shown a lower deactivation with respect to the pure ceria supported catalyst, Zr-doped have shown the best performance both with a water/methane ratio of 0.5, to which the hydrogen yield was 23%, and with a water/methane ratio of 3, to which the hydrogen yield was 70%. The catalysts that were calcined at 750 °C have shown the highest methane conversion in all cases. The catalysts that were calcined at 900 °C were tested with a water/methane ratio 1 at 600, 700, and 900 °C showing higher deactivation with respect to ones calcined at 600 °C. Aghayan et al. reported the preparation of a one-dimensional nickel-based catalysts, by template assisted wet-combustion synthesis, for methane steam reforming and methanation reactions [73]. The catalysts were prepared by the infiltration of nickel nitrate and glycine solution in the blocks of nanofibers of mesoporous self-oriented γ-alumina, and subsequent calcined at 400 °C for 30 min. The NiO average particle size was 4 nm, while the alumina surface was covered with the $NiAl_2O_4$ nanolayer. The catalysts have shown outstanding activity and stability in methane steam reforming.

Park et al. reported the preparation of nickel nanoparticles that were supported on $Ni_{0.4}Mg_{0.6}O$ solid solution, by the exsolution method, as catalysts for methane steam reforming [74]. The nickel magnesium solid solution was prepared by the co-precipitation method, while the nickel nanoparticles were obtained during the reduction, with hydrogen, of the solid solution. The activity tests have shown a good stability of the catalysts in 1000 h of time on stream. Zhang et al. reported a comparative study on the use of Ni-based catalysts that were supported on $Y_2B_2O_7$ compounds, in which B was Ti, Sn, Zr, or Ce [75]. The supports were prepared by the coprecipitation method; the ratio between the radius of yttria and the metal ion designed as B decreases with series Ti, Sn, Zr, and Ce, therefore the crystalline structure become increasingly more disordered. The XPS analysis have shown that on the surface of $Ni/Y_2Ti_2O_7$ and $Ni/Y_2Ce_2O_7$, the more abundant active oxygen species are present, being beneficial to the removal of the carbonaceous deposits and keeping the nickel sites free from coking. The H_2-TPR results have shown that the active sites have stronger interaction with the support, in $Ni/Y_2Ti_2O_7$ and $Ni/Y_2Sn_2O_7$ catalysts, resulting in catalysts with higher metallic surface area and better thermal stability. Moreover, the reduction of $Ni/Y_2Sn_2O_7$ catalyst produced the Ni_3Sn_2 alloy, which improved the coking resistance but depressed the activity. Finally, the catalysts were tested in methane steam reforming and methane dry reforming, and the $Ni/Y_2Ti_2O_7$ catalyst have shown the highest activity, stability, and the strongest coking resistance. Chen et al. studied mNi/xLa-Si (m = 7.5, 12.5, 15, 17.5, 22.5) (x = 0, 1, 2, 3, 5, 7) catalysts with a different weight percentage of nickel and lanthanum in a combined carbon dioxide and steam reforming of the methane reaction [76]. The catalysts were prepared via one-step hydrolysis and the condensation of tetraethoxysilane and the inorganic metal salt precursors with the assistance of poly(ethylene glycol) ($M_{av} = 1000$) and ethylene glycol in a water solution of nitric acid. Moreover for a comparison a series of catalysts, with a nickel loading of 17.5% and a lanthanum/silicon ratio of 3, were prepared without the assistance of both poly(ethylene glycol) and ethylene glycol, and a catalyst with a nickel loading of 17.5% and a lanthanum/silicon ratio of 3, was prepared by the incipient impregnation method. The results have shown that the addition of lanthanum had a beneficial effect on the catalytic activity. The catalysts that were prepared with the poly(ethylene glycol) and ethylene glycol assistance, with a nickel loading of 17.5%, have shown an increase of the CH_4 conversion with the lanthanum/silicon ratio, from 0 to 3, and a decreased with the lanthanum/silicon ratio, from 3 to 7. Moreover, the CH_4 conversion, in the case of the catalyst that was prepared by impregnation, with a nickel loading of 17.5% and a lanthanum/silicon ratio, of 3, have shown the lowest CH_4 conversion. These results were related to the nickel particle sizes; thus, an increase of the particle sizes correspond to a lowest CH_4 conversion. A further comparison between these catalysts was also carried out, in terms of TOFs, calculated based on the initial CH_4 conversions at 800 °C and a number of nickel surface per gram of catalyst, obtaining a same trend obtained with the CH_4 conversion. The time on stream tests have shown that the deactivation rate for both CO_2 and CH_4 decreased with the increase in La content in the lanthanum/silicon ratio of 0–3, while the deactivation rates increased for higher ratios. The effect of the different preparation route was also studied; the results have shown that catalysts that were prepared with the poly(ethylene glycol) and ethylene glycol assistance have shown the best performance, in terms of stability. The effect of the nickel loading on the catalytic activity have shown that the CH_4 conversion and the stability of the catalyst increased from 7.5 to 17.5 of Ni wt %, a further increase to 22.5 wt % did not significantly affect the CH_4 conversion. The spent catalysts were analysed by means of X-RAY Diffraction (XRD), Transmission Electron Microscopy (TEM), and Thermo Gravimetric analysis (TGA); the results have shown an increase of the nickel particle size and coke formation for all of the catalysts and highlighted the effect of lanthanum promotion. The crystallite sizes and the coke amount that were recovered by TGA decreased with the lanthanum/silicon ratio from 0 to 3 and increased with the lanthanum/silicon ratio from 3 to 7. These results demonstrated that the catalyst that was prepared with the assistance of poly (ethylene glycol) and ethylene glycol had the best catalytic activity, stability, and coke resistance. Fang et al. studied the effect of rare earth element on the physicochemical properties of the $Ni/Ln_2Ti_2O_7$ (Ln = La, Pr, Sm, and Y) catalysts for methane steam reforming [77]. The supports were prepared by the co-precipitation method, while the catalysts were prepared by impregnation and incipient wetness impregnation methods. The characterization results have shown that changing the element from La and Pr to Sm and Y, the supports transformed from monoclinic layered perovskite to monoclinic layered pyrochlore structure. The Ni active site resulted in being highly dispersed on the pyrochlore supports; moreover, a stronger interaction with the supports was also found; the amount of oxygen vacancies was higher for the pyrochlore supports, thus these catalysts exhibited higher catalytic activity. Among the studied catalysts, the $Ni/Y_2Ti_2O_7$ catalyst exhibited the highest catalytic activity and the best coke-resistance. Iglesias et al. studied the nickel catalysts that were supported on zirconium- doped ceria in the methane steam reforming reaction [78]. The supports were prepared by the coprecipitation method obtaining a solid solution with formula $Ce_{1-x}Zr_XO_{2-\delta}$, in which x was varied from 0 to 35%, while the catalysts were obtained by impregnation. The addition of zirconium enhanced the reducibility of the support and metallic dispersion, but diminished the specific surface area; however, the nickel area was maximized at a zirconium content of 15%. The effect of the nickel loading was also investigated, showing that the best performance was obtained with a loading of 5 wt %, to which the highest metallic surface area corresponded. These results were also confirmed in further studies that were reported from the same group [79]. Sebai et al. studied the use of ammonia, ethylamine, diethyl amine, and triethylamine, as ligands to complex nickel nitrate salt, in the preparation of 5 wt % $NiO/\gamma\text{-}Al_2O_3$ catalysts for methane steam reforming [80]. The catalysts were prepared by incipient wetness impregnation of $\gamma\text{-}Al_2O_3$, via Ni-amines intermediate in-situ complexes formation. The results have shown that the use of the amines complexation reduced the spinel phase formation; moreover, to a larger size of the Ni-amine complex, corresponded to a wider contact area with the support, leading to larger spacing between the resulting nickel particle, which was obtained after the calcination, thus preventing the agglomeration and enhancing the dissociative adsorption of CHx species. Dan et al. reported a study on two alumina supported nickel catalysts, with different pore sizes, 5.4 and 9.0 nm, which were tested in the combined steam and dry reforming of methane [81]. The results have shown that the Ni/Al_2O_3 catalyst with larger pore size was characterized by higher surface area, lower nickel crystallite sizes, higher proportion of stronger catalytic sites for hydrogen adsorption, and higher CO_2 adsorption capacity.

In **Table *1*** the summary of preparation procedures and operating conditions used in monometallic catalysts and related publications is reported.

Table 1: *summary of preparation procedures and operative conditions used in monometallic catalysts and related publications.*

Catalysts (Particle size)	Preparation procedure	Operating conditions MSR	Selected catalyst CH_4 conv./vol% versus temperature/ pressure (Time on stream, deactivation)	Ref.
$Ni/SiO_2Al_2O_3$ (5-8 ± 1.2 nm)	10wt% $SiO_2Al_2O_3$, $NiCl_2*6H_2O$, NaOH, ethylene glycol, $N_2H_4*H_2O$. T=90°C. $T_{calcination}$=900°C.	WHSV=1700 ml/g*h, CH_4/H_2O=1, T=650-900°C.	$X_{CH4}\approx$100%, T=750°C, P=1 bar (50h, 0.41%)	[64]
$Ni/SiO_2Al_2O_3$ (18-20 ± 3.1 nm)	10wt% $SiO_2Al_2O_3$, $Ni(NO_3)_2*6H_2O$, H_2O. $T_{calcination}$=900°C.	WHSV=1700 ml/g*h; CH_4/H_2O=1; T=650-900°C.	$X_{CH4}\approx$75%, T=750°C, P=1 bar (50h, 9.2%) $X_{CH4}\approx$100%, T=900°C, P=1 bar	[64]
$Ni/MgAl_2O_4$ (0.25-0.30 mm)	$MgAl_2O_4$, $Ni(NO_3)_2*6H_2O$, H_2O. $T_{calcination}$=350°C, 500°C, 650°C, 850°C, 1000°C.	WHSV=0.34 g_{cat}h/mol; $CH_4/H_2O/N_2$=1/5/1; T=600°C; P=1-10 bar	X_{CH4}=40-50%, T=600°C, P=1 bar X_{CH4}=35-45%, T=600°C, P=5 bar X_{CH4}=35-45%, T=600°C, P=10 bar	[65]
$NiAl_4O_7$ (8−10 nm), $NiAl_2O_4$ (6−7 nm), $Ni_2Al_2O_5$	$Ni(NO_3)_2*6H_2O$, $Al(NO_3)_3*9H_2O$, ethylene glycol, citric	GHSV=65,500 h^{-1}; H_2O/CH_4N_2 =2.4/1/3.4; T=700°C;	$NiAl_4O_7$ not active $NiAl_2O_4$ X_{CH4}=78%, T=700°C;	[66]

(3−4 nm)	acid, H_2O. $T_{calcination}$=1000°C.	P=1bar	P=1bar (12h, 2%) $Ni_2Al_2O_5$ X_{CH4}=82%, T=700°C, P=1bar (12h, 7%)	
$Ni/ZnLaAlO_4$ (50-60 nm) $Pt/ZnLaAlO_4$ (50-60 nm) $Ru/ZnLaAlO_4$ (≈40 nm) Ni/γ-Al_2O_3 (50-60 nm)	$Ni(NO_3)_2*6H_2O$ or $H_2PtCl_6*6H_2O$ or $Ru(N=O)(NO_3)_3$, $ZnLaAlO_4$ or γ-Al_2O_3, H_2O. $T_{calcination}$=700°C.	GHSV=3500,7000 and 10,500 h^{-1}; $H_2O/CH_4/Ar$=3/1/3; T=600-800°C; P=1 bar	$Ni/ZnLaAlO_4$ X_{CH4}≈72%, T=700°C, P=1bar (10,500h^{-1}, 30h, ≈8%) $Pt/ZnLaAlO_4$, X_{CH4}≈88% X_{CH4}≈72%, T=700°C, P=1bar (10,500h^{-1}, 30h, ≈1%) $Ru/ZnLaAlO_4$ X_{CH4}≈98%, T=700°C, P=1bar (10,500h^{-1}, 30h, ≈0%)	[68]
$Ni/Y_2Zr_2O_7$_x x=HT, CP, GNC	$Ni(NO_3)_2*6H_2O$, $Y_2Zr_2O_7$_x, H_2O. $T_{calcination}$=800°C. x=HT, CP, GNC	WHSV=72,000 mL/h gcat; H_2O/CH_4=2/1; T=550-800°C; P=1, 20 atm	$Ni/Y_2Zr_2O_7$_HT X_{CH4}≈83%, T=800°C, P=1atm (100h, 11%) $Ni/Y_2Zr_2O_7$_CP X_{CH4}≈60%, T=800°C, P=1atm (100h, 15%) $Ni/Y_2Zr_2O_7$_GNC X_{CH4}≈98%, T=800°C, P=1atm (100h, 0%)	[69]

Ni–$La_{0.6}Sr_{0.4}FeO_{3-\delta}$ (50 nm) Ni–$SrTi_{0.7}Fe_{0.3}O_{3-\delta}$ (25 nm)	$Ni(acac)_2$, acetone, $La_{0.6}Sr_{0.4}FeO_{3-\delta}$ or $SrTi_{0.7}Fe_{0.3}O_{3-\delta}$ $T_{calcination}$=600°C.	$H_2O/CH_4=1/1$; T=550-600°C; P=1 bar	Ni–$SrTi_{0.7}Fe_{0.3}O_{3-\delta}$ X_{CH4}≈90%, T=600°C, P=1bar	[70]
Ni/γ-Al_2O_3 (<10 nm)	γ-Al_2O_3, H_2O, $Ni(NO_3)_2$*6H_2O, butyric acid. Ni/butyric acid 0-1 $T_{calcination}$=700°C.	Flow= Natural gas (92 vol% methane and 8 vol% ethane) 5 ml/min, steam (11 ml/min), and nitrogen (18 ml/min).	10Ni/γ-Al_2O_3 Ni/butyric acid=0.25 $X_{natual\ gas}$≈64%, T=550°C (1000min, 0%)	[71]
Ni/$Ce_{0.95}M_{0.05}O_{2-d}$ (M = Zr, Pr, La) (17-35 nm)	$Ce_{0.95}M_{0.05}O_{2-d}$ (M = Zr, Pr, La), H_2O, $Ni(NO_3)_2$*6H_2O. $T_{calcination}$=600, 750, 900°C.	Weight/Flow = 1 g min/Nml), CH_4 (12.5%), H_2O/CH_4 (0.5, 1, 1.5 or 3).	5% Ni/$CeZr_5$ X_{CH4}=72%, T=600°C, R=3. (4h, ≈12%)	[72]
Ni/γ-Al_2O_3 (<50 nm)	γ-Al_2O_3, H_2O, $Ni(NO_3)_2$*6H_2O, glycine. $T_{calcination}$=400°C	WHSV = 45,000–360,000 $scm^3g^{-1}h^{-1}$, $H_2O/CH_4=2/1$, T=650 °C.	CH_4≈10% vol, H_2≈50% vol T=650°C (50h, 0%)	[73]
Ni/$Ni_{0,4}Mg_{0,6}O$ (18-28 nm)	Reduction of $Ni_{0,4}Mg_{0,6}O$ with hydrogen.	WHSV=15, 800 $cm^3g^{-1}h^{-1}$, $H_2O/CH_4=0.5$.	X_{CH4}≈99%, T=800°C. (100h, 0%)	[74]
Ni/$Y_2B_2O_7$ (B=Ti, Sn, Zr, or Ce)	$Ni(NO_3)_2$*6H_2O), H_2O, $Y_2B_2O_7$ (B=Ti, Sn, Zr, or Ce)	WHSV=36, 000 $mLh^{-1}g_{cat}^{-1}$, $H_2O/CH_4=2$	Ni/$Y_2Ti_2O_4$ X_{CH4}≈85%, T=750°C (50h, ≈5%)	[75]

	$T_{calcination}$=800°C.	:1.	Ni/$Y_2Sn_2O_4$ X_{CH4}≈9%, T=750°C (50h, ≈2%) Ni/$Y_2Zr_2O_4$ X_{CH4}≈43%, T=750°C (50h, ≈35%) Ni/$Y_2Ce_2O_4$ X_{CH4}≈65%, T=750°C (50h, ≈5%)	
mNi/xLa-Si (m=7.5,12.5,15,17.5,22.5) (x=0,1.0,2.0,3.0,5.0,7.0) (14-20 nm)	$Ni(NO_3)_2$*$6H_2O$, $La(NO_3)_3$*$6H_2O$, PEG, H_2O, ethylene glycol, nitric acid, TEOS. $T_{calcination}$=800°C.	GHSV=1.584x10^5 mL/g_{cat}h, $CH_4/CO_2/H_2O$=1/0.4/0.8, T=730-830°C, P=1 atm	17.5Ni/3.0La-Si X_{CH4}≈85%, T=800°C (60h, ≈5%)	[76]
Ni/$Ln_2Ti_2O_7$ (Ln = La, Pr, Sm, and Y) (16.6-17.5 nm)	$Ni(NO_3)_2$*$6H_2O$, H_2O, $Ln_2Ti_2O_7$ (Ln = La, Pr, Sm, and Y). $T_{calcination}$=800°C.	WHSV=72,000 mL/gh, H_2O/CH_4=2/1, T=600-800°C, P=1 atm.	Ni/$Y_2Ti_2O_7$ X_{CH4}≈85%, T=800°C (50h, ≈5%)	[77]
yNi/$Ce_{1-X}Zr_XO_{2-\delta}$ (X=0, 0.15, y=2,5,10).	$Ni(NO_3)_2$*$6H_2O$, H_2O, $Ce_{1-X}Zr_XO_{2-\delta}$ (X=0, 0.15). $T_{calcination}$=600°C.	τ=1 mg min/Nml H_2O/CH_4=1/1, T=600°C.	5Ni/$Ce_{0.85}Zr_{0.15}O_{2-\delta}$ X_{CH4}≈70%, T=600°C (4 h)	[78]
Ni/γ-Al_2O_3 (11.4-14.2 nm)	γ-Al_2O_3, $Ni(NO_3)_2$*$6H_2O$, H_2O, amine. Ni/Amine=1/6, Amine= ammonia, ethylamine, diethylamine, triethylamine.	GHSV= 24x10^3 mL/g_{cat} h, H_2O/CH_4=3/1, T=500-800°C,	5Ni/γ-Al_2O_3 amine= diethylamine X_{CH4}≈90%, T=700°C (500min, ≈0%)	[80]
Ni/Al_2O_3	Al_2O_3,	GHSV=	10wt%	[81]

(6-12 nm)	$Ni(NO_3)_2*6H_2O$, H_2O. $T_{calcination}$=550°C.	100 mL/min, CH_4/CO_2=1/0.48, H_2O/CH_4=1.2/0.48, 3.5/0.48, 6.1/0.48. T=600-700°C.	Ni/Al_2O_3, X_{CH4}≈99%, T=700°C (20h, ≈0%)	

3.1.2. Polymetallic Ni-based powder catalysts

Nickel-based catalysts, although widely used in reforming processes, are less active than noble metal-based catalysts and more prone to deactivation [43]. An effective strategy for improving the performance of the nickel-based catalysts resides in the use of promoters [82]. Carbon formation can be avoid when the CO_2 concentration in nickel crystals is lower than that at the equilibrium, hence decreasing the steady state carbon activity, which is achievable by enhancing the adsorption of steam or CO_2, enhancing the rate of the surface reaction, or decreasing the rate and degree of methane activation and dissociation [83]. The use of promoters, which can improve the coke resistance of nickel-based catalysts in reforming processes, is a possible way to achieve these effects [84]. Promoters can also affect the reducibility and dispersion of nickel particles, by acting as structural promoters [85] as well as affecting the segregation in oxidation-reduction processes [86]. The promoters are usually metallic ions added to the active components, which can induce electronic changes or crystal structure modification [87]. In this section, a selection of the latest work on the effect of adding one or more metals to nickel-based catalysts, in methane steam reforming reaction, is provided.

Morales-Cano et al. studied the role of Rh, Ir, and Ru as promoters in $Ni/\alpha\text{-}Al_2O_3$ catalysts in the methane steam reforming reaction [88]. The sintering of the metal nanoparticles and the alloying between nickel and the metal promoters was realized by ageing at 800 °C and a PH_2O = 22 bar. The characterization results revealed that the degree of alloying and sintering is strongly affected from the promoter. Rhodium and iridium have shown an increase of the alloying degree with nickel during the ageing process, due to the high mobility of the nickel species and diffusion into the structure of the promoters; moreover, the sintering of the nickel particle was mitigated. Ruthenium have shown a low propensity to alloy with nickel and, therefore, a lower sintering resistance was obtained. The density functional theory calculations have shown that the diffusion of nickel atoms in ruthenium lattice structure is not energetically favourable; on the contrary, nickel atoms are equally stable in the first and second surface layers of iridium and rhodium. The catalytic activity tests have shown considerably higher activity for all of the bimetallic catalysts, Ni–Rh/Al_2O_3 Ni–Ir/Al_2O_3 and Ni–Ru/Al_2O_3, than Ni/Al_2O_3 in methane steam reforming reaction; moreover, the Ni–Rh/Al_2O_3 and Ni–Ir/Al_2O_3 have shown higher activity than Ni–Rh/Al_2O_3 and Ni–Ir/Al_2O_3, respectively; on the contrary, Ni–Ru/Al_2O_3 have shown lower activity than the monometallic Ru/Al_2O_3.

Lertwittayanon et al. studied the effect of $CaZrO_3$ as promoter for Ni/α-Al_2O_3 catalysts in methane steam reforming [89]. The promoted catalysts were prepared by the impregnation of α-Al_2O_3 with the mixed solution of calcium and zirconium nitrate; the resulting oxide was impregnated with the nickel nitrate solution. Each catalyst contained 10 wt % of nickel and 5, 10, or 15 wt % of $CaZrO_3$. The activity tests highlighted the best performance of catalyst that was promoted with 15wt % of $CaZrO_3$, in terms of CH_4 conversion and hydrogen yield. Three different S/C ratios were investigated (from 1/3 to 3); contrary to what was expected the S/C ratio 3 resulted in an excessive steam adsorption at the oxygen vacancies of the promoter; consequently, the competitive adsorption between methane and steam caused a decreasing of methane dissociation.

Jaiswar et al. studied the effect of the addition of platinum to Ni/$MgAl_2O_4$ catalyst, in the MSR reaction [90]. The bimetallic catalysts were obtained by the dry impregnation of Ni/$MgAl_2O_4$ with H_2PtCl_6*$6H_2O$; a series of catalysts were prepared with a platinum percentage in the range 0–1 wt %. The results have shown that the addition of platinum increased the activity of the catalyst, and the highest effect was obtained by loading 0.1wt % of platinum, an increasing of the loading resulted in a decreasing of the activity. These results were related to metal dispersion, the highest dispersion was, in fact, obtained with 0.1 wt % loading of platinum. Azancot et al. studied the effect of the preparation method of Ni-Mg-Al based catalysts on the activity in methane steam reforming [91]. The catalysts were prepared by means of three techniques, for the impregnation of γ-alumina with magnesium nitrate and nickel nitrate, for the coprecipitation-impregnation method, in which the magnesium and aluminium nitrates were coprecipitated and, subsequently, impregnated with nickel nitrate, finally for coprecipitation of the three metal nitrates. The activity of the catalysts was related to the degree of Ni-Mg- Al interaction; according to the reducibility, the Ni/$MgAl_2O_4$ catalyst have shown the optimal metal-support interaction and the highest catalytic activity and hydrogen production. Boudjeloud et al. studied the La-doped nickel catalysts that were supported on α-Al_2O_3, at different Ni/La ratio (7/3, 8/2, 9/1) in methane steam reforming [92]. The results have shown that the addition of lanthanum might cause strong change at the surface of NiO sites, obtaining smaller and better dispersed NiO particles with a strong interaction with the support, and increasing the spacing between the active nickel particles, thus preventing their agglomeration and sintering. The small Ni particles, which were highly dispersed, enhanced the dissociative adsorption of CHx species, while the highest hydrogen yield was obtained with the 7Ni-3La/α-Al_2O_3 catalyst. Nazari and Alavi studied the effect of adding copper and zinc to Ni/Al_2O_3 catalysts for methane steam reforming reaction [93]. The results have shown that zinc could enhance the activity, stability, and hydrogen selectivity of the Ni/Al_2O_3 catalysts; copper led to a significant enhancement in the stabilization of the catalyst toward the coke formation. Based on the Taguchi design results, the optimum catalyst, in terms of hydrogen yield and lower selectivity to CO, was 15Ni-1Cu-5Zn/γ-Al_2O_3.

In **Table** *2* the summary of preparation procedures and operating conditions used in polymetallic catalysts and related publications is reported.

Table 2: *summary of preparation procedures and operative conditions used in polymetallic catalysts and related publications.*

Catalyst (Particle size)	**Preparation procedure**	**Operating conditions**	**Selected catalyst CH_4 conv./ CH_4 conv. rate temperature/pressure (Time on stream, deactivation)**	**Ref**
Ni-X/α-Al_2O_3 X=Ru, Rh, Ir (7-30 nm)	α-Al_2O_3, $Ni(NO_3)_2*6H_2O$, H_2O, $Rh(NO_3)_2*xH_2O$ or $IrCl_3*6H_2O$ or $Ru(NO_3)_3(NO)$. $T_{calcination}$=450°C.	GHSV=11,195 h^{-1}; $CH_4/H_2O/H2$=2/8/0.8; T=500°C; P=30 barg	Ni-Ir/α-Al_2O_3 CH_4 conv. rate≈0.17 mol/g_{cat}*h Ni-Ru/α-Al_2O_3 CH_4 conv. rate ≈0.22 mol/g_{cat}*h Ni-Rh/α-Al_2O_3 CH_4 conv. rate ≈0.22 mol/g_{cat}*h	[88]
Ni/$CaZrO_3$/α-Al_2O_3 x=5,10,15 wt%	α-Al_2O_3, H_2O, $Ca(NO_3)_2*4H_2O$, $ZrO(NO_3)_2*H_2O$. $T_{calcination}$=800°C. $Ni(NO_3)_2*6H_2O$, H_2O. $T_{calcination}$=700°	WHSV= 60,000 ml/h g; $H_2O/CH_4/Ar$ =1/1/3, 1/3/6 and 3/1/6.	15Ni/15$CaZrO_3$/α-Al_2O_3 XCH_4≈67%, T=700°C S/C=1 (10h, ≈0%)	[89]

	C.			
xPt/15wt%Ni/MgAl$_2$O$_4$ x=0-1 wt% (7.6-14.9 nm)	15wt%Ni/MgAl$_2$O$_4$, H_2PtCl_6*6H_2O, H_2O. $T_{calcination}$=600°C.	WHSV= 0.34 g_{cat}*h/mol; $CH_4/H_2O/N_2$=1/5/1 T=600°C; P=1-10 bar	T=600°C, P=1 atm x=0.00Wt% X_{CH4}≈48% (8h, ≈1%) x=0.01Wt% X_{CH4}≈50% (8h, ≈2%) x=0.05Wt% X_{CH4}≈59% (8h, ≈1%) x=0.1Wt% X_{CH4}≈62% (8h, ≈1%) x=0.3Wt% X_{CH4}≈63% (8h, ≈3%) x=1.0Wt% X_{CH4}≈19% (8h, ≈2%)	[90]
Ni/Mg/γ-Al_2O_3 (21.9 nm)	1.$Mg(NO_3)_2$*6H_2O, γ-Al_2O_3 H_2O. 2.$Ni(NO_3)_2$*6H_2O., Mg/ γ-Al_2O_3 H_2O. $T_{calcination}$=550°C.	GHSV=60 L/gh, H_2O/CH_4=1.24, T=750-850°C.	X_{CH4}≈60%, T=850°C	[91]
Ni/$MgAl_2O_4$ (14.9 nm)	1.$Mg(NO_3)_2$*6H_2O, $Al(NO_3)_3$*9H_2O, NaOH, Na_2CO_3, H_2O. 2.$Ni(NO_3)_2$*6H_2O, $MgAl_2O_4$, H_2O. $T_{calcination}$=900°C.	GHSV=60 L/gh, H_2O/CH_4=1.24, T=750-850°C.	X_{CH4}≈74%, T=850°C	[91]
$NiMgAlO_X$ (42.1 nm)	$Mg(NO_3)_2$*6H_2O,	GHSV=60 L/gh,	X_{CH4}≈35%, T=850°C	[91]

	$Al(NO_3)_3$*9H_2O, $Ni(NO_3)_2$*6H_2O, NaOH, Na_2CO_3, H_2O. $T_{calcination}$=550°C.	H_2O/CH_4=1.24, T=750-850°C.		
xNi-yLa/α-Al_2O_3 (x/y=7/3, 8/2, 9/1)	α-Al_2O_3, $Ni(NO_3)_2$*6H_2O, $La(NO_3)_3$*6H_2O, H_2O. $T_{calcination}$=700°C.	GHSV=32x10^3 ml/g_{cat}h, CH_4/H_2O=1/3, 10%CH_4/Ar, T=500-800°C.	7Ni-3La/α-Al_2O_3 X_{CH4}≈87%, T=600°C (12h, ≈0%)	[92]
xNi-yCu-tZn/γ-Al_2O_3 (x=5,10,15; y=1,3,5; t=1,3,5)	γ-Al_2O_3, $Ni(NO_3)_2$*6H_2O, Zn (NO_3)*6H_2O, Cu (NO_3)*6H_2O, H_2O. $T_{calcination}$=900°C.	Methane molar rate (mol/min)=0.0002719 H_2O/CH_4 ratio=4, T=700°C.	15Ni-1Cu-5Zn/γ-Al_2O_3 X_{CH4}≈95%, T=700°C (10 h, ≈3%)	[93]

3.1.3. Deactivation studies

Catalysts life is intimately dependent on the process conditions and the composition of the feed stream; a reliable prediction of the catalyst's life cycle is extremely difficult [94]. Deactivation, which can take place by sintering, thermal degradation, coking, and poisoning, is one of the major issues related to the use of nickel-based catalysts in reforming processes. Sintering is an agglomeration phenomenon, for which the crystallite growth of the catalytic phases or the loss of the surface area of the support occur. The thermal degradation is a chemical transformation of the catalytic phase to non-catalytic phases [95]. Coking is a phenomenon for which coke covers the catalytic surface as the result of side reactions, such as the Boudouard reaction or cracking. Poisoning is due to the strong chemisorption of species on catalytic sites that block the catalytic activity. Catalysts regeneration is intimately related to the type of deactivation, which is the most used way to regenerate the reforming catalysts involves oxidative environments at high temperatures to burn off the coke [96]. Nickel-based catalysts that are deactivated by particle sintering can be successful regenerated by treatment with oxidative CO_2 atmosphere, as well as catalysts, deactivated by sulphur poisoning can be regenerated by steam/hydrogen stream treatment [97]. In this section, a selection of the latest article in deactivation studies in methane steam reforming process is provided.

Jablonski et al. presented a comparative study on the deactivation by H_2S, SO_2, and COS of Ni/YSZ and Ni/K_2O-$CaAl_2O_4$ commercial catalysts, in methane steam and dry reforming [98]. The composition of the feed stream was: 14.3 vol % He, 8.6 vol % H_2, 34.3 vol % N_2, 14.3 vol % CH_4, and 28.5 vol % H_2O or CO_2. The experiments were carried out, as follows: 30 min. of reforming followed by 90 min. of reforming in presence of sulphur species (H_2S, SO_2, and COS at concentrations of 1, 3, and 5 ppm). The results have shown that the Ni/YSZ catalyst was less active that the Ni/K_2O-$CaAl_2O_4$ commercial catalyst and it was also more sensitive to sulphur poisoning. The deactivation rates trend for the sulphur species on both catalysts was COS > $SO_2 \geq H_2S$. Yang studied the deactivation behaviour of a nickel-based catalyst by cofeeding H_2S in the methane steam reforming reaction [99]. The catalyst was prepared by wet impregnation of cement-modified α-Al_2O_3, with the salt precursors of cerium and nickel. The steam reforming reaction was carried out at a steam to methane ratios of 3.0 with a CH_4 flow of 40 ml/min, and at the reaction temperature of 700 °C, 800 °C, and 900 °C. After reaching a reaction steady state, H_2S was introduced into the reactor and the activity was evaluated every 30 min. The results have shown that the sulphur is more strongly adsorbed at lower temperatures, while a faster deactivation, at constant temperature, occurs at a higher concentration of hydrogen sulphide. At 900 °C, the sulphur poisoned catalyst keeps a residual reforming activity, while at 700 °C the activity of the catalyst rapidly decreases even at very low hydrogen sulphide concentration. Three regenerating techniques were also studied, by treatment with steam, with air and steam, or with hydrogen and steam. Treating the catalysts with steam for three hours followed by treating with hydrogen for three hours can be utilized to achieve the regeneration; however, the extent of the regeneration was related to temperature and increased with the increase of the temperature.

Laprune et al. studied the effect of exposure to naphthalene of Ni and Rh-based catalysts for MSR [100]. The preparation of the catalysts firstly provided the synthesis of the support; silicalite-1 was prepared by means of sol-gel method, while the Ni@silicalite-1 catalysts were prepared by means of an encapsulation method [101]. The reforming reactions were carried out at 700–900 °C at a space velocity GHSV of 750,000 h^{-1}, by feeding a reformate stream gas. The results have shown a strong decrease of the CH_4 conversion in the presence of 1400 ppm of naphthalene; however, the effect was partially reversible. The encapsulation did not prevent the poisoning of the catalysts, probably because naphthalene was able to hit the Nickel particles, despite the encapsulation. A similar deactivation was obtained with pyrene, which is bulkier, but crack to naphthalene; on the contrary, the effect of toluene was negligible. Haynes et al. studied the effect of calcination temperature on Ni-based lanthanum zirconate pyrochlore catalysts for methane steam reforming [102]. The results have shown that the catalysts that were calcined below 700 °C gave rise to the highest activity and selectivity, due to the smaller and well-dispersed nickel particles, and to less lanthanum enrichment on the surface of the support. The catalysts that were calcined at 700–900 °C have shown a reversible deactivation at both low and high reaction pressure (P = 1.8 MPa), which suggests a synergistic interaction between nickel and lanthanum. The exposure of fresh catalysts to high reaction pressures leads to the rapid and irreversible deactivation, due to the presence of LaOx species that cover the Ni particles. Hernandez et al. studied the effect of H_2S and thiophene on the methane and benzene steam reforming and water gas shift, for Ni/Al_2O_3, Ni/mayenite and Rh/Al_2O_3 catalysts [103]. The experiments were carried out by feeding a simulated coke oven gas stream, and the temperature range studied was 675–900 °C. The results have shown that the temperature plays a crucial role in determining the poisoning of the catalysts, in particular decreasing the temperature leads to the poisoning effect increasing, due to the exothermicity of the sulphur chemisorption equilibrium. The thermal conversion of thiophene reached the 42% at 800 °C, and the main products were H_2S and COS. In the presence of thiophene, Ni/Al_2O_3 and Ni/mayenite have shown similar benzene steam reforming activity, while Rh/Al_2O_3 outperformed both the nickel catalysts, especially at temperatures that were above 775 °C. The regeneration of the catalyst activity was possible only at 900 °C.

3.2. Ni-based structured catalysts

The aim of a distributed hydrogen production, for example, through an on-site type of hydrogen station, is only reachable if a novel reforming system is developed, with some unique properties that are not present in the large-scale reforming system. These properties include, among the others, (i) daily start-up and shutdown (DSS) operation ability, (ii) rapid response to load fluctuation, (iii) compactness of device, and (iv) excellent thermal exchange. In this sense, the catalyst has an important role. The fixed-bed reaction system that is adopted in the large-scale hydrogen manufacturing process cannot satisfy such properties, even if, in the last years, several studies were performed to optimize the catalyst shape, so minimizing the pressure drop and increasing methane conversion. In literature, different papers in which researchers performed experimental and simulation investigations on the role and effect of the Ni-based catalyst shape in packed bed reactors for MSR are present. In the paper of Buwa et al. [104] the authors analysed, through particle resolved CFD simulations of multi-layered packed beds, the effect of different boundary conditions and particle modelling approaches. In particular, the simulations had the aim of understanding the effect of particle shape on pressure drop (ΔP), dispersion, methane conversion, and effectiveness factors for methane steam reforming reactions. With this aim, 30 $Ni\text{-}\alpha Al_2O_3$ particles with different shapes (trilobe, daisy, hollow cylinder, cylcut, and seven-hole cylinder), as shown in Figure 11, with a tube to particle diameter ratio of 5, were considered. The authors developed a modified correlation that was able to predict ΔP for the particles with different shapes, since the empirical correlations usually used (Ergun and Zhavoronkov et al.) over-predicted the ΔP. The results have shown that the catalyst shape has an important effect: lower ΔP and higher dispersion can be obtained while using the externally shaped particles (trilobe and daisy), since they are characterized by a lower surface area and higher back flow regions, while higher CH_4 conversion and effectiveness factors can be obtained while using the internally shaped particles (cylcut, hollow, and seven-hole cylinder), since they assure the better access for the reactants. Among all, the cylcut-shape allowed for obtaining the best compromise between CH_4 conversion and ΔP.

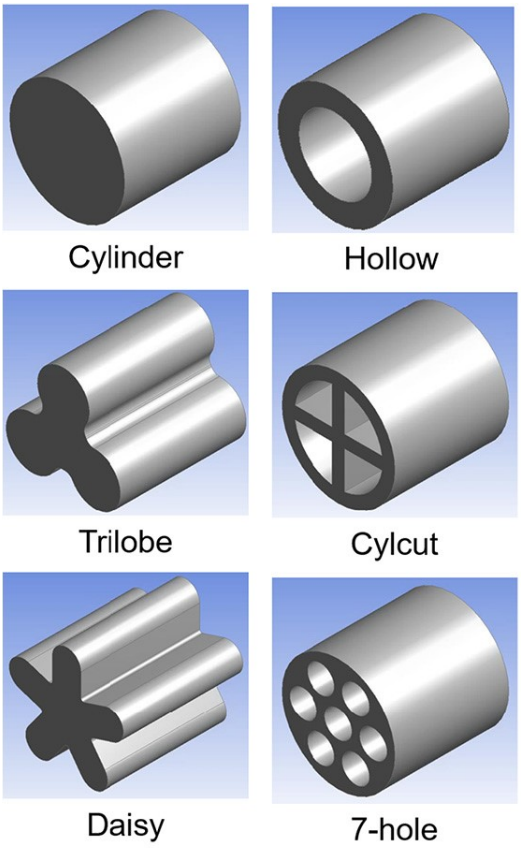

Figure 11: *Packing shapes considered in the work of Buwa et al. [63].*

Pashchenko investigated the effect of the Ni-αAl_2O_3 catalyst shape on the methane conversion and pressure loss in a packed bed reactor for MSR in a recent paper [105]. The author performed different experimental tests at a constant packed bed length (600 mm), in particular by varying the shape (a simple cylinder, a Raschig ring, a seven-holes cylinder, and a seven-holes sphere), and, in the case of the simple cylinders and the Raschig rings, also the end-to end dimensions (5 mm, 10 mm, 15 mm, 20 mm, and 25 mm) were varied. The results have shown that, as expected, the catalysts shape is important for determining the methane conversion and pressure drop. In particular, the seven-holes spheres allowed obtaining the maximum methane conversion and the minimum pressure drop, due to their higher surface area. Furthermore, it is reasonable thinking that the improvement of the performance of the steam methane reforming reactor can be obtained by increasing the geometric surface of the packed bed since the catalytic activity of the surface unit of all investigated catalysts was not dependent from their shape. Also, the reduction of the size of the catalyst particles allowed for increasing the methane conversion at a constant weight residence time [105].

Park et al. also faced the problem of the intensification of MSR fixed bed reactors [106], with the aim to identify and solve the typical problems occurring in the scale up of the process. So, the authors performed several experimental tests by using lab- and bench-scale reactors, investigating the effects of different reaction parameters, such as temperature, pressure, steam/methane ratio, and space velocity, on hydrogen production. The lab-scale tests allowed for the design of the bench-scale reactor, which is characterized by three consecutive heaters, and in which the thermodynamic and kinetic data that were obtained using the lab-scale reactor were used for choosing the operating conditions. The results have shown that a methane conversion higher than 90% and a hydrogen production higher than 10 L/min. was obtained in the bench-scale reactor only if all three consecutive heaters were able to heat the system up to 800 °C, at the gas-hourly space velocity of 2.0 L $CH_4/(h \cdot g_{cat})$. Furthermore, the author proposed an effective shutdown and start-up procedure, which was able to prevent catalyst deactivation during the shutdown, as well as allowed for decreasing the time and costs that are involved in the start-up.

Ko et al. [107] investigated the performance in MSR reaction of two Nickel-based catalysts, which were prepared using cylinder-shaped alumina pellets as supports: (i) egg-shell-type catalysts, in which nickel was selectively located in the outer region of the alumina pellets, by means of ethylene glycol or 1-octanol as hydrophobic solvents (in order to avoid or retard the internal penetration of the alumina pellets by the nickel nitrate solution), and (ii) 'homo-type' catalyst, with even nickel distribution inside the alumina pellets. The results highlighted that, in the case of the homo-type catalyst, the Ni loading has a fundamental role, since a loading of 3.5 wt %

did not allow for obtaining high methane conversion, while a loading of 10 wt % assured the same methane conversion of a commercial catalyst used as reference. On the other hand, egg-shell-type catalyst with a nickel loading of 3.5wt % have shown almost the same methane conversion as those of 10wt % 'homo-type' catalyst and the reference catalyst, so indicating that egg-shell-type catalysts were potentially feasible for use as MSR catalysts.

Apart from the intensification of MSR fixed bed reactor, in the way of an innovative distributed hydrogen production, the adoption of a different concept from the fixed-bed reaction system is necessary for the development of a novel reforming system. This concept includes the use of micro structured catalytic reactors or the use of structured catalytic reactors. In particular, the latter are very promising, since it is possible the integration and the optimization of the chemical (catalytic activity and selectivity) and the physical (enhancement of heat-transfer, rectifying property of flow, and lower pressure drop) properties by depositing a catalytic component onto a metallic or ceramic substrate with high thermal conductivity, thus resulting in an effective process intensification [108].

3.2.1 Micro-structured Catalytic Reactors

Some advantages that are characteristic of microreactors, such as (i) the reduced dimensions, included the weight, and compact design, (ii) the improved heat- and mass-transfer efficiencies, (iii) enhanced lifetime of catalyst, and (iv) higher conversion, yield, and the selectivity that they allow obtaining, made these reactors increasing the attention of the scientific community. The typical microreactor is designed to provide inside it mostly a laminar ($1< Re < 1000$), directed, and highly symmetric hydrodynamic flow and decreased interparticle mass-transfer resistance. In this way, a better and faster contact between reactants and catalyst, as well as more uniform temperature and concentration profiles, are assured due to the high surface to volume ratio. In addition, the possibility to realize in the microreactors the precise control of the main features, temperature, pressure, residence time, and flow rate, allowed for performing explosive and highly exothermic reactions with less risks than conventional processes [109]. All these positive features make possible an effective increase of the MSR process efficiency by using the micro-channel reactors, so favouring the increase of space time yields to approach the industrial requirement. Various micro-reactor types, such as coated wall micro-reactors, packed-bed micro-reactors, structured catalyst micro-reactors, and membrane micro-reactors, have been tested and used for hydrogen production [110].

Regarding the hydrogen production by means of MSR in microreactors, Chadwick et al. [109], developed a micro-structured catalytic hollow fibre with low mass- and heat-transfer resistance, by incorporating Ni/SBA-15 catalyst into alumina hollow fibres. The 5−25 μm widely opened radial microchannels that were present on the inner surface of the hollow fibres were responsible of the good catalyst incorporation and contributed to higher interaction between the reactants and catalyst, resulting in a higher catalytic performance. The authors compared the methane conversion that was achieved from both ceramic hollow fibre (CHF) reactor and the classical packed bed reactor, and the results have shown that, in both cases, a methane conversion close to thermodynamic equilibrium values (around 25% at 465 °C) was reached. However, in the case of the CHF configuration containing Ni/SBA−15 catalyst, a space velocity approximately 6.5 times higher was used. More important, the CHF configuration allowed for obtaining a higher CO_2 selectivity and an increased productivity rate, and this last result confirmed their potential for further reducing the required catalyst.

Cheng et al. [110] studied the effect of temperature, steam-to methane ratio, GHSV at high pressure varied from 0.5 MPa to 2.0 MPa on the catalytic performance of Ni catalyst plate for methane steam reforming reaction in micro-channel reactors. The results have shown that, at 240,000 h^{-1}, the methane conversion approached the thermodynamic equilibrium value at 900 °C and 2.0 MPa, hence indicating that micro-channel reactor with coated catalyst is feasible and highly efficient for MSR process. In these conditions, the authors reported a hydrogen productivity of about 0.1 m^3/h in a single channel at 2.0 MPa, which corresponded to 1.95×10^4 $m^3/(m^3\ h)$ space time productivity.

Kincal et al. [111] studied the possibility of performing the steam methane reforming reaction over Ni/mullite and Pd/CeO_2/mullite catalysts by using the solar energy as power source. In particular, a parabolic mirror with a 70 cm was used: so, delivering concentrated solar flux onto a focal area of about 3 cm in diameter. The authors compared the performance of powder and micro-structured reactors monolith (mullite) catalysts. The results evidenced a CH_4 conversion that was higher than 90% for both the samples, but a coke deposition was observed over the 15% Ni/Mullite monolith. These results, even if very interesting due to the renewable power source used, denoted the need for further improvements. In fact, the coke formation must be decreased, in order to increase the lifetime of the catalyst. For example, more consistent water vapor delivery can be performed, or the catalyst formulation can be optimized.

3.2.2 Structured Catalytic Reactors

In the perspective of process intensification, dedicated studies have demonstrated that the use of a carrier with a high thermal conductivity can allow for obtaining better catalytic performance. The main studied carriers can be divided in two groups: (i) metallic and (ii) ceramic.

3.2.2.1 Metallic carriers

The most investigated metallic carriers are the honeycomb fin (Figure 12), on which the active species are deposited by means of different techniques.

Fukuhara et al. studied the effect of the preparation procedure on the reforming performance of a nickel-based metal honeycomb-type catalyst in 2015 [108]. The authors prepared the catalyst while using the combined technique of the sol–gel method and the electroless plating on the stainless-steel substrate, by varying (i) the reducing agents in the plating bath (NaH_2PO_2, $NaBH_4$, or $(CH_3)_3NBH_3$), (ii) the plating time, and (iii) the nickel source ($NiCl_2$, $NiSO_4$, or $Ni(NO_3)_2$). The results have shown that the honeycomb catalyst that was prepared by using $NaBH_4$ with a plating time of 3 min. and chloride or sulphate as nickel source, demonstrated a higher methane steam reforming performance than the commercial catalyst. The authors also studied the effect of the addition of a promoter component to the aluminium sol solution, by adding Ce, Y, Mg, or Zr, and the reforming property of the catalyst that adds the Ce component was improved.

Figure 12: *Stainless honeycomb monolith [63].*

Xu et al. investigated the effect of the pre-treatment on the performance of catalytic Ni_3Al foils for steam reforming of methane [112]. The authors set up a pre-treatment procedure that consists of water vapor oxidation followed by H_2 reduction, and the results indicated that the catalytic activity and selectivity of the Ni_3Al foils towards MSR was enhanced when a water vapor treatment at 600–700 °C, followed by H_2 reduction at 600 °C, occurred. The authors highlighted the formation of a multi-layer surface structure on the foils after pre-treatment, consisting in fine Ni particles on the outermost layer, with subsurface layers consisting of $NiAl_2O_4$ and Al_2O_3, which, in their opinion, was responsible of the enhancement of catalytic properties.

Mundhwa et al. investigated the influence on MSR of different configurations of the coated combustion-catalyst (platinum-alumina) in a catalytic plate reactor (CPR), by means of simulation models. In one research, they compared a segmented configuration (SLCC-model) with a continuous configuration (CLCC-model) [113]. In a following research, they extended their studies, by simulating four different computational models with four different combinations of segmented and continuous configurations, (i) Continuous Combustion-catalyst and Continuous Reforming catalyst (CCCR), (ii) Continuous Combustion-catalyst and Segmented Reforming catalyst (CCSR), (iii) segmented combustion-catalyst and continuous Reforming catalyst (SCCR), and (iv) segmented combustion-catalyst and segmented reforming catalyst (SCSR), between the combustion-catalyst and reforming-catalyst [114]. In both research, the authors investigated the influence of flow direction, gas hourly space velocity (GHSV), and reforming-catalyst thickness on the performance of CPR. The results have shown that the best performance in terms of methane conversion and hydrogen production, as well as in terms of minimizing the maximum reactor plate temperature, axial thermal-gradients, and thermal hot-spots, were obtained by using the segmented combustion-catalyst in co-flow mode. In fact, this configuration assures a continuous supply of heat to the reforming-side from the combustion-side through the interspacing among active combustion-catalyst segments. In this way, the formation of cold and hot zones is avoided and a balanced thermal distribution at the reactor downstream is obtained. In addition, the authors have shown that the CPR that was designed with SLCC configuration required both less combustion feed flow (about 7 to 8%) and combustion-catalyst (about 70% less) to produce the required hydrogen flow (29.80 mol/h) to feed a 1 kW fuel cell as compared to the CPR designed with CLCC. Moreover, a significant reduction and the complete disappearance of the thermal hot spots at the initial length of the catalysts are observed with the SCSR and SCCR configurations, respectively, when compared to the conventional CCCR design. In addition, the authors reported that both reforming-side and combustion-side effective thermal conductivities were noticeably improved for the first 44% and 36% of the catalyst length in a CPR that was designed with the SCSR and SCCR configurations, respectively, when compared to the CCCR configuration.

Tightly rolled Ni coil catalysts were extensively studied by the research group of Hirano, Xu et al. The authors assembled and tested in MSR a tightly rolled Ni coil catalyst using only 30 mm-thick pure Ni foils, in a wide range of space velocities (455–2800h^{-1}) and S/C (0.62–2.48) ratios [115]. The results have shown that the high geometric surface area per catalyst volume (88.1 cm^2/cm^3) that was achieved for the Ni coil catalyst allowed for obtaining a high H_2 production rate per unit catalyst volume and a high CH_4 conversion, so demonstrating the high potential of this kind of catalyst for small-scale hydrogen production systems. The authors continued their research by assembling and testing, in MSR, a tightly rolled Ni coil catalyst, always using only 30 mm-thick pure Ni foils, with a higher cpsi (about 2300) if compared to the previous one (about 700) [116]. The results have shown that the honeycomb catalyst with higher cpsi have shown higher catalytic activity for methane steam reforming at low S/C (1.36) and high GHSV (6400 h^{-1}) than the one with lower cpsi. The authors also performed isothermal tests at 800 °C, and the results have shown a decrease in the catalytic activity of the honeycomb catalyst in first hours, up to reaching the stable value of about 40%. In-situ XAFS measurements revealed that the decrease in activity at temperatures lower than 750 °C was due to the oxidation of surface Ni atoms during the catalytic reaction. Subsequently, the authors investigated the influence of steam treatment and hydrogen reduction on the catalytic activity of the pure Ni honeycomb catalyst with the higher cpsi [117]. The results have shown that a steam treatment and subsequent hydrogen reduction at a temperature higher than 800 °C enhanced the catalytic activity of the Ni honeycomb catalyst. The authors attributed this enhancement to the combined effect of the two treatments: in fact, the steam treatment is responsible for the formation of fine Ni oxide particles, which are reduced to metallic Ni on the surface during the hydrogen reduction, hence suggesting a structure sensitivity of the MSR.

Settar et al. compared four different Wall-Coated Steam Methane Reformer (WC-SMR) with a catalytic surface [118]. In particular, the authors compared a classical WCSMR, with three modified configurations, in which three different inert Metal Foam (MF) matrices were inserted in the catalytic region: Ni-Foam, Ni-Cr-Foam, and Ni-Fe-Cr-Foam, identified as MF (A), MF (B) and MF(C), respectively.

The results have shown that the use of MF in such configurations increased the CH_4 conversion, since they allowed for a good heat distribution inside the system and better contact among the gas mixture and the catalyst particles, as well, as they were able to reduce the gas mixture velocity. In particular, the inert Ni-Fe-Cr-Foam, MF (C) resulted in the most significant improvement of the conversion rate, 18.64%, and of H_2 production, 16.91%, when comparing to the clear WC-SMR. These results confirmed the possibility to enhance the MSR by adding inert metallic foam in the catalytic region of a WC-SMR; one possible optimization of this system could be the use of catalysed metallic foams.

Ashraf et al. investigated the preparation, characterization, and testing in MSR of Fecralloy® monoliths with different cell density (461–1367 cpsi), catalysed with different loadings of Ru/La-Al_2O_3 (100–200 mg) [119]. The results have shown that the methane conversion increased with increasing temperature, catalyst loading, and cell density. In particular, in correspondence of the same washcoat thickness (about 20.6 μm), the higher cell density monolith has shown 13.6% higher methane conversion at 600

°C, weight hourly space velocity (WHSV) = 55 NL h^{-1} g_{cat}^{-1}, and ratio S/C = 3.0, as compared to the lower cell density one.

Shigarov et al. investigated the performance of a compact (800 cm^3) membrane reformer module to produce 0.25–0.30 Nm^3/h of hydrogen by MSR by means of experimental tests and modelling [120]. The module consists of a two-sided composite membrane disc with a 50 mm Pd-Ag layer and two adjacent 4 mm thick Ni foam discs (60 ppi). A nickel catalyst and porous support were deposited on the foam discs to give the final composition of 10%Ni/10%MgO/Ni-foam. The modules were tested at an 8–13-bar pressure of the mixture in the reforming zone and at 1-bar of pure hydrogen under the membrane, $H_2O/C = 2.5–3$, and a module temperature of 550–680 °C (with and without hydrogen removal). Calculations were made for revealing the effect of thickness of the Pd-Ag membrane layer (5–50 μm), thickness of the Ni foam discs (0.5–8 mm), and temperature (600–700 °C) on the hydrogen output of the module in order to optimize construction of the module. The results evidenced a production of hydrogen higher than 0.7 $kg(H_2)/h/m^2$ and an energy production higher than 1 MW/m^3.

Payak et al. proposed an innovative Methane Steam reforming reactor, whose novelty consisted in dividing it into segments of various lengths and reactivity. In particular, the catalyst (nickel and yttria-stabilized zirconia) was split, and the created empty volume was filled with porous, nonreactive, thermal conducting metallic foam [121]. This approach allows for moderating a sharp temperature drop at the inlet of the reactor typical for the endothermic methane/steam reforming process. The authors developed and implemented an in-house solver for the mathematical and numerical models of transport phenomena and the reaction kinetics (taken from the literature). The results of the model were compared with the experimental tests, which were performed by varying the number and lengths of catalytic and non-catalytic segments, and good agreement was found. The results indicated that a reduction of the difference between the maximum and minimum values of the temperature inside the reactor occurred, and the conversion rate decreased 15% in correspondence of a reduction of catalyst of a half, so evidencing that it is possible to realize a reactor for steam reforming, with less catalyst used and obtaining the same methane conversion rate as the reference case with relatively small elongation of reforming unit.

Deo et al. investigated the effect of adding Rh to 15 wt % $Ni/MgAl_2O_4$ catalyst for the MSR [122]. In particular, the authors washcoated FeCralloy metal monoliths with a 0.5wt %Rh-15wt %$Ni/MgAl_2O_4$ catalyst and compared its performance with a packed bed and a 15%wt$Ni/MgAl_2O_4$ washcoated metal monolith. The results evidenced that, in the operating conditions of Twall = 600 °C, P = 1-bar, ratio S/C = 5, GHSV = 6000 h^{-1}, and W/F_{ao} = 0.34 g_{cat}-h/gmol, the Rh-$Ni/MgAl_2O_4$ washcoated metal monolith have shown the best performance in terms of methane conversion (about 50%) if compared to $NiMgAl_2O_4$ washcoated metal monolith and packed bed reactor (about 40% and 25%, respectively).

Recently, Tronconi et al. proposed and tested in MSR an innovative fixed bed reactor configuration, consisting in small catalytic pellets filling the voids of highly conductive metallic open-cell foams [123]. The aim was to enhance the radial heat transfer of the tubular reactor by using a high thermal conductivity solid. In particular, alumina egg-shell particles with diameter of 600 μm, catalysed with Rh/Al_2O_3, were used to fill the voids of FeCrAlY open cell foams of 12 ppi and copper open cell foams of 10 and 40 ppi. The results of the tests, which were performed at GHSV of 5000 and 10000 h^{-1} in the temperature range 600 – 800 °C, highlighted the benefits in terms of thermal management of the reactor and an increase of productivity at the same furnace temperature in kinetically-limited conditions. The authors, based on the electric equivalent circuit approach, also developed a heat transfer model of the packed foams, incorporating independently estimated lumped or effective parameters, thus providing an engineering rationale of the observed reduction of temperature gradients across the catalytic bed.

Table *3* summarizes the main performances of the packed bed reactors and of the catalysts supported on metallic carriers.

Table 3: *main performances of the packed bed reactors and of the catalysts supported on metallic carriers.*

Structured carrier shape	**Catalyst**	**Op. conditions**	**Main characteristics**	**Main performance**						**Ref.**
Ceramic Packed bed	$Ni/\alpha Al_2O_3$	Initial mass fractions CH_4 = 0.1966 H_2 = 0.0005 CO = 0.0007 CO_2 = 0.1753 H_2O = 0.6269 Re_t = 50000	Surface area, mm^2	DP, Pa	T_s, °C*	Q_{sink}, W*	X_{CH4}, %*	η_1*	η_3*	
Cylinder			1885	1109	723.87	1159	1.984	0.269	0.452	[104]
Trilobe			1637	165	727.96	787	1.373	0.393	0.595	
Daisy			1955	164	732.33	868	1.475	0.438	0.639	
Hollow			2428	197	742.47	1062	1.831	0.551	0.766	
Cylcut			3484	208	750.66	1243	2.136	0.689	0.857	
7-hole			3737	218	752.06	1283	2.187	0.690	0.865	
Ceramic packed bed	NiO=14.5%;	T=500°C to 700°C	surface area =	@ S/C=1, flow rate = 15 g/s, p=3 bar, T = 700 °C						[105]

Cylinder	SiO_2=0.2 %; support CaO-MgO-La_2O_3-αAl_2O_3	P = 3 bar S/C = 1 to 4 Residence time = 1 to 8 $kg_{cat}\cdot s/mol$	4.5 m^2/g_{cat} bulk density = 680 kg/m^3 average porosity = 41%	X_{CH4} = 62%	
Raschig ring				X_{CH4} = 70%	
7-hole cylinder				X_{CH4} = 75%	
7-hole sphere				X_{CH4} = 80%	
1-hole cylinder	Ni = 20wt%, CaO-Al_2O_3= 80 wt%	T=500°C to 850°C P = 0.2 to 1 MPa S/C ratio = 2 to 3.3 GHSV = 2 to 40 l $CH_4/(h\cdot g_{cat})$	surface area = 21.26 m^2/g_{cat} density = 1.8 g/cm^3 pore size = 111 Å	Thermodynamic CH_4 conversion values reached @ GHSV = 2 l $CH_4/(h\cdot g_{cat})$, T > 800°C, P = 1 MPa, S/C = 3	[106]
cylinder-shaped alumina pellets	E-5Ni**	T = 700 °C to 800 °C S/C = 3 WHSV = 3000 $ml/(g_{cat}\ h)$	Ni = 5.6wt% Surface area = 204 m^2/g	X_{CH4} = 96% @ 700°C X_{CH4} = 99% @ 800°C	[107]
	E-3.5Ni**		Ni = 3.5 wt% Surface area = 167 m^2/g	X_{CH4} = 96% @ 700°C X_{CH4} = 97% @ 800°C	
	E-3.5Ni-5Mg**		Ni = 3.1 wt% Mg = 4.5 wt% Surface area = 120 m^2/g	X_{CH4} = 95% @ 700°C X_{CH4} = 98% @ 800°C	
Micro-channel reactor Metal-ceramic plate	Ni = 15.87wt%	T = 800 °C to 900 °C S/C = 3 to 5 P = 0.5 to 2 MPa GHSV = 40000 to 240000 h^{-1}	Surface area = 108.75 m^2/g Catalyst layer thickness = 70 mm	Thermodynamic CH_4 conversion value and H_2 productivity = 0.1 m^3/h @ T=900°C, GHSV = 240000 h^{-1}, P = 2 MPa, S/C = 3	[108]
honeycomb	Ni/Ce	T = 450 to 650°C S/C = 2 P = 1	Surface area = 152 m^2/g	X_{CH4} = 79.1% S_{CO} = 59.4% S_{CO2} = 40.6% @ 650°C	[108]

		atm			
Rolled foils	Ni_3Al	T = 600 to 800°C S/C = 1 GHSV = 0.091m^3/(hm^2)	total geometrical surface = 0.0066 m^2	X_{CH4} = 90% S_{CO} = 99% S_{CO2} = 2% @ 650°C	[112]
Rolled foils	Ni	GHSV = 455 to 2880 h^{-1} S/C=0.62 to 2.48 T= 700 to 800°C	Geometric surface area = 66.4 cm^2 Pore density = 700 cpsi specific surface area = 88.1 cm^2/cm^3	X_{CH4} = 94.0% S_{CO} = 91.1% S_{CO2} = 8.9% H_2 yield = 77.6% H_2 production rate = 8.7 ml/min H_2 production rate/Volume = 11.6 ml/min/cm^3 @ T= 800°C, GHSV = 535 h^{-1}, S/C = 1.24	[115]
Rolled foils	Ni	GHSV = 6400 h^{-1} S/C=1.362 T= 600 to 900°C	Geometric surface area = 43.72 cm^2 Pore density = 2300 cpsi specific surface area = 87.2 cm^2/cm^3	X_{CH4} = 55.7% @ T= 800°C	[116]
Rolled foils	Ni	GHSV = 6400 h^{-1} S/C=1.362 T= 600 to 900°C	Geometric surface area = 43.72 cm^2 Pore density = 2300 cpsi specific surface area = 87.2 cm^2/cm^3	X_{CH4} = 90% @ T= 900°C, Ni honeycomb catalysts steam treated at 900 °C for 1 h followed by H_2 reduction at 900 °C for 1 h	[117]
foam	Ni	w^0_{CH4} =	ppi = 10	X_{CH4} = 29.491 %	[118]

		21.28 w^0_{H2O} = 71.45 w^0_{H2}= 2.60 w^0_{CO} = 1.19 w^0_{N2} = 3.48 T_0= 550°C P =1 bar	K_P = 1.2 m^2*** C_f=0.097 *** ρ_s = 8900 Kg/m^3*** λ_s= 71 W/m K***	H_2 production rate = 47.645	
	Ni-Cr	w^0_{CH4} = 21.28 w^0_{H2O} = 71.45 w^0_{H2}= 2.60 w^0_{CO} = 1.19 w^0_{N2} = 3.48 T_0=550°C P =1 bar	ppi = 20 K_P = 1.185 m^2*** C_f=0.1*** ρ_s = 8420 Kg/m^3*** λ_s= 22.5 W/m K***	X_{CH4} = 22.534 % H_2 production rate = 41.015	
	Ni-Fe-Cr	w^0_{CH4} = 21.28 w^0_{H2O} = 71.45 w^0_{H2}= 2.60 w^0_{CO} = 1.19 w^0_{N2} = 3.48 T_0=550°C P =1 bar	ppi = 10 K_P = 1.49 m^2*** C_f=0.099 *** ρ_s = 6285 Kg/m^3*** λ_s= 134.87 W/m K***	X_{CH4} = 37.400 % H_2 production rate = 53.577	
Fecralloy® monoliths	1.5wt%Ru/3wt% La-Al_2O_3	T = 600 to 900°C WHSV = 55 Nl/(h g_{cat}) S/C = 3	cpsi = 461 catalysts loading = 109 mg	Thermodynamic CH_4 conversion values @ 800°C X_{CH4} = 52% @ 600°C	[119]
		T = 600 to 900°C WHSV = 55 Nl/(h g_{cat}) S/C = 3	cpsi = 461 catalyst loading = 171.8 mg	Thermodynamic CH_4 conversion values @ 800°C X_{CH4} = 61% @ 600°C	
		T = 600	cpsi =	Thermodynamic CH_4 conversion	

		to 900°C WHSV = 55 Nl/(h g_{cat}) S/C = 3	461 catalyst loading = 216.9 mg	values @ 800°C X_{CH4} = 62% @ 600°C	
Membrane reformer with Ni foam	10%Ni/10%MgO/Ni-foam	P = 1 bar T = 400 to 600°C S/C = 2	4 mm thick foam discs, 60 ppi	Thermodynamic CH_4 conversion values @ 600°C for the catalytic discs	[120]
FeCralloy monolith	0.5wt%Rh-15wt%Ni/$MgAl_2O_4$	T_{wall}= 600 °C, P= 1 bar, S/C=5, GHSV=6000 h^{-1} and W/F_{ao}= 0.34 g_{cat}-h/gmol		X_{CH4} = 50% H_2/CO = 37 H_2/CO_2 = 4.6 S_{CO} = 11.0x10^{-2}	[122]
Catalytic alumina egg-shell particles with diameter of 600 μm, filling the voids of FeCrAlY open cell foams of 12 PPI and copper open cell foams of 10 and 40 PPI	Rh/Al_2O_3	GHSV = 5000 and 10000 h^{-1} T= 600 to 800 °C S/C = 3.5	λ_s = 16 W/(m K) – FeCrAlY foam λ_s = 380 W/(m K) – Cu foam	Maximum radial temperature difference between wall thermocouple (WT) and central thermocouple (CT) = 40 for Cu foam – 50 for FeCrAlY foam X_{CH4} = 86.4% for Cu foam, 75% for FeCrAlY foam @ T_{oven} = 700°C	[123]

*Ts = volume averaged temperature; Qsink = normalized heat sink; X_{CH4} = normalized CH_4 conversion; ηi = effectiveness factors
** Egg-Shell type Ni Distribution

3.2.2.2 Ceramic carriers

The research group of the University of Salerno very deeply investigated the possibility to intensify the MSR by using Ni based catalysts supported on silicon carbide (SiC) and cordierite monoliths. The authors, by setting-up an advanced experimental reaction system, preliminarily studied the influence of the geometric configuration of the monoliths, as well as the Ni loading and the washcoat presence [124]. The experimental tests have shown that the monolith with "wall flow" (WF, the parallel channels are alternatively plugged at each end in order to force the reaction stream to flow through the inner porous walls) configuration had better performance in terms of hydrogen yields at the same temperature and GHSV with respect to the “flow through” (FT, the channels are open on both sides) configuration. In particular, the results highlighted that the preliminary deposition of a ceria-based washcoat on the support increases the specific surface area, thus allowing a better dispersion of the active species and consequently better catalytic activity, particularly at lower temperatures. These preliminary results demonstrated that the use of high thermal conductivity monolithic catalyst in wall flow configuration allowed to overcome the energy and mass limitations, which are the main bottlenecks of the commercial steam reforming catalysts. In addition, this research confirmed that the use of high thermal conductivity supports for Ni based structured catalysts may result in a feasible process intensification of the MSR, since the choice of these supports has the conjugated advantages of increasing the hydrogen yield and requires a lower temperature outside the reactor, allowing for an overall increase in the efficiency of the process. In this way, the optimization in catalytic volume management might lead to substantial performances increasing, which, in turn, assures a reduction in hydrogen production costs. The observed enhancements in thermal management inside the catalytic volume could result in practical application, not only in the steam reforming field: the minimization of heat transfer resistance could be achieved in all endothermic reactions, flattening the thermal profiles from the peripheral to the centre of the catalytic bed, hence resulting in an improving of reaction control. Moreover, the ability of SiC monolith to redistribute temperature in the catalytic volume might reduce the risks that are linked to hotspot phenomena for oxidative reactions, (such as partial oxidation of hydrocarbons): the optimal reaction control results in an enhanced safety of the process, as well as in an improved catalyst lifetime.

Moon et al. also investigated the SiC as support for Ni based structured catalysts for MSR [125]. The authors prepared and tested in MSR 10wt % Ni based catalysts, supported on calcium aluminate (CAx), which differ from each other by the carrier (with and without SiC). The results evidenced that the contemporary presence of CAx and SiC, as carrier, increased the thermal conductivity of the whole structured catalyst, thus allowing a higher catalytic activity in terms of methane conversion (>90%) and H_2 yield (>95%) as well as a higher coke resistance (coke formation <0,6%) at 750 °C, with respect to the other catalysts. These results confirmed that the Ni based catalysts supported on SiC could be promising candidates for producing hydrogen by the steam reforming of methane.

Other research groups also investigated the feasibility of ceramic supports different from SiC for the intensification of MSR. Ashraf et al. used ceramic monoliths (α-alumina) with square channels (100 cpsi) and hexagonal channels (170 cpsi), diameter 9 mm, and length 30 mm, loaded with

100/150/200/250 mg of catalyst (Ru(1,5wt %)/La(3wt %)-Al_2O_3) [126]. The results evidenced that the better performance in terms of methane conversion, in all of the tested conditions (temperature range 600–900 °C, WHSV = 27–368 NL h^{-1}gcat, molar steam to carbon ratio S/C = 3.0) was obtained with the catalyst loading of 100 mg (washcoat thickness of 58.5 μm) and 150 mg (washcoat thickness of 78.9 μm). These catalysts reached high methane conversion, approaching the thermodynamic equilibrium, at temperatures that were higher than 800 °C. The authors highlighted that the intensification of MSR could be obtained by using monoliths with high cell densities, since they can simultaneously increase the geometric surface area and the voidage, hence allowing a reduction of the thickness of the catalytic layer, in order to avoid internal mass transfer limitations.

Narataruksa et al. performed an interesting study to achieve optimal dimensions of a monolithic catalytic ceramic reactor for the highest rate of reaction in MSR [127]. The authors, by means of an analytical and CFD model, individuated the optimal length of a square channel monolithic reactor. The results of the analytical model have shown that the optimal length was of 41.6 mm with a reaction rate of 2.88×10^{-8} mol/s at the channel height of 1.5 mm, 600 °C, and 1 atm; the results of the CFD model and the experimental tests evidenced an optimal channel length of 80.0 mm and 90.0 mm, respectively, with respective reaction rates of 7.42×10^{-7} mol/s and $6.85 \text{ x } 10^{-7}$ mol/s. The CFD model was also used to investigate the effects of channel heights that ranged from 0.5 to 3.0mm, by the definition of methane conversion per unit channel perimeter: the highest value (50% mm^{-1}) is afforded at a channel height of 0.50 mm. The results of the CFD model can be summarized in the sense that a constant reaction rate was established at an L/H ratio of 53, while the experimental results that were performed with monoliths with different channels allowed for concluding that a constant reaction rate occurred at an L/H ratio of 60.

Nam et al. numerically investigated the effects of the washcoat properties, including the layer thickness (20–80 mm), the mean pore diameter (10–40 nm), and the volume-specific catalyst surface area ($1.1–3.3 \times 10^7$ m^2/m^3), in the Ni/$MgAl_2O_4$ washcoat catalyst layers that were used in MSR conditions relevant to small-scale hydrogen production systems (1–3-bar pressure, 600–800 °C temperature, and 2–4 steam-to-carbon ratio) [128]. The authors used the intrinsic reaction kinetics (Xu and Froment model) and multicomponent mass diffusion (Maxwell-Stefan equation) in their simulations, and proposed correlation equations for easy evaluation of the effectiveness factors (presented as a function of the methane conversion ratio and effective Thiele moduli) coming from the simulations. The authors demonstrated that the proposed correlation equations could adequately estimate the effectiveness factor data that were obtained by numerical calculation, hence providing useful data for designing small-scale MSR systems and performing numerical simulations.

Leonzio developed an ANOVA analysis, in which an integrated Pd-based membrane reactor is considered for the MSR. The catalyst is a Ni(10)/CeLaZr catalyst that is supported on SSiC ceramic foam, and the reactor was modelled in MATLAB software while using the Numaguchi kinetic [129]. The results have shown that only inlet temperature, methane flow rate, their interaction, and the thickness of membrane are significant in order to improve the performance of the reactor in terms of hydrogen yield, carbon dioxide conversion and methane conversion. In particular, methane conversion of 99%, carbon dioxide conversion of 40%, and hydrogen yield of 3.2 can be achieved with an inlet temperature equal to 823 °C, methane flow rate equal to 0.1 kmol/h, hydrogen permeability equal to 3600 $\text{m}^3\mu\text{mm}^{-2}\text{hbar}^{0.5}$, being chosen in order to have better performances of membrane, and a thickness equal to 0.003 m to reduce the costs.

Table *4* summarizes the main performances of the catalysts supported on ceramic carriers.

Table 4: *Summary of the main performance of the catalysts supported on ceramic carriers.*

Structured carrier shape	**Catalyst**	**Operating conditions**	**Main characteristics**	**Main performance**	**Ref.**
SiC monolith	30wt%Ni	GHSV = 5000 to 25000 h^{-1} T = 600 to 800°C P = 1 bar S/C = 3	Direct impregnation λ_s = 350 W/(m K) – SiC monolith Flow through configuration	Thermodynamic CH_4 conversion values for T > 800°C	[124]
	20wt%Ni/20wt%CeO_2	GHSV = 1250 to 5000 h^{-1} T = 550 to 800 °C P = 1 bar S/C = 3	Washcoating + Ni direct impregnation λ_s = 350 W/(m K) – SiC monolith Flow through and Wall Flow configuration	Thermodynamic CH_4 conversion values for T > 800°C - Flow Through Thermodynamic CH_4 conversion values for T > 750°C – wall Flow	
calcium aluminate modified SiC	10%Ni	GHSV = 30000 h^{-1} T = 650 to 850 °C P = 1 bar S/C = 1 to 3	1mm granules λ_s = 1.16 W/(m K)	X_{CH4} = 97.9% at T = 650°C and S/C = 3 X_{CH4} = 81.3% at T = 850°C and S/C = 1	[125]
αAlumina	1.5wt%Ru/ 3wt%La-Al_2O_3	T = 600 to	Catalyst	Thermodynamic	[126]

monolith		900°C S/C = 3 WHSV=27 to 368 Nl h^{-1} g_{cat}^{-1}	loading = 100 to 250 mg	CH_4 conversion values at T > 800 °C for 100 and 150 mg catalyst loadings	

3.3 MW-assisted reforming processes

Regarding the microwave-assisted reforming processes, the CO_2 reforming of methane was studied by some research groups [130]. Zhang et al. [131] studied the CO_2 reforming of methane with Pt catalysts both with microwave-assisted and conventional heating: they reported that H_2/CO ratio at low temperatures was lower than the equilibrium for conventional heating, while it was higher for the microwave-assisted one; at high temperatures, the H_2/CO ratio approached the thermodynamic equilibrium for both the heating systems. The MW effect was attributed to hot-spots formation, when microwave heating was employed, there are some zones in the catalytic bed where the reaction occurs at higher temperatures than those measured, giving a higher H_2/CO ratio. At high temperatures, this phenomenon is less evident, in fact the ratio approached the equilibrium value. Moreover, the Pt loading had a very little effect in conventional heating (CH), while in MW heating the effect was more evident, showing that Pt catalyses the reverse Water Gas Shift (WGS) reaction preferentially. Fidalgo et al. [132] investigated mixtures of carbon and Ni/Al_2O_3 for the CO_2 reforming of methane: Ni/Al_2O_3 is not heated by MW radiation, so it must be mixed with a MW receptor, such as carbonaceous material. They studied the effect of the addition of a commercial activated carbon, FY5, and a metallurgical coke. As the first has its own catalytic effect, the best performances were reached with FY5+ Ni/Al_2O_3. Ni/FY5 was also tested since in this way the support is a microwave receptor, but the authors found that its activity was lower than that reported for the solid mixture. Moreover, the work highlighted that the FY5+ Ni/Al_2O_3 mixture gave the same conversion of Ni/Al_2O_3 in a CH system, so the loss in catalyst amount due to the mixing with FY5 was offset by the enhancement in conversion due to MW heating. The same researchers reported in a subsequent study [133] that the estimated energy consumption in a pilot plant using MW heating is remarkably lower for the FY5+ Ni/Al_2O_3 mixture than Ni/FY5 (44.4 kW per m^3 of produced H_2 in the first case and 4.6 kW in the latter) because of the higher amount of produced H_2 per mass of C/MR (catalyst/microwave receptor) ratio. Moreover, FY5+ Ni/Al_2O_3 energy consumption is comparable with the conventional steam reforming stage of industrial H_2 production processes (1.2 kW per m^3 of produced H_2). The improvement of the catalytic properties in MW heating processes was confirmed by Domìnguez et al. with a rich potassium char as a catalyst [134]. They found that MW heating can enhance the conversion of both methane and carbon dioxide thanks to the hot spots generated by the interaction between the MW field and the catalyst. Moreover, the study of the exhausted catalyst have shown the formation of a significant amount of carbon nanofibers on the char surface, obtained only with MW heating; the nanofibers were more abundant in the dry reforming reaction rather than the single CH_4 decomposition, due to the higher amount of carbon in the system. Sharifvaghef et al. studied the microwave-assisted dry reforming of methane over Ni and Ni–MgO catalysts supported on activated carbon (AC) [135]. The authors studied the effect of operating parameters, including the type of catalysts' active metal and their concentration in the AC support, feed flow rate, and reaction temperature on the reaction conversion and H_2/CO selectivity. The results of the tests evidenced that the catalysts' activity was increased under microwave heating and as a result, the feed conversion and hydrogen selectivity were enhanced in comparison to the conventional heating method. Li et al. studied the syngas production through the dry reforming of methane with CO_2 using 2.45-GHz microwave plasma conditions [136]. The results of their tests evidenced that the presence of a Ni catalyst resulted in a lower ratio of syngas compared to the plasma reaction without a catalyst. The results of the tests highlighted how the MW heating had a positive effect by increasing the catalysts' activity, as well as the methane conversion and hydrogen selectivity. Recently, Gangurde et al. [137] synthesized a ruthenium doped $SrTiO_3$ perovskite catalyst and applied it in the DRM reaction. The synthesized Ru/$SrTiO_3$ have shown high microwave susceptibility and stable catalytic behaviour. As a continuation, the same group [138] studied a range of mechanical mixtures of Ru/$SrTiO_3$ and different commercial and relatively cheap nickel supported metal oxides, in order to improve the overall microwave heating properties. De Dios Garcia et al. studied microwave-assisted DRM on Pt/C and Ni/Al_2O_3 catalysts, and two silicon carbide-based mechanical mixtures, i.e., Ni/Al_2O_3-SiC and Ni/SiC [139]. The authors developed a custom-designed rectangular mono-mode microwave applicator, and the results evidenced the better performance of the mechanical mixture of Ni/Al_2O_3-SiC (conversions of CH_4 and CO_2 of 90% at 800 °C and WHSV of 11,000 mL/g/h) with respect to the conventional heated catalyst (79% conversion of both CH_4 and CO_2).

Regarding the methane steam reforming, there are relatively few studies present in literature regarding the microwave-assisted process. Wang et al., studied the methane steam reforming performed through MW plasma at atmospheric pressure conditions, by using Ni/Al_2O_3 catalysts loaded in the discharge zone [140]. The results presented a selectivity to H_2 of 92.7% for a H_2O/CH_4 molar ratio over 0.5, and a methane conversion of 91.6% at a H_2O/CH_4 ratio of 1. Nanocarbon powder, CO_2, C_2H_2, C_2H_4, and HCN were detected as side products [140].

Chapter 4

4. Experimental

4.1. Catalysts preparation

Two SiC monoliths (SiC1 and SiC2, respectively) were obtained by modelling commercial honeycomb monolith (Pirelli Ecotechnologies) in order to obtain quasi-circular samples. The monoliths were preliminary entrapped in a thermo-expandable ceramic mat (3M) before being placed in the reactor, thus avoiding any bypass phenomena. The geometric characteristics of the obtained monoliths are reported in **Table *5***.

Table 5: *geometric characteristics of the bare monoliths used for the preparation of the structured catalysts.*

	SiC 1	**SiC 2**
Diameter [cm]	4.1	6
Length [cm]	10.1	9
Number of channels	308	559
Walls thickness [mm]	0.6	0.6
Channels length [mm]	1.6	1.6
Total volume [cm^3]	133	254

The prepared monoliths were preliminarily heat-treated at 1000 °C for 48 h, in order to increase the washcoat adherence to the monolith, due to the formation of SiO_2 streaks on the SiC granules [141].

1 wt% of pseudobohemite (Pural SB; Sasol) and 1 wt% of methyl cellulose (Viscosity 4,000 cP; Sigma-Aldrich) were dissolved in a solution with pH = 3 (adjusted by HNO_3). 19 wt% of CeO_2 powder (Opaline®; Actalys HAS; Rhodia) was dispersed in this solution by means of strong stirring, so obtaining the washcoat slurry. The dip-coating procedure was used for the monolith impregnation, and the centrifugation at 1500 rpm for 5 minutes was used to remove the excess slurry. Subsequently, the washcoated monoliths were heat-treated first at 120°C for two hours and then at 850°C for three hours (the temperature increasing was of 10°C/min). This procedure was repeated until the monoliths were loaded with the wanted amount of washcoat (≈13wt% with respect the total weight). The active species was deposited onto the so obtained washcoated monoliths by impregnation in a $Ni(NO_3)_2$ aqueous solution ($Ni(NO_3)_2 \cdot 6H_2O$ was used as precursor, 99.999% trace metals basis, Sigma-Aldrich). The same heat-treating procedure used after the washcoat deposition was used after the catalyst deposition. The Ni loading obtained on the monoliths was of 7% on SiC1 and of 15% on SiC2, with respect to the washcoat weight, corresponding to about 1wt% and 2wt% with respect to the total weight. The two samples were named, respectively, NiWSiC1 and NiWSiC2. In Figure 13, the catalyst NiWSIC1 is shown, as an example.

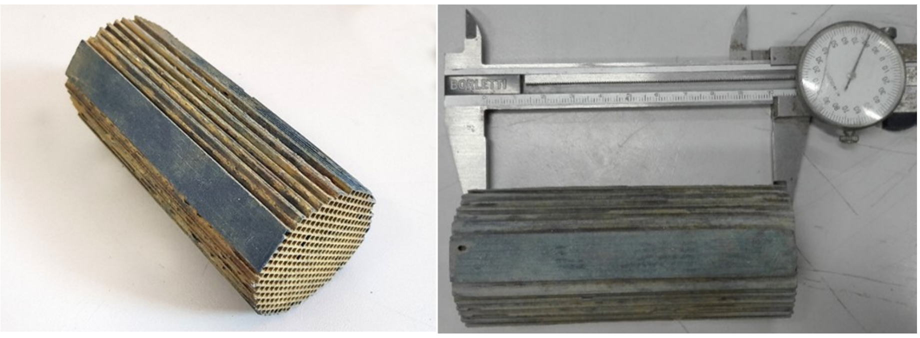

Figure 13: *two different views of the sample NiWSiC1 prepared for the microwave-assisted methane steam reforming.*

4.2. Catalysts characterization

Different techniques were used for the characterization of the fresh and spent catalysts, aiming to correlate their physiochemical properties with samples activity and stability. In the following paragraphs, the different techniques, including X-ray fluorescence (XRF), X-ray diffraction (XRD), Hg-intrusion porosimetry, Scanning Electron Microscopy (SEM), ultrasound adherence test and N_2 physisorption at -196°C, will be briefly described.

4.2.1 X-ray Fluorescence (XRF)

The chemical composition of the samples was determined by X-ray fluorescence (XRF) spectrometry in a ThermoFischer QUANT'X EDXRF spectrometer equipped with a rhodium standard tube as the source of radiation; a compressed tablet of the powder was analysed by the Fundamental Parameters method.

4.2.2 X-ray Diffraction (XRD)

X-ray power diffraction (XRD) patterns were recorded under a CuKα radiation (λ=1.5406 Å) using a D-8 Advance Bruker WAXRD instrument and Scherrer formula was employed to evaluate crystallites dimensions; the samples were scanned over a 2Θ range of 10–80° with a step of 0.05°.

4.2.3 Hg-intrusion porosimetry

The porosity and pore size distribution of the samples before and after the washcoat and active species deposition were evaluated by Hg penetration technique, with a "PASCAL 140" and "PASCAL 240" (Thermo Finnigan Instruments).

4.2.4 Scanning Electron Microscopy (SEM)

Images for the sample characterization were recorded by means of a Scanning Electron Microscope (SEM mod. LEO 420 V2.04, ASSING), coupled to an Energy Dispersive X-Ray analyser (EDX mod. INCA Energy 350, Oxford Instruments), for the evaluation of the active species dispersion.

4.2.5 Ultrasound adherence test

The adherence of the washcoat to the monoliths was evaluated by stressing the samples, immersed in a 100 mL petroleum ether (Carlo Erba reagenti) containing beaker, with a ultrasonic bath CP104 (EIA S.p.A.). The procedure implied using 60% of the rated power for a total of six cycles of 5 minutes each, at 25°C. After each cycle, the monoliths were heat-treated at 120°C for 1 hour, cooled, and the weight loss percentage was calculated according to (*Equation 20*, in which the weight of the carriers was not considered.

$$weight\ loss = \frac{Final\ mass - Initial\ mass}{Initial\ washcoat\ mass} * 100 \qquad (Equation\ 20)$$

4.2.6 N_2 physisorption at -196°C

The deposited layer on the carrier was characterized thorough N_2 physisorption at −196 °C, by means of NOVAtouch sorptometer, with the porosimetric features calculated through Barrett-Joyner-Halenda (BJH) method, and the specific surface area calculated through Branauer-Emmet-Teller (BET) method.

4.3. Laboratory plants

The microwave-assisted catalytic activity tests were performed by using an ad-hoc set-up laboratory plant, composed of the feeding, reaction and analysis sections, in two different configurations, as below specified.

4.2.1 First lab plant configuration

The first lab plant configuration is shown in Figure 14.

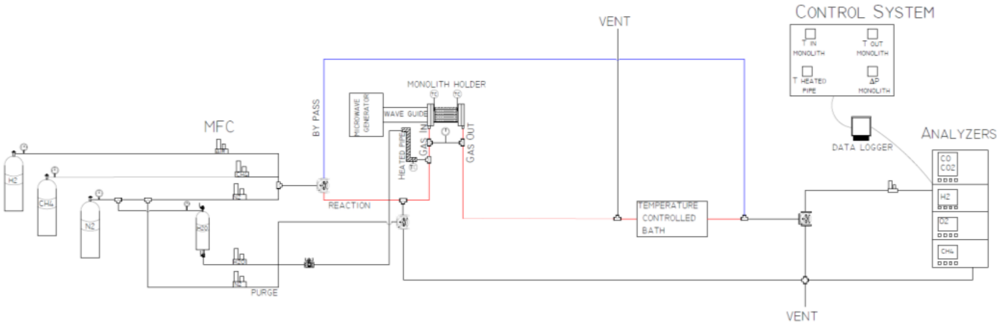

Figure 14: *first configuration of the experimental plant used for the microwave-assisted methane steam reforming process.*

The test bench is divided in three sections, which are also shown in Figure 14:

a. Gas feeding section;
b. Reaction section;
c. Analysis section.

The feed section is made up of different mass flow-controllers (MFC) for gases (CH_4 and N_2) and liquid (H_2O) admission.

The MFC consists of a thermal mass flow sensor (thermal mass flow instruments make use of a bypass, i.e., capillary bypass or bypass sensor) and a precise control valve.

The MFCs are all provided by Brooks, and an analogic control panel is used. The microwave apparatus includes: i) a power supply that allows to smoothly and stepless adjust the magnetron output power up to 2000 W, driven by an external analogical signal; ii) a 2.45GHz water cooled 2 kW Magnetron head, fitted on a suitable launcher. The latter is connected to a circulator with a water dummy load, in order to protect the magnetron from the reflected power. A dual bidirectional coupler is used for measuring the forward and reflected power. The coupler is fitted on a waveguide at the output of the circulator. Moreover, a motorized three stub tuner is fitted on the waveguide at the coupler output in order to match the load impedance and minimize the amount of reflected power. Preliminary heating tests were performed in order to verify the possibility to heat the monolith by using the microwaves and, also important, to verify the microwaves absorption behaviour of the structured catalyst, since the control system is able to continuously monitor the reflected and absorbed microwave power. The tests were carried out in a stainless-steel cylindrical reactor (internal diameter = 900 mm) (Figure 15a), at atmospheric pressure, by feeding N_2 at various low rates, and by varying the microwave power. After having verified that the SiC-based structured catalyst absorbs all the microwaves, a more compact plant was designed and set-up. In this system, the magnetron was placed directly in front of the monolith (Figure 15b).

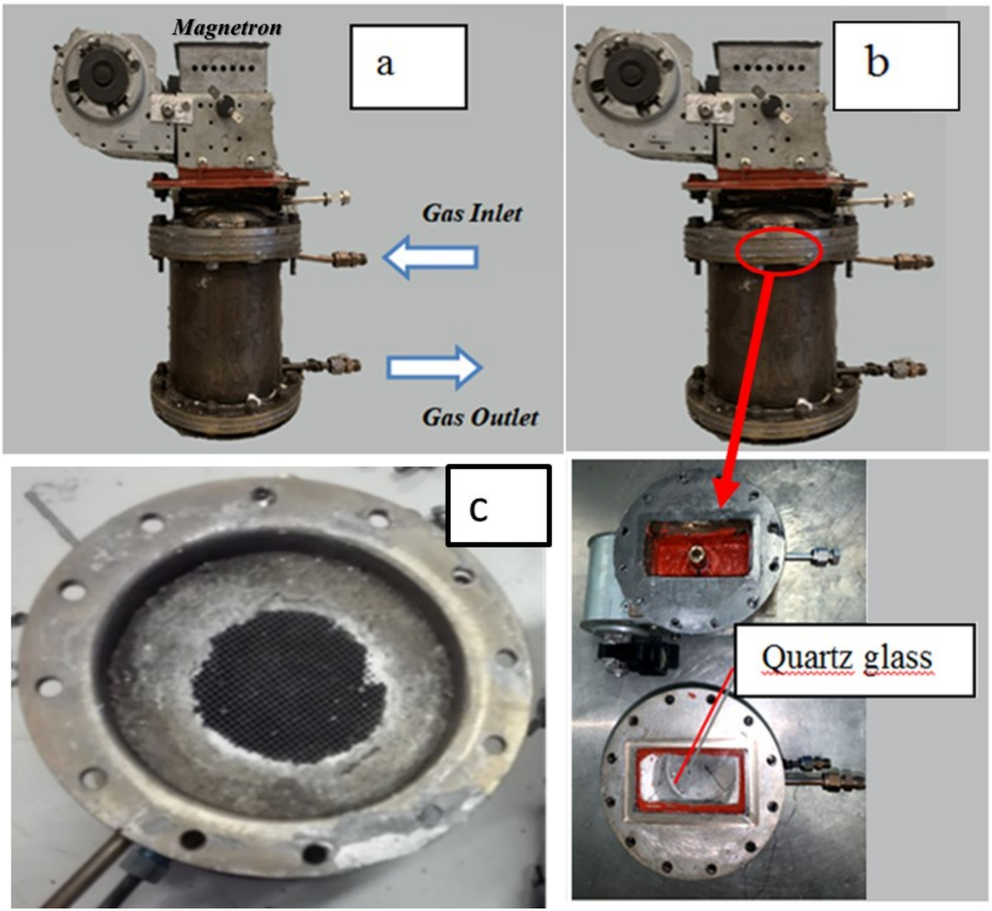

Figure 15: *magnetron and stainless-steel reactor, (a) with the gas inlet and oulet, (b) with the quartz glass specification, and (c) the SiC monolith placed in the reactor.*

A heated coil placed at the inlet of the reactor was used for the preliminarily vaporization of the water before its mixing to the cold gaseous feed. The pressure and temperature were continuously monitored by using specific sensors, the thermocouples were placed at the centre of the inlet and outlet sections of the monolith. The gas stream leaving the reactor was online monitored on dry bases after the condensation of the water vapour, using an on-line ABB analyser, equipped with a non-dispersive infrared analyser Uras 14 and a thermal conductivity detector Caldos 17, for the continuous monitoring of CO, CO_2, CH_4 and H_2.

4.2.2 Second lab plant configuration

The second plant configuration comprises the feeding, reaction, and analysis sections, as reported in the previous sub-section. In this configuration, both the reactor and the plant set-up have been optimized, in order to demonstrate the compactness of the proposed technology. A 2.45GHz air cooled 2 kW magnetron head, properly coupled to the reactor, was used for microwaves generation, whose output power was adjusted through a power supply driven by an external analogical signal. The reactor configuration was optimized with the aim of intensifying the electric field in the catalytic zone with respect to the classical one [142]. A detailed review of current literature, coupled to the CFD modelling of the reactor performed by using the COMSOL Multiphysics software (descripted in the following chapters), allowed to find that the reactor internal section could have a restriction of the middle section (where the structured catalyst could be placed) with respect to the inlet and outlet sections, in order to intensify the microwaves electric field in that zone [143, 144]. Consequently, a modification of the electric field propagation can be obtained, with the result of having better performance of the system. The reactor configuration (Figure 16a) was then designed and built.

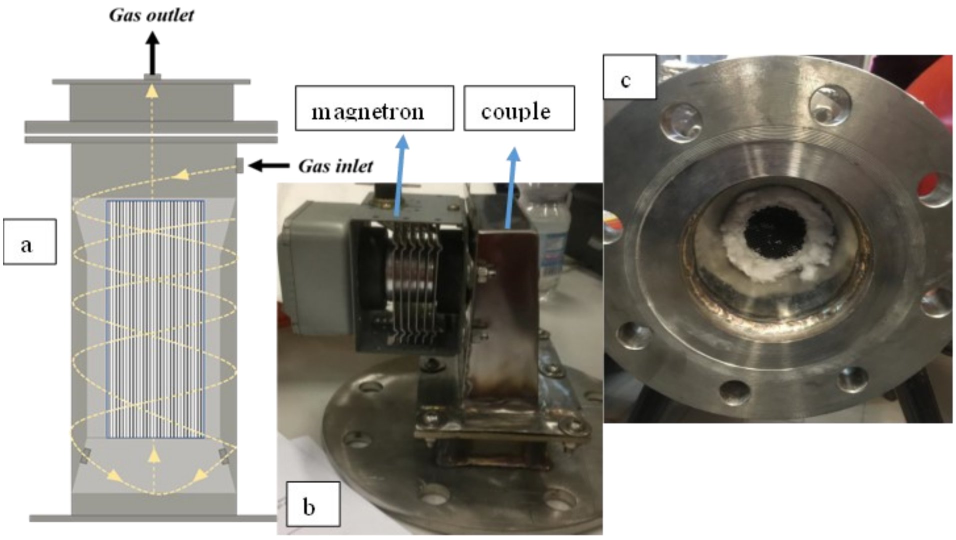

Figure 16: *a) reactor configuration; b) magnetron and coupler to the reactor, and c) catalyst NiWSiC1 inside the reactor.*

In this configuration, the gas enters from the top, passes through the inner interspace, and then enters in the reactor from the bottom. The magnetron was connected to a properly designed coupler (Figure 16b), in order to avoid any reflection phenomena. The internal section, in which the structured catalyst was placed, has a diameter of 6.5 cm and a length of 7.5 cm (Figure 16c). Moreover, the gas stream leaving the reactor was online continuously monitored on dry bases after the condensation of the water vapour, using a mass spectrometer (Pfeiffer Omnistar).

Regarding the plant set-up, in Figure 17 a picture of the final second configuration plant is shown, with evidence of the reactor, highlighting the compactness of the final installation.

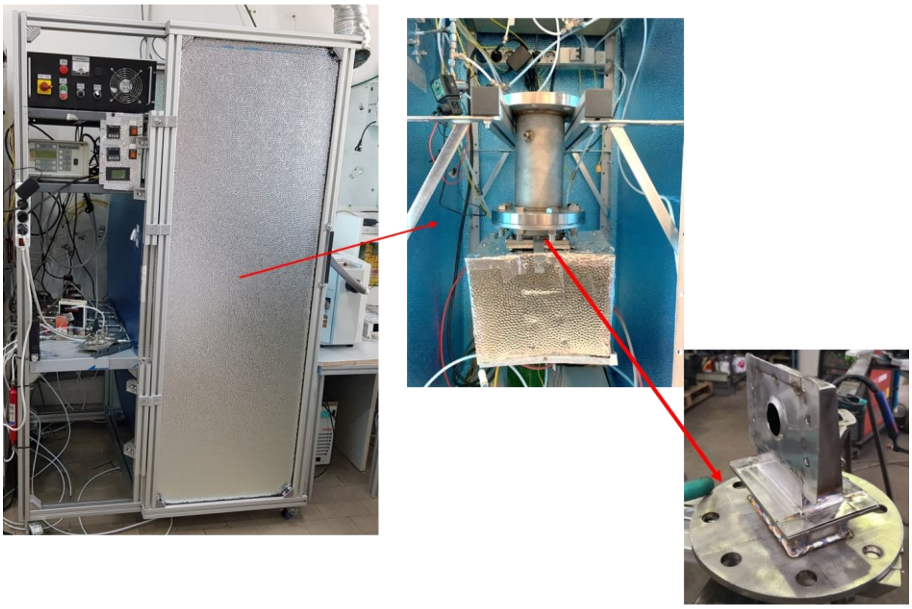

Figure 17: *(left) second configuration of the lab plant for the MW-assisted catalytic tests, (middle) reactor and magnetron, (right) coupler to magnetron and closing flange.*

In the second configuration plant, two main important features are present: (i) a compact microwave generator (shown in black in the upper part of the left side of Figure 17, with the possibility to choose the microwave power either in manual or in automatic mode) and a controller with which it is possible to set a temperature ramp and ensure that the Set Point is gradually reached, at a predetermined time (so working in automatic mode with the microwave generator).

4.3 Measurements of the temperature profile in the SiC monolith when irradiated by microwaves

During this Ph.D. thesis many efforts have been devoted to the deep understanding of the thermal phenomena occurring in the SiC monolith in both radial and axial directions when exposed to microwaves. Aiming at identifying the temperature profiles, properly designed experimental tests have been performed by using the second reactor configuration, as below described. First of all, a bare SiC monolith with the same dimensions of the catalytic one was used, and an inert gas with different flow rates (Ar, 0, 2 and 4 NL/min) has been fed. The tests have been performed at the same MW power set at 255W, with the following procedure:

1. The microwave generation system has seen an initial heating ramp set to "*manual*" up to a temperature of 330 °C.
2. After the achievement of this temperature, by means of the system controller and relay and then switching to "*auto*" the system previously shown, a temperature of the system of about 300 °C has been set.
3. Once the system reached a thermal steady-state, the microwave generator was turned off, acquiring the data concerning the cooling.

For the temperature measurements, optical fibers properly designed for operating under electromagnetic fields (Optocon TS2), to the FOTEMP-OEM-PLUS thermometer. This device is equipped with four measurement channels, analog/digital outputs and a communication port that can be used for real-time data acquisition with the help of Fotemp Assistant software.

The positioning of the optical fibers for the thermal analysis was crucial. They were arranged, as shown in the following figure, in such a way as to fall within a single quadrant of the monolith itself, thus allowing to acquire a temperature at the center, at the wall and at a midpoint center-wall thus obtaining a radial profile of the monolith, and they were represented as CH2, CH3 and CH4.

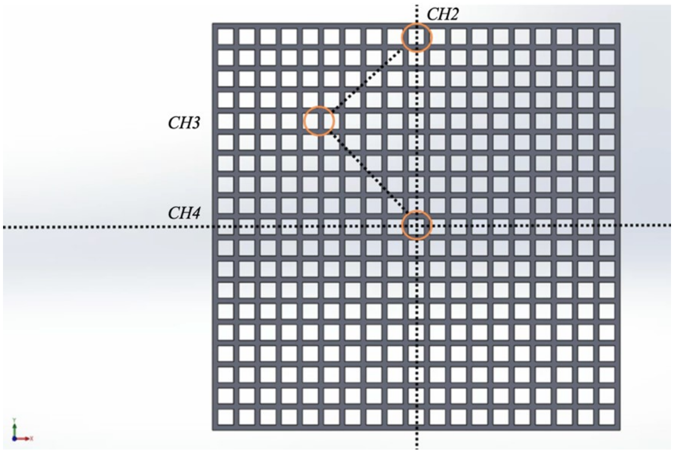

Figure 18: *Top view of the monolith and highlighted positioning of the optical fibers.*

The same arrangement was reproduced at different points of the height (INLET, MID, OUTLET,) of the monolith to acquire the same radial results on the *z-axis*. It was performed also an axial Temperature evaluation, disposing the fibers in staggered position on the monolith's height.

A thermocouple to acquire was used the Temperature data of the inert gas passing through the monolith's channels.

To have a better comprehension of the whole characterization process, a table is reported in the following that synthesize all the performed tests.

Table 6: *Test performed for the thermal characterization of the system.*

TEST TYPOLOGY	SiC RADIAL PROFILE	SiC AXIAL PROFILE
FREQUENCY [Mhz]	2450	2450
OUTPUT POWER [W]	255	255
Ar FLOW RATE [NL/min]	0-2-4	0-2-4
INLET - MID - OUTLET POSITIONING	YES	YES
STARTING T [°C]	T_{AMB}	T_{AMB}
T BEFORE THE FINE POWER CONTROL [°C]	330	330
COOLING TARGET T [°C]	T_{AMB}	T_{AMB}

In the following chapters the test above reported will be better represented, using an isometric projection of the chosen configuration.

4.3.1 *SiC monolith radial profile*

The isometric projections of the monolith drilled for the acquisition of temperatures are reported below (Figure 19). It is possible to note the layout adopted, chosen in order to have a temperature measurement in the radial direction in three sections: INLET, MID, OUTLET.

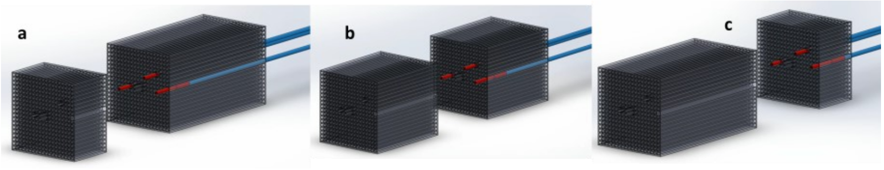

Figure 19: *Isometric projection of the SiC monolith. (a) inlet, (b) mid, (c) outlet positions.*

4.3.2 *SiC monolith axial profile*

Here is the isometric projection of the configuration adopted for the axial temperature measurements, in which the fibers have been located close to the inlet, middle and outlet section of the monolith.

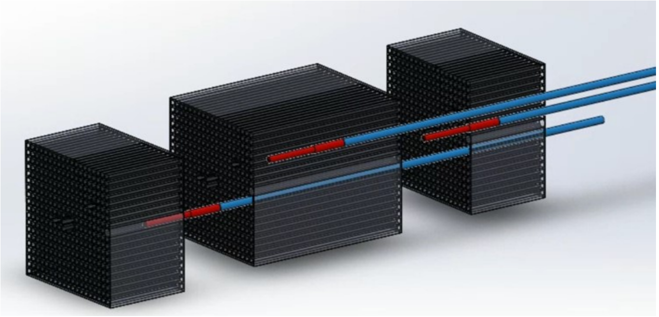

Figure 20: *Isometric projection of the SiC monolith. INLET, MID, OUTLET acquisition position (AXIAL).*

4.4 MW-assisted catalytic activity tests

The catalytic activity tests were performed using the same reactor, by supplying a feeding stream with a Steam/Carbon ratio of 3 and Nitrogen/Carbon ratio of 3, at gas hourly space velocities (GHSV) of 3300 and 5000 h^{-1} (calculated as the ratio between the volumetric flow rate and the overall volume, included the monolith). The tests were performed by varying the microwave power up to reaching the desired reaction temperature. The structured catalysts were preliminarily in-situ reduced, by feeding a stream (flow rate of 1000 mL/min) composed of 24% of H_2 diluted in N_2, from 20 to 850°C using the microwaves as heat source. The catalytic performance was evaluated in terms of methane conversion and hydrogen yield, defined in (*Equation 21* and (*Equation 22*, respectively.

$$Y_{H_2} = \frac{F_{H_2,out}}{4*F_{CH_4,in}}$$

$$X_{CH_4} = \frac{F_{CH_4,in} - F_{CH_4,out}}{F_{CH_4,in}} \qquad (\textit{Equation 21})$$

$$Y_{H_2} = \frac{F_{H_2,out}}{4*F_{CH_4,in}} \qquad (\textit{Equation 22})$$

In which F_{IN} and F_{OUT} represent the molar rate on the indicated species at the inlet and outlet of the system.

During all the tests, the power absorbed by the electric grid was continuously monitored, in order to calculate the energy efficiency of the system.

The energy efficiency was calculated by applying the classical equation of the thermal balance ((Equation *23*).

$$\text{IN} - \text{OUT} + \text{GEN} = \text{ACC} \qquad (\textit{Equation 23})$$

In which ACC = 0 since the thermal balance refers to the stationary state.

The thermal balance is expressed as follows (*Equation 24*):

$$(F_{CH4,in} \cdot cp_{CH4,in} + F_{N2,in} \cdot cp_{N2,in}) \cdot (T_{gas,in} - T_{rif}) + F_{H2O,in} \cdot cp_{H2O,in} \cdot (T_{H2O,in} - T_{rif}) - (F_{CH4,out} \cdot cp_{CH4,out} + F_{N2,out} \cdot cp_{N2,out} + F_{H2O,out} \cdot cp_{H2O,out} + F_{CO2,out} \cdot cp_{CO2,out} + F_{CO,out} \cdot cp_{CO,out} + F_{H2,out} \cdot cp_{H2,out}) \cdot (T_{gas,out} - T_{rif}) - (F_{CH4,in} - F_{CH4,out}) \cdot \Delta H^{\circ}_{R,Trif,}\ SR + (F_{CO2,in} - F_{CO2,out}) \cdot \Delta H^{\circ}_{R,Trif,} WGS + Q_{MW} - Q_{diss} = 0 \qquad (\textit{Equation 24})$$

In which:

F_i = molar flow rates in and out from the reactor,
c_p = specific heat,
$T_{gas,\ in}$ =temperature at the inlet, fixed at 25°C,
$T_{gas,\ out}$ = temperature at the outlet of the reactor,
T_{rif} = reference temperature, 25°C,
$T_{H2O,\ in}$ = temperature of H_2O at the inlet, 200°C,
$\Delta H^{\circ}_{R,Trif}$ = standard enthalpy at 25°C,
Q_{MW} = heat supplied by means of microwaves,
Q_{diss} = heat dissipated by the system

The catalytic activity tests were performed under the operating conditions reported in **Table** *7*.

Table 7: *operating conditions of the microwave-assisted catalytic activity tests*

Sample	**GHSV [h^{-1}]**	**Q_{in} CH_4 [m^3/h (STP)]**	**Q_{in} H_2O [m^3/h (STP)]**	**Q_{in} N_2 [m^3/h (STP)]**	**Q_{tot} [m^3/h (STP)]**
NiWSiC1	3300	0.06	0.19	0.19	0.44
	5000	0.10	0.29	0.29	0.67
NiWSiC2	3300	0.12	0.36	0.36	0.84
	5000	0.18	0.54	0.54	1.26

The tests were performed according to the following procedure:

1. The system is fed with only N_2, in order to achieve the desired GHSV;
2. After about 1 min, the microwave heating was set on, and when the system reached the temperature of about 550°C, methane and H_2O were added, always keeping the desired GHSV.

4.5 Kinetic measurements

The experimental tests have been also used for the determination of the kinetic parameters. In particular, in order to assume differential reaction conditions with negligible heat and mass transfer effects, the data regarding the catalytic performance of the system far from the thermodynamic equilibrium conditions were considered for developing the model.

For the numerical analysis, MSR and WGS reaction (respectively Eq. 1 and Eq. 2) were supposed to occur, and the reaction rate considered to estimate the kinetic parameters was expressed by (*Equation 25*) for the former and (*Equation 26*) for the latter. The reaction rate expression follows the approach proposed by Haberman and Young [145].

$$-r_{SR} = k_{SR}\left(P_{CH_4}P_{H_2O} - \frac{P_{H_2}{}^3 P_{CO}}{K_{eq,SR}}\right) \qquad (Equation\ 25)$$

$$-r_{WGS} = k_{WGS}\left(P_{CO}P_{H_2O} - \frac{P_{CO_2}P_{H_2}}{k_{eq,WGS}}\right) \qquad (Equation\ 26)$$

$$-r_{SR} = k_{SR}\left(P_{CH_4}P_{H_2O} - \frac{P_{H_2}{}^3 P_{CO}}{K_{eq,SR}}\right)$$

$$k_i = k_{0,i} \cdot e^{\frac{-E_{a,i}}{RT}} -r_{SR} = k_{SR}\left(P_{CH_4}P_{H_2O} - \frac{P_{H_2}{}^3 P_{CO}}{K_{eq,SR}}\right)$$ (*Equation 27*)

In the above reported expressions, P_i is the partial pressure of the “i” component, while k_i is the reaction rate constant, according to the Arrhenius law (*Equation 27*), where the parameters $k_{0,I}$ and $E_{a,i}$ correspond respectively to the pre-exponential factor and to the activation energy. The equilibrium constants of the two reactions are expressed as (*Equation 28* for MSR and (*Equation 29* for WGS.

$$K_{eq,SR} = 1.0267 \cdot 10^{10} \cdot \exp(-0.2513 \cdot Z^4 + 0.3665 \cdot Z^3 + 0.5810 \cdot Z^2 - 27.134 \cdot Z + 3.2770)\ [Pa^2]$$

$$K_{eq,SR} = 1.0267 \cdot 10^{10} \cdot \exp(-0.2513 \cdot Z^4 + 0.3665 \cdot Z^3 + 0.5810 \cdot Z^2 - 27.134 \cdot Z + 3.2770)\ [Pa^2]$$

$$-r_{WGS} = k_{WGS}\left(P_{CO}P_{H_2O} - \frac{P_{CO_2}P_{H_2}}{k_{eq,WGS}}\right) -r_{SR} = k_{SR}$$

$$4.1788 \cdot Z + 0.3169)$$

$$K_{eq,SR} = 1.0267 \cdot 10^{10} \cdot \exp(-0.2513 \cdot Z^4 + 0.3665 \cdot Z^3 + 0.5810 \cdot Z^2 - 27.134 \cdot Z +$$

$$4.1788 \cdot Z + 0.3169) 3.2770)\ [Pa^2]$$

$$-r_{WGS} = k_{WGS}\left(P_{CO}P_{H_2O} - \frac{P_{CO_2}P_{H_2}}{k_{eq,WGS}}\right)$$

$$2513 \cdot Z^4 + 0.3665 \cdot Z^3 + 0.5810 \cdot Z^2 - 27.134 \cdot Z +$$

$$-r_{WGS} = k_{WGS}\left(P_{CO}P_{H_2O} - \frac{P_{CO_2}P_{H_2}}{k_{eq,WGS}}\right) -r_{SR} = k_{SR}\left(P_{CH_4}P_{H_2O} - \frac{P_{H_2}{}^3 P_{CO}}{K_{eq,SR}}\right)$$

The mass balances on the single components led to the obtainment of a set of equations, solved by applying the Eulero method by means of the Excel software. For each operating condition, the experimental value x_{exp} and the corresponding kinetic model solution x_{mod} were compared, and an objective function was defined as (*Equation 31*. The minimization of the objective function (through the Solver of the Excel software) leaving the kinetic parameters ($E_{a,i}$ and $k_{0,i}$) as degrees of freedom for the solution, allowed the achievement of very close experimental and modelled values. The optimization procedure was performed several times with various initial values of the parameters, with the aim to confirm the robustness of the optimization scheme.

$$f = \min\left(\sum_{c=1}^{n}(x_{exp_c} - x_{mod_c})^2\right)$$ (*Equation 31*)

$$-r_{SR} = k_{SR}\left(P_{CH_4}P_{H_2O} - \frac{P_{H_2}{}^3 P_{CO}}{K_{eq,SR}}\right)$$

Chapter 4

Chapter 5

5 CFD Modelling

5.1 CFD modelling of the catalytic reactor for the MW-assisted tests

One of the main challenges in the development of microwave heating-based technologies is the proper design of the microwave cavity, in particular with the aim to scale-up a MW-assisted reactor. In fact, the sensitive nature of the standing wave pattern of the electric and magnetic fields and the ineffective heating of the reactor due to the penetration depth becoming smaller than the reactor size make this step very difficult. Therefore, these drawbacks must be overcome for a widespread application of MW heating in chemical processes. In this sense, the fast progress in computational resources and the availability of user-friendly Multiphysics commercial software could be helpful, for example, in providing the exact distribution of the 3D temperature and electromagnetic field in a microwave cavity and reactor [146]. However, progress in CFD goes on slowly with respect to the advances in experimental tests. In fact, the presence of different aspects which must be considered makes the modelling of microwave multiphase reactors very challenging, aspects which are related to the peculiar nature of the reactors, simultaneously being multiphase (they are characterized by the presence of more than one phase, such as gas and solid or gas and liquid), Multiphysics (they are characterized by the presence of different physics, such as electromagnetism, transport processes and chemical reactions) and multiscale (they are characterized by a variable length scale, from a single catalyst particle to the microwave cavity). Due to these difficulties, few comparative studies are present in which the simulation results are validated with experimental tests [147 - 151]. In any case, the majority of these studies have been performed considering only single-phase systems, such as the microwave heating of liquids in a glass vial [147, 148, 151]. In the case of multiphase systems, several simplifications are needed to effectively manage the complexity of the system and obtain the results in a reduced computational cost. For example, some studies are available in which a multiphase fixed bed reactor, constituted by uniformly arranged large particles [29], biphasic solid hydride [152] and zeolites [143, 153], was considered a continuum, and in the simulations the experimentally measured effective permittivity of the sample was employed. However, these simplifications should be carefully chosen, since they can introduce large uncertainties in the model predictions, which can result in uncertainties for the reactor design.

Starting from this literature review, as mentioned in the previous chapters, another objective of this work was to represent the experimentally known system by means of a multiphysical system modelling. The COMSOL Multiphysics 5.6 software was used for this purpose. This software is widely used for engineering applications and provides the user with a wide range of physics that can be used and coupled to obtain satisfactory results as close to reality as possible. First, the overall system, comprising the reactor and the monolith, was drawn by using the COMSOL CAD (Figure 21).

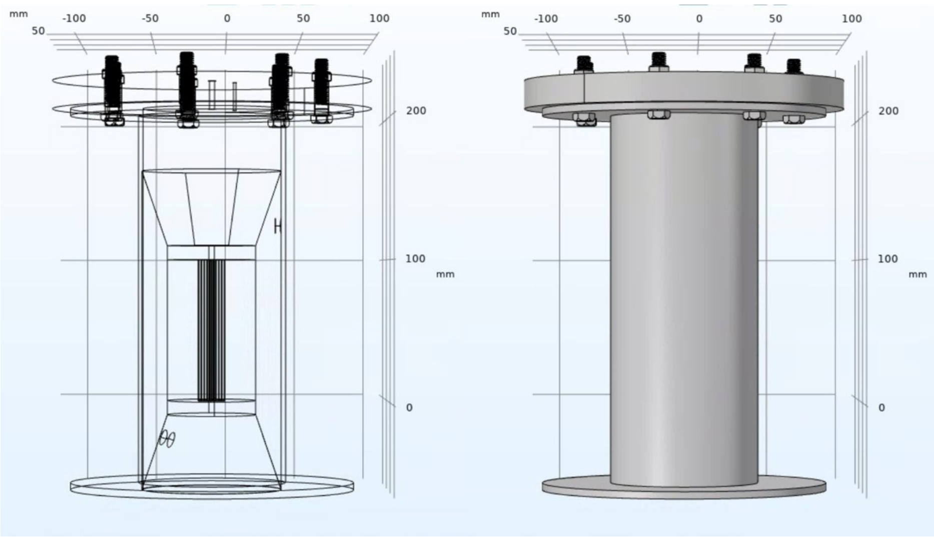

Figure 21: *xy representation of the entire geometry uploaded to the COMSOL Multiphysics software, with the evidence of the SiC monolith inside the reactor (left).*

The next steps were the implementation of the materials and the setting of the physics. With regards to the physics, the MW heating system interests both the electromagnetism and the heat transfer in a solid material. In particular, in order to predict the distribution of the electric field and the temperatures distribution when the microwave's heating system is on, the physics "Electromagnetic Waves (Frequency domain)", "Heat transfer in Solids" and "Laminar Flow" were used. The selected mesh for performing these simulations was the "physics controlled" one, in order to permit the software to automatically optimize the mesh for all the domains. For each physics, the following equations and boundary conditions have been used.

5.1.1 ELECTROMAGNETIC WAVE, FREQUENCY DOMAIN (EMW)

The first equation to be presented in this physics is the wave equation. This comes from Maxwell's equations and calculates the distribution of the electromagnetic field throughout the domain within the microwave-assisted reactor.

$$\nabla * {\mu_r}^{-1} * (\nabla * \boldsymbol{E}) - {k_0}^2 * \left(\varepsilon_r - \frac{j * \sigma}{\omega * \varepsilon_0}\right) * \boldsymbol{E} = \boldsymbol{0} \qquad (\textit{Equation 32})$$

The chosen port for the microwaves used in this physics is defined as "circular", whose equation is below reported.

$$\mathrm{S} = \frac{\int_{\partial\Omega} (E - E_1) * E_1}{\int_{\partial\Omega} E_1 * E_1} \qquad (\textit{Equation 33})$$

$$\mathrm{S} = \frac{\int_{\partial\Omega} (E - E_1) * E_1}{\int_{\partial\Omega} E_1 * E_1}$$

This equation calculates the scattering "S" parameter, a parameter that quantifies the power not absorbed by the material absorbing the microwaves, so, the power that is reflected to the source. E1 represents the input electric field vector at the gate.

The following boundary conditions have been applied for this physics.

PEC (Perfect Electric Conductor): It implies that the tangential component of the electric field is zero and is applied to metal walls; these are assumed to be ideal conductors.

$$\mathrm{n} * \boldsymbol{E} = \boldsymbol{0} \qquad (\textit{Equation 34})$$

$$\mathrm{n} * \boldsymbol{E} = \boldsymbol{0}$$

Impedance Boundary Condition

$$\sqrt{\frac{\mu_0\mu_r}{\epsilon_0\epsilon_r - j\frac{\sigma}{\omega}}} * n * H + E - (n * E) * n = (n * E_s) * n - E_s$$

(*Equation 35*)

$$\sqrt{\frac{\mu_0\mu_r}{\epsilon_0\epsilon_r - j\frac{\sigma}{\omega}}} * n * H + E - (n * E) * n = (n * E_s) * n - E_s$$

5.1.2 LAMINAR FLOW (SPF & SPF2)

In fluid dynamics we speak of laminar flow or laminar regime when fluid motion occurs with infinitesimal layers sliding over each other without any kind of fluid mixing, not even on a microscopic scale. The flow is governed by viscous forces and is constant in time. At the lowest velocity, it is called *Stokes flow*, and is governed by the *Stokes equations.*

Below are the same equations and boundary conditions for the two laminar flow physics used individually for the jacket and later for the waveguide. The fluid dynamic results of the two physics were then coupled into the heat transfer physics to set up a proper profile development.

A correct setting of this physics was essential for a successful simulation. The gas paths within the system are a must for the resolution as the system is characterized by a flow-through behaviour.

The first equation is the governing equation of physics.

$$\rho * \frac{\partial \mathbf{u}}{\partial t} + \rho * (\boldsymbol{u} * \nabla) * \boldsymbol{u} = \nabla * [-p * \boldsymbol{I} + \boldsymbol{K}] + F$$

(*Equation 36*)

$$\rho * \nabla * \mathbf{u} = \mathbf{0}$$

(*Equation 37*)

This is followed by equations that refer only to the domains of the system occupied by the fluid.

$$\rho * \frac{\partial \mathbf{u}}{\partial t} + \rho * (\boldsymbol{u} * \nabla) * \boldsymbol{u} = \nabla * [-p * \boldsymbol{I} + \boldsymbol{K}] + F$$

(*Equation 38*)

$$\rho * \nabla * \mathbf{u} = \mathbf{0}$$

(*Equation 39*)

$$\mathbf{K} = \mu * (\nabla \boldsymbol{u} + (\nabla \boldsymbol{u})^T)$$

(*Equation 40*)

Here are the boundary conditions set for this physics including: the no sleep condition at the walls, starting with the walls of the jacket, passing through those of the waveguide and ending with the walls of each individual channel that makes up the monolith; the input and output conditions that, as mentioned above, will prove to be fundamental for their coupling in the physics of heat transfer.

$$\mathbf{u} = \mathbf{0}$$

(*Equation 41*)

For the inlet condition, instead of a fluid velocity and a velocity range in the system, a maximum inlet flow rate of 2 NL/min was set, detailing the calculation of the velocity range at COMSOL itself.

$$-\int_{\partial\Omega} \rho * (\boldsymbol{u} * \boldsymbol{n}) d_{bc} * dS = m \qquad (\textit{Equation 42})$$

Exit 1

$$[-p * \boldsymbol{I} + \boldsymbol{K}] * \boldsymbol{n} = -\widehat{p_0} * \boldsymbol{n} \qquad (\textit{Equation 43})$$

$$\widehat{p_0} \leq p_0 \qquad (\textit{Equation 44})$$

5.1.3 HEAT TRANSFER IN SOLID (HT)

The governing equations used in this physics are as follows.

$$\rho * C_p * \frac{\partial T}{\partial t} + \rho * C_p * \boldsymbol{u} * \nabla T + \nabla * \boldsymbol{q} = Q + Q_{ted} \qquad (\textit{Equation 45})$$

$$q = -k * \nabla T \qquad (\textit{Equation 46})$$

$$\rho * C_p * \frac{\partial T}{\partial t} + \rho * C_p * \boldsymbol{u} * \nabla T + \nabla * \boldsymbol{q} = Q + Q_{ted}$$

Here the appropriate boundary conditions, with a thermal insulation condition.

$$-\mathbf{n} * \mathbf{q} = \mathbf{0} \qquad (\textit{Equation 47})$$

$-\mathbf{n} * \mathbf{q} = \mathbf{0}$As heat source, considering the microwave impact zone on one of the 4 external faces of the monolith, a boundary heat source condition was chosen, this one selected on the main face of the SiC monolith. The power on the surface has been set as 255 W in impact on the face, having in consideration the exposed surface on the monolith.

Of particular interest was the thermal conductivity of the monolith. Since it is a function of temperature, it was decided to carry out a function study on MATLAB based on experimental data proposed by NIST (National Institute of Standards and Technology) (Figure 22).

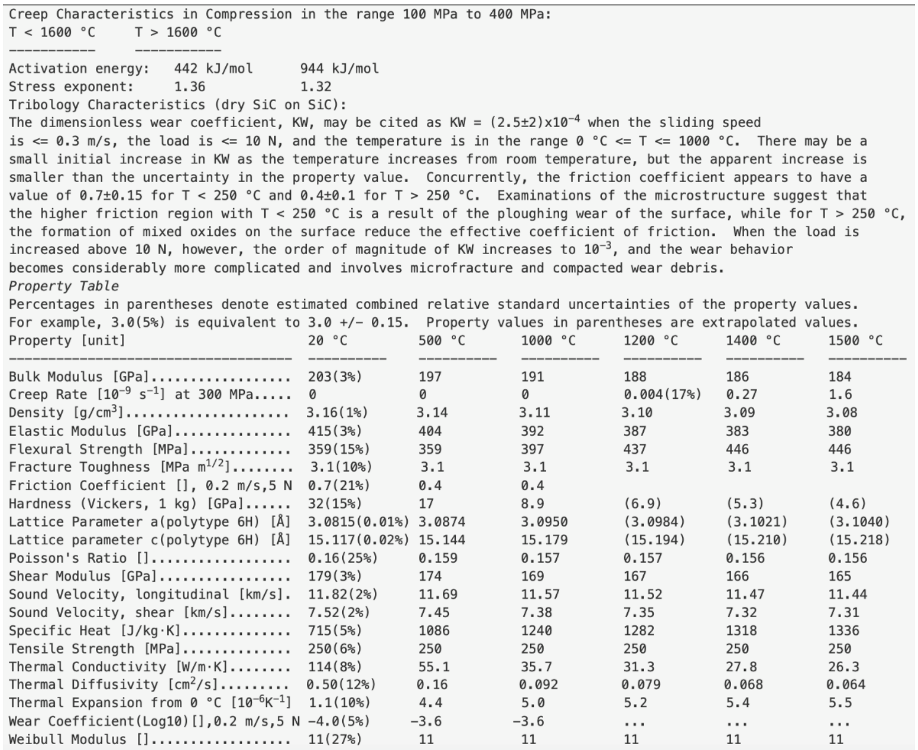

```
Creep Characteristics in Compression in the range 100 MPa to 400 MPa:
T < 1600 °C     T > 1600 °C
-----------     -----------
Activation energy:   442 kJ/mol      944 kJ/mol
Stress exponent:     1.36            1.32
Tribology Characteristics (dry SiC on SiC):
The dimensionless wear coefficient, KW, may be cited as KW = (2.5±2)x10⁻⁴ when the sliding speed
is <= 0.3 m/s, the load is <= 10 N, and the temperature is in the range 0 °C <= T <= 1000 °C.  There may be a
small initial increase in KW as the temperature increases from room temperature, but the apparent increase is
smaller than the uncertainty in the property value.  Concurrently, the friction coefficient appears to have a
value of 0.7±0.15 for T < 250 °C and 0.4±0.1 for T > 250 °C.  Examinations of the microstructure suggest that
the higher friction region with T < 250 °C is a result of the ploughing wear of the surface, while for T > 250 °C,
the formation of mixed oxides on the surface reduce the effective coefficient of friction.  When the load is
increased above 10 N, however, the order of magnitude of KW increases to 10⁻³, and the wear behavior
becomes considerably more complicated and involves microfracture and compacted wear debris.
Property Table
Percentages in parentheses denote estimated combined relative standard uncertainties of the property values.
For example, 3.0(5%) is equivalent to 3.0 +/- 0.15.  Property values in parentheses are extrapolated values.
Property [unit]                      20 °C         500 °C       1000 °C      1200 °C      1400 °C      1500 °C
------------------------------------ ----------    ----------   ----------   ----------   ----------   ----------
Bulk Modulus [GPa].................  203(3%)       197          191          188          186          184
Creep Rate [10⁻⁹ s⁻¹] at 300 MPa.....  0             0            0            0.004(17%)   0.27         1.6
Density [g/cm³]....................  3.16(1%)      3.14         3.11         3.10         3.09         3.08
Elastic Modulus [GPa]..............  415(3%)       404          392          387          383          380
Flexural Strength [MPa]............  359(15%)      359          397          437          446          446
Fracture Toughness [MPa m¹/²]........  3.1(10%)      3.1          3.1          3.1          3.1          3.1
Friction Coefficient [], 0.2 m/s,5 N 0.7(21%)      0.4          0.4
Hardness (Vickers, 1 kg) [GPa]......  32(15%)       17           8.9          (6.9)        (5.3)        (4.6)
Lattice Parameter a(polytype 6H) [Å] 3.0815(0.01%) 3.0874       3.0950       (3.0984)     (3.1021)     (3.1040)
Lattice parameter c(polytype 6H) [Å] 15.117(0.02%) 15.144       15.179       (15.194)     (15.210)     (15.218)
Poisson's Ratio []..................  0.16(25%)     0.159        0.157        0.157        0.156        0.156
Shear Modulus [GPa].................  179(3%)       174          169          167          166          165
Sound Velocity, longitudinal [km/s].  11.82(2%)     11.69        11.57        11.52        11.47        11.44
Sound Velocity, shear [km/s]........  7.52(2%)      7.45         7.38         7.35         7.32         7.31
Specific Heat [J/kg·K].............  715(5%)       1086         1240         1282         1318         1336
Tensile Strength [MPa].............  250(6%)       250          250          250          250          250
Thermal Conductivity [W/m·K]........  114(8%)       55.1         35.7         31.3         27.8         26.3
Thermal Diffusivity [cm²/s].........  0.50(12%)     0.16         0.092        0.079        0.068        0.064
Thermal Expansion from 0 °C [10⁻⁶K⁻¹] 1.1(10%)      4.4          5.0          5.2          5.4          5.5
Wear Coefficient(Log10)[],0.2 m/s,5 N -4.0(5%)     -3.6         -3.6          ...          ...          ...
Weibull Modulus []..................  11(27%)       11           11           11           11           11
```

Figure 22: *NIST properties data summaries of Silicon Carbide*

The data relevant to the thermal conductivity vs temperature have been used for obtaining an equation able to describe the functionality with respect to temperature as an independent variable, which could be entered in the "definitions" section on COMSOL Multiphysics and then called up in the SiC properties. In this way, by using a regression model, a third-order polynomial (*Equation 48*) was finally chosen because it have shown the best validation parameters (R2, ADJ R2, RMSE and SSE) and the best fitting within the desired range, as well as the best chaotic distribution of residuals.

$$f(x) = -4.102 * e - 08 * T^3 + 0.0001455 * T^2 - 0.1871 * T + 117.6$$

(*Equation 48*)

The function loaded into COMSOL Multiphysics was then graphically represented and set in the material properties.

5.2 Validation of the CFD modelling activities

The results of the simulations have been validated with the properly defined experimental tests described in the section 4.3., aiming at mapping the temperature of the SiC monolith when it is exposed to microwaves. In particular, the simulated temperature of the monolith in the outlet, middle and outlet sections has been compared with the experimental one both during the MW-assisted heating phase and in the stationary phase. The results of these comparisons are reported in the next chapter, both in figure and in table mode.

Chapter 5

Chapter 6

6 Results and discussion

6.1 Results of catalysts characterization

The XRD patterns related to a NiWSiC1 sample, compared with the ones related to CeO_2 and Pural SB calcined at 850°C and SiC powder, are reported in Figure 23.

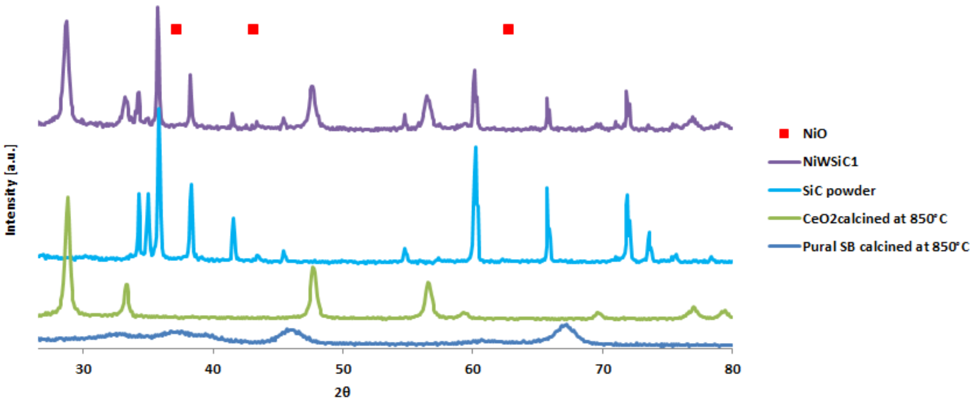

Figure 23: *XRD analysis for the NiWSiC samples.*

The XRD patterns have shown that the pseudohemite pural SB calcined at 850°C had transformed in γ-alumina, the ceria support calcined at 850°C, as expected, maintains the typical fluorite type cubic structure, while the SiC powder diffractogram was an overlapping of α- and β-silicon carbide structures [154], and the data are reported in **Table *8***. The NiWSiC1 patterns catalyst have shown the preponderance of SiC carrier and ceria support, while no evidence of nickel oxide was found, probably because of the low loading. Crystallite sizes were also evaluated, the results have shown the maintenance of the nanometric nature of the ceria support and SiC structure, despite repeated treatments at 850 ° C.

Table 8: *Crystallite sizes as calculated by XRD analysis.*

Sample	**Crystallite size (nm)**			
	SiC (111)	**Ni**	**γ-Al_2O_3 (440)**	**CeO_2 (111)**
CeO_2 powder calcined at 850°C	-	-	-	23
NiWSiC1	50	-	-	22
NiWSiC2	51	-	-	23
Pural SB calcined at 850°C	-	-	15	-
SiC powder	48	-	-	-

The characterization results of the prepared catalytic samples are summarized in **Table *9***, in which the comparisons with the washcoat powder and the bare SiC monoliths are also reported. The chemical composition obtained by ED-XRF was closer to the wanted one, thus demonstrating the good replicability of the coating procedure, and confirming the formation of a homogeneous washcoat slurry.

Table 9: *Chemical composition (wt%) and textural properties.*

Sample	**XRF [wt%]**				**SSA [m^2/g]**	**Pore D_m [μm]**
	SiC	**Ni**	**Al_2O_3**	**CeO_2**		
Washcoat powder	-	-	3.9	96.1	74.0	-
NiWSiC1	87.5	0.8	0.5	11.2	9.0	6.50
NiWSiC2	87.0	1.7	0.5	10.8	10.0	4.60
No calcined SiC bare monolith	100	-	-	-	0.3	20.00
Calcined SiC bare monolith	100				1.5	20.00

The data in **Table *9*** also show how the adding of the washcoat to the bare monoliths resulted in the decreasing of both the average diameter and volume of the pores. The peculiar characteristics of the starting SiC carrier led to this expected result: the washcoat not only deposits on the inner surface, but it also adheres to the inner walls of the pores (average pore diameter of about 17 μm), reducing their section and diameter, as reported in previous works [155].

Moreover, it is evident that the adding of the washcoat to the bare SiC monoliths allowed to increase the SSA from 1,5 up to 10 m^2/g, a very important result.

The results of the Hg-intrusion porosimetry are reported in detail as pore distribution and cumulative volume, respectively, vs pore diameter in Figure 26 and Figure 27 for the bare SiC monolith and the NiWSiC1 sample (as an example of final structured catalyst).

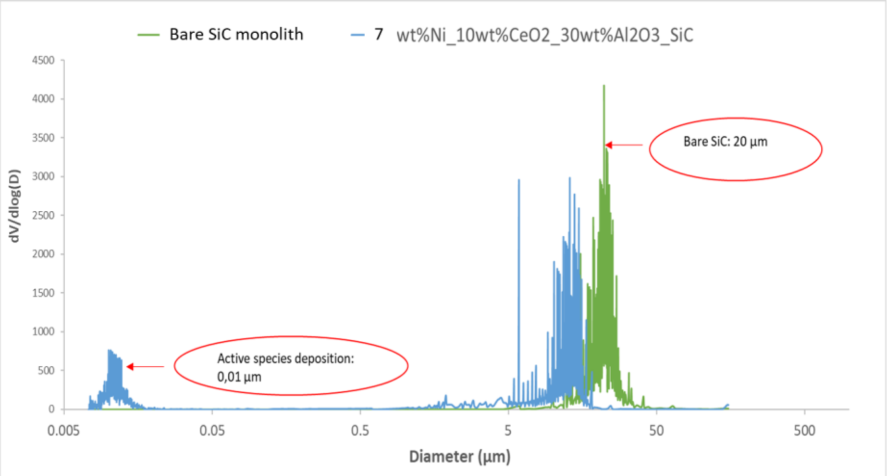

Figure 24: *Hg-intrusion porosimetry, pore distribution vs pore diameter.*

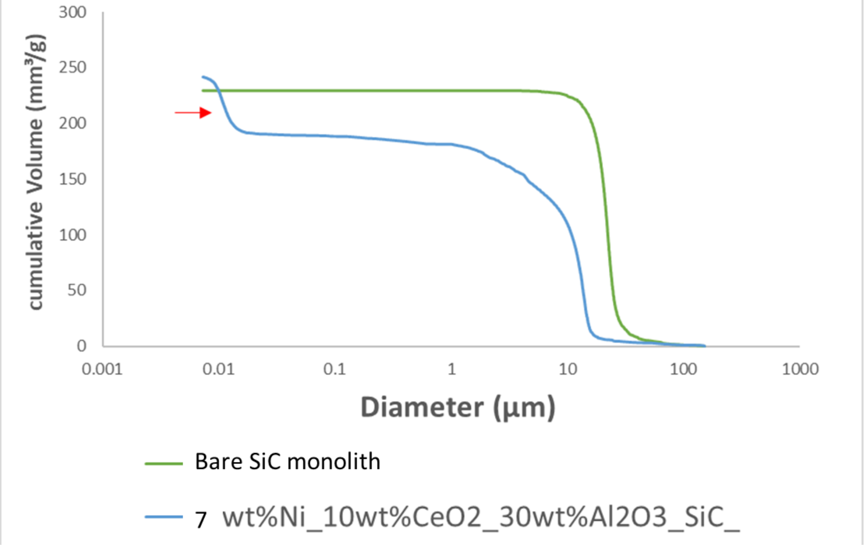

Figure 25: *Hg-intrusion porosimetry, cumulative volume vs pore diameter.*

The above reported results highlighted the effect of the washcoat and active species deposition on the SiC carrier. In particular, green and blue curves, relevant to the bare and catalytic SiC monolith, respectively, from Figure 26, the formation of pores with a diameter of about 0.01 µm after the catalyst deposition is evident, as well as from Figure 27, the presence of smaller pores is indicated by the increasing slope of the right part of the blue curve. Therefore, aiming at better charactering the catalytic sample, the N_2 adsorption-desorption technique has been employed, and the isotherms are reported in Figure 26, for each preparation step of the structured catalyst. In detail, the samples have been characterized after (a) alumina, (b) CeO_2, and (c) Ni consecutive loading to the SiC structure.

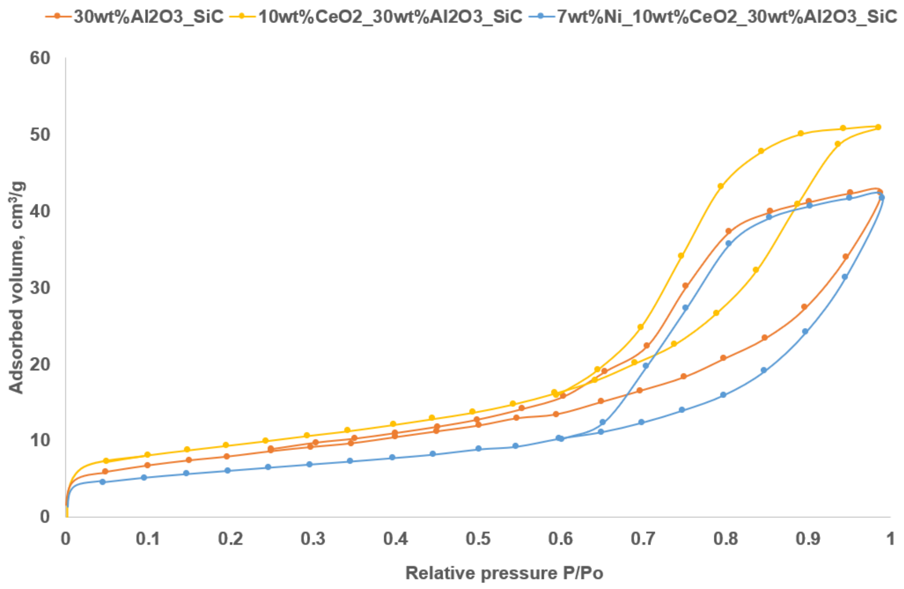

Figure 26: *N_2 adsorption-desorption isotherms for the structured catalyst NiWSiC for each preparation step.*

The data reported in Figure 26 evidenced that the curves are IV type ones, thus confirming the mesoporous nature of the deposited layer, with the presence of micropores. In particular, a slight decrease in the adsorbed volume can be observed after the CeO_2 addition. Moreover, the H2b hysteresis denotes the formation of disordered pores after the active species deposition. The porosimetric features are shown in Figure 27, as pore distribution vs radius.

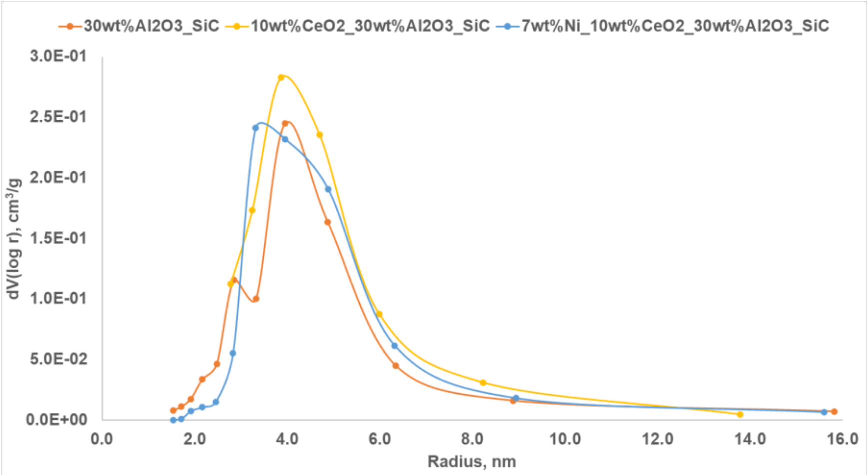

Figure 27: *porosimetric features of the NiWSiC catalyst after each preparation step, calculated through BJH method.*

The data in Figure 27 evidenced that the CeO_2 and Ni addition (yellow and blue curves, respectively) resulted in a monomodal pore distribution, with a radius of about 3 nm, highlighting that the active species deposition allowed the formation of a layer on the SiC carrier, as expected.

Some specific SEM images have been used for investigating the thickness of the deposited layer. One of these images, relevant to the NiWSiC1 sample, is shown in Figure 28.

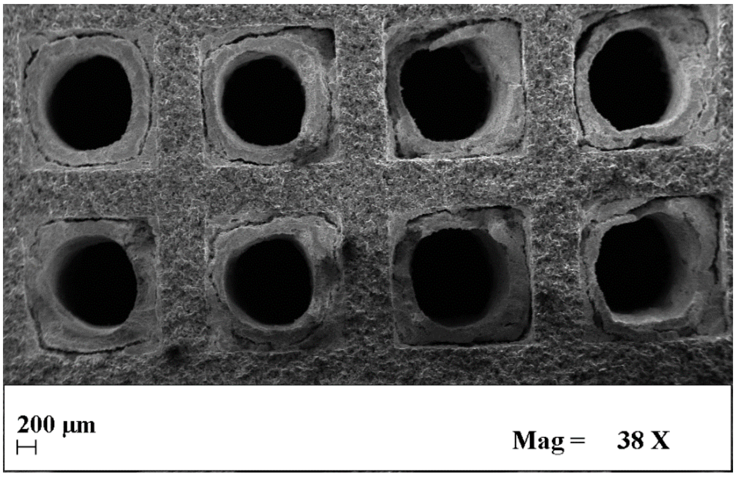

Figure 28: *SEM image of some frontal channels of the NiWSiC1 sample.*

As evident from Figure 28, the deposition of the catalytic layer resulted in the modification of the shape of the inlet section of the channels, which became quasi-circular. Moreover, it is possible to estimate that the layer had a thickness of about 200 µm.

The SEM images related to the bare SiC monolith and the final prepared catalyst NiWSiC1 are shown in Figure 29.

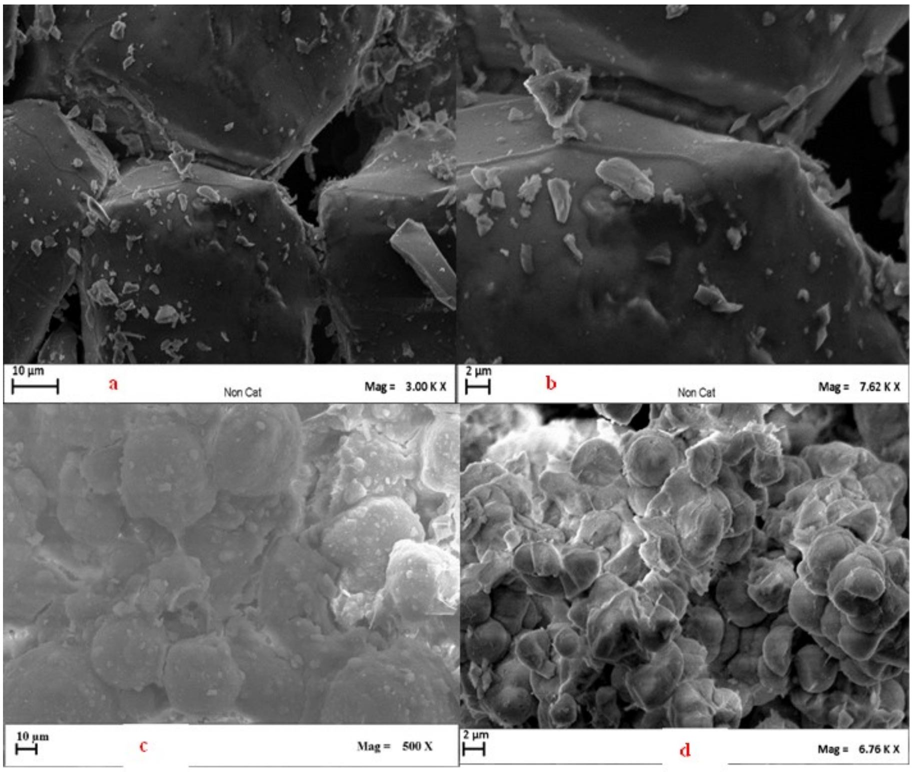

Figure 29: *SEM images at various magnitudes for the bare SiC monoliths (a and b) and for the NiWSiC1 monolith (c and d).*

The images highlighted the inner porosities (a) of the bare monolith, as well as the SiO_2 streaks formed after its calcination at 1000°C (b), the active species and washcoat deposited on the SiC granules (c) and a magnification of the catalysts aggregates (d). In addition, the decrease of the average diameter of the inner porosities is evident from (d), as also reported in **Table *9***.

The distribution of elements on a NiWSiC sample, obtained by EDS element mapping, is shown Figure 30.

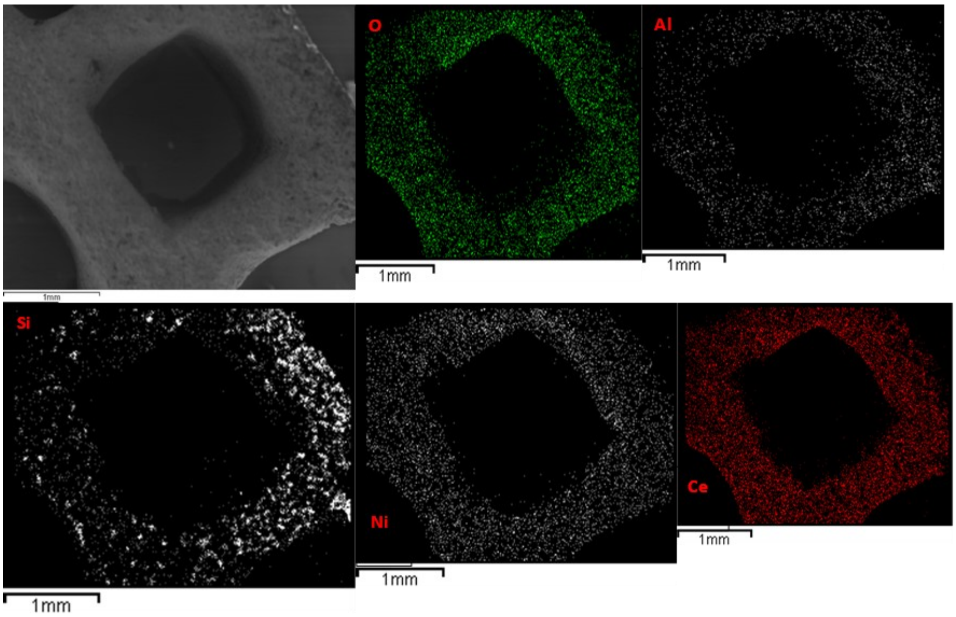

Figure 30: *SEM image and distribution of elements, as obtained by EDS element mapping, for a NiWSiC1 monolith.*

Figure 30 highlights how the active species (Ni) and the washcoat (Ce and Al) cover all the SiC granules, evidencing the very good and homogeneous dispersion obtained with the preparation procedure.

The ultrasound adherence tests, consisting of evaluating the weight loss caused by an ultrasonic cleaning, aimed to investigate the resistance of the coating to a strong mechanical stress. The weight loss percentage vs cycle number is reported in Figure 31 for a single sample after the washcoat deposition.

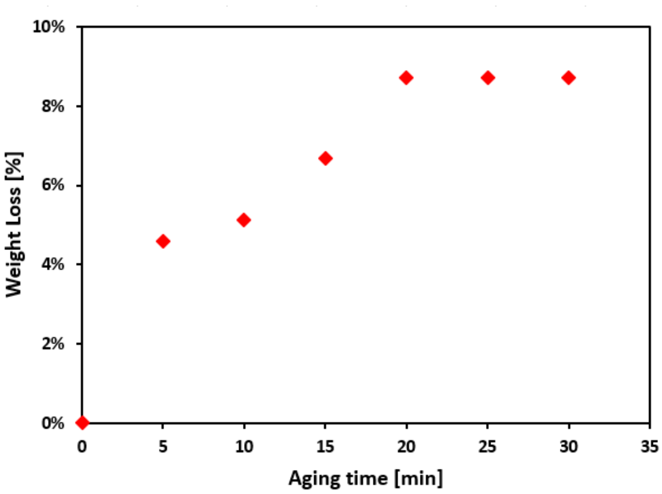

Figure 31: *Weight loss percentage of the prepared washcoated sample.*

As highlighted in Figure 31, a weight loss of about 4,5% was recorded after the first test cycle, and a stable value (about 9%) was reached at the fourth cycle of the test. After that, no more weight losses were registered, and the low final value is evidence of the strong bonding of the washcoat to the carrier surface.

6.2 Results of MW-assisted tests by using the first plant configuration

Preliminary microwave-assisted heating tests were performed, in order to verify the feasibility to heat the monoliths up to the reaction temperature. The results of the tests, performed at various flow rates by feeding N_2 at the fixed power supplied by the microwave generator of 600 W, are shown in Figure 32 for the sample NiWSiC1 as an example.

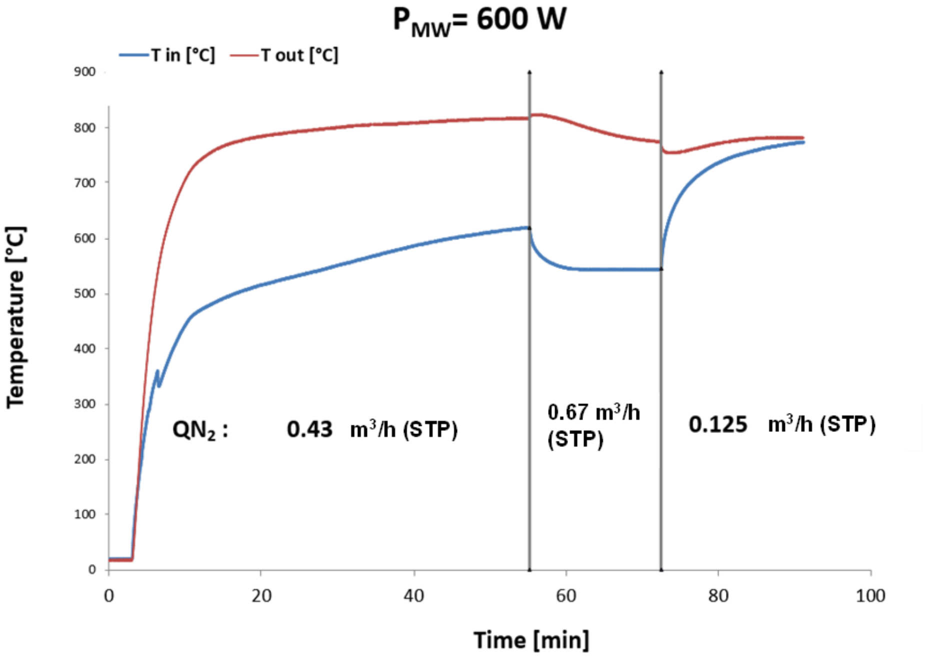

Figure 32: *preliminary microwave-assisted heating test of the catalytic monolith NiWSiC1.*

The data reported in Figure 32 highlight how it is possible to heat the catalytic monoliths using the microwaves by feeding a N_2 gas flow rate similar to that adopted in the reaction tests (0.44 and 0.67 m^3/h STP). The results have shown that in about 10 minutes, it is possible to reach the outlet temperature of about 700°C. Furthermore, it is possible to observe how the flow rate has a significant effect on the thermal behaviour of the system: since the gas is supplied at room temperature and the microwaves heat the solid directly, the higher the flow rate is, the higher its quenching effect is.

Regarding the MW-assisted MSR catalytic tests, the heating phase for both the catalysts is shown in Figure 33, in which the outlet temperature vs time is reported.

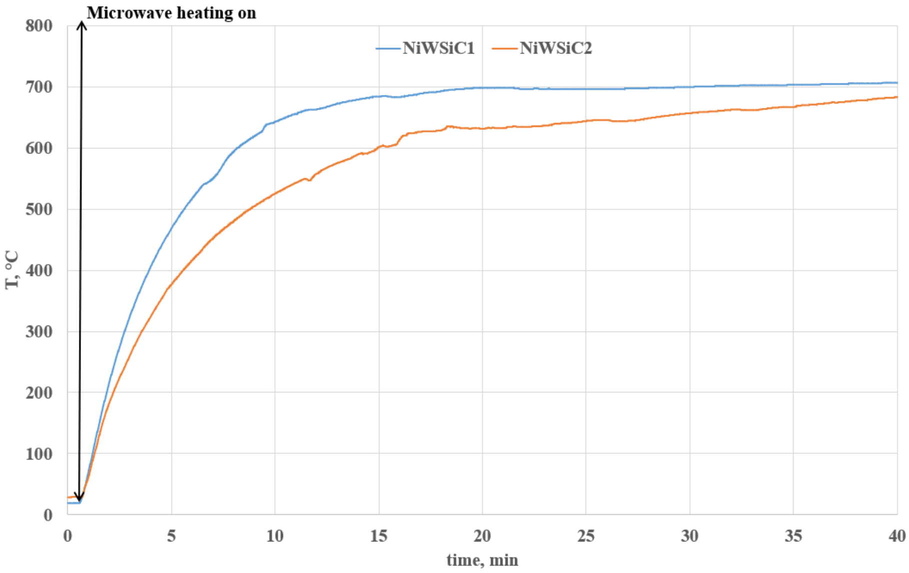

Figure 33: *microwave-assisted catalytic test, detail of the heating phase.*

It is evident how the catalytic monoliths reach the reaction temperature in about 15 min.

The results of the microwave-assisted catalytic tests performed at a GHSV value of 3300 h^{-1} are shown in Figure 34, in terms of CH_4 conversion vs temperature and H_2 yield vs temperature.

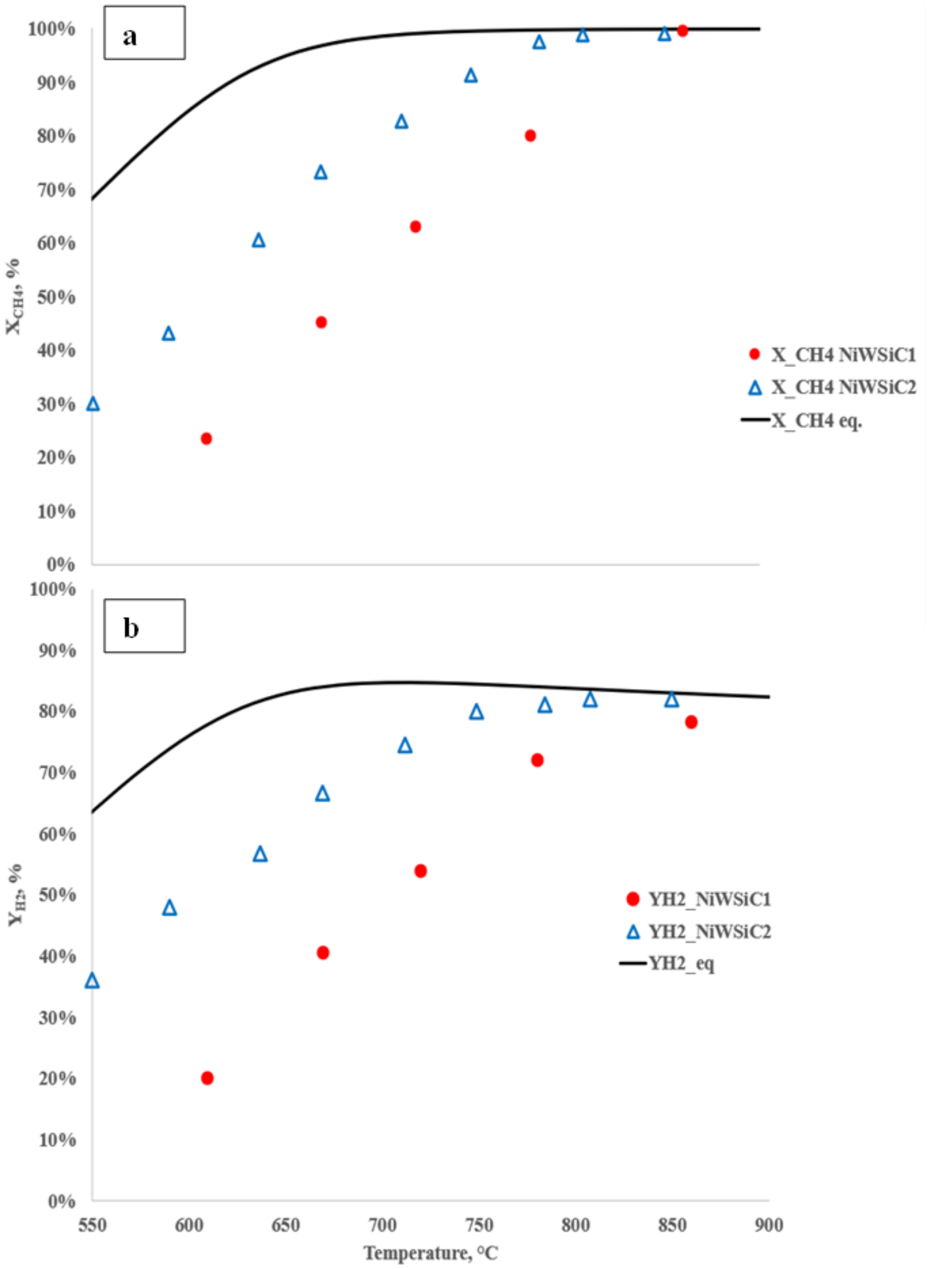

Figure 34: *results of the microwave-assisted catalytic activity tests (GHSV = 3300* h^{-1}*) in terms of a)* CH_4 *conversion and b)* H_2 *yield vs temperature*

The results shown in Figure 34 highlight the better performance of the catalyst NiWSiC2 (higher Ni loading) with respect to the catalyst NiWSiC1 (lower Ni loading) in terms of both CH_4 conversion and H_2 yield. It is evident that the first catalyst approaches the CH_4 conversion thermodynamic equilibrium at about 780°C, showing, in whatever case, a CH_4 conversion higher than 80% for temperature higher than 700°C. The second catalyst have shown a significantly lower CH_4 conversion up to 850°C, and only at about 880°C approached the thermodynamic equilibrium. This behaviour is due to the higher Ni loading of the catalyst NiWSiC2, that increased its catalytic activity towards CH_4 conversion in methane steam reforming. The results relevant to the H_2 yield confirmed the better performance of the catalyst NiWSiC2, that approached the equilibrium H_2 yield at about 800°C; on the contrary, the catalyst NiWSiC1 have shown a lower H_2 yield (about 80%) and never approached the equilibrium H_2 yield in the investigated temperature range.

The tests were performed by adjusting the microwave power supplied in order to reach, in every point shown above, the desired temperature. Similar tests were performed at GHSV = 5000 h^{-1}, in order to investigate the effect of this parameter on the catalytic activity. The comparison of the catalytic activity at the two different values of GHSV are shown in Figure 35, in terms of CH_4 conversion vs temperature for both the catalysts.

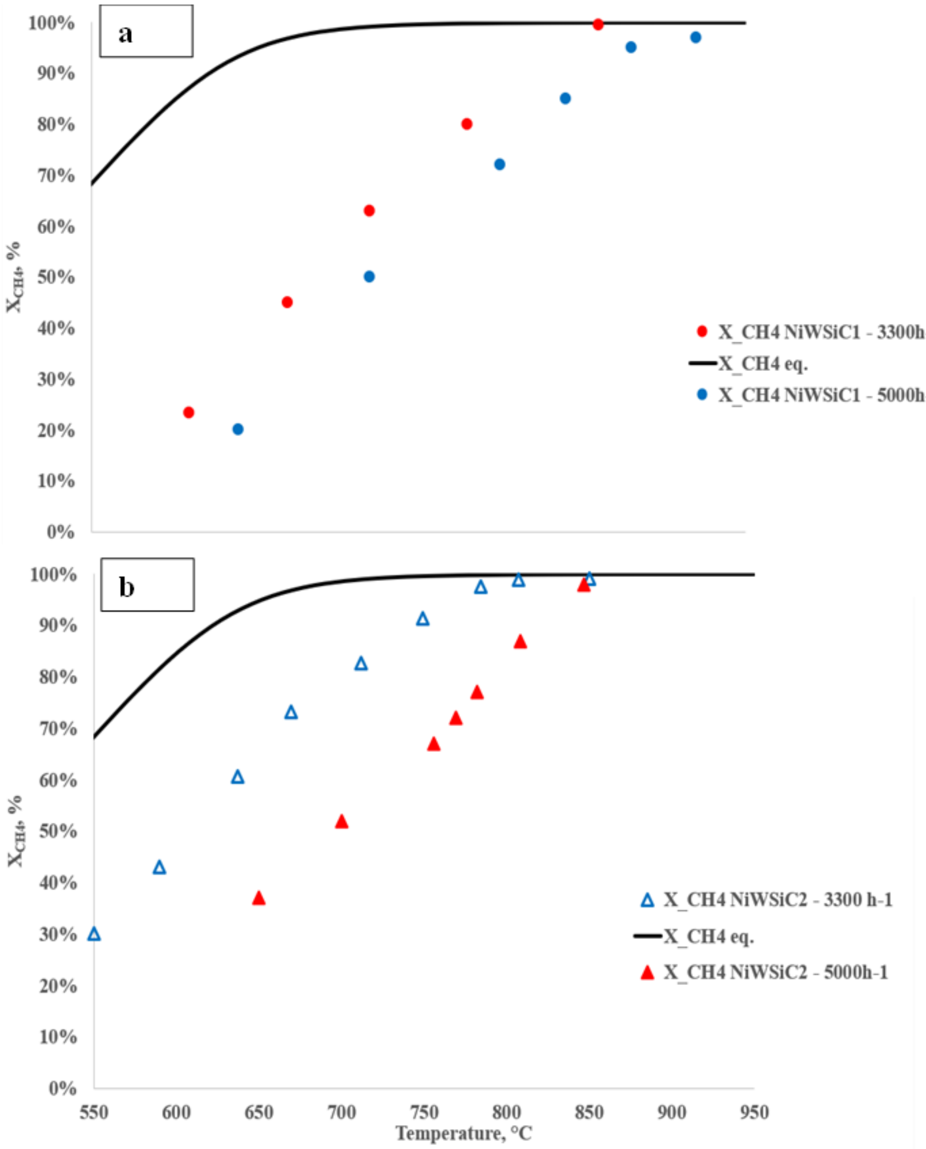

Figure 35: *effect of GHSV on the microwave-assisted catalytic activity tests for: a) catalyst NiWSiC1 in terms of CH_4 conversion vs temperature, b) catalyst NiWSiC2 in terms of CH_4 conversion vs temperature.*

The results in Figure 35 highlight how the catalytic activity in terms of CH_4 conversion decreased by increasing the GHSV, even if an important difference between them can be observed. While in the case of the catalyst

NiWSiC1 the CH_4 conversion did not approach the equilibrium conversion even at about 920°C, the catalyst NiWSiC2 approached the CH_4 equilibrium conversion at about 850 °C (with a difference of about 50°C with respect to the lower GHSV).

By resolving (Equation *24*, it is simple to calculate the value of $Q_{MW} - Q_{diss}$, that corresponds to the heat effectively absorbed by the system. The energy efficiency can now be calculated as the ratio between this last value and the heat supplied by microwaves.

The calculated energy efficiencies were of about 50% and 55%, at GHSV values of 3300 and 5000 h^{-1}, respectively, for both the catalytic systems. This same average value is due to the peculiarity of the microwave heating, that is dependent only on the dielectric properties of the material (in this case the catalysts differ only by Ni loading). A more detailed analysis of the above reported data highlighted that the smaller monolithic catalyst at lower power has a lower efficiency, since up to 700W, corresponding to about 800°C, the dissipative effects overcome the material microwaves absorption, affecting the thermal management of the system.

A first value of energy consumption of the microwave-assisted steam reforming performed by using the first plant configuration may be calculated as kWh/(produced Nm^3H_2). The final value is **3.8** kWh/(produced Nm^3H_2). It is evident that, nevertheless the developed microwave-assisted system for the steam reforming needs further improvements in terms of wave guide and reactor optimization, in order to increase the energy efficiency, its energy consumption is comparable (and in some cases lower) to that of the electrolysers (**Table *10***).

Table 10: *energy consumption among the microwave-assisted steam reforming and different kinds of electrolysers for* H_2 *production.*

Technology	**Conventional alcaline electrolyser [61]**	**Advanced Alcaline electrolyser [61]**	**Proton exchange electrolyser [61]**	**High temperature electrolyser [61]**	**MW-assisted Steam Reforming (this Ph.D. thesis)**
Energy consumption (kWh/Nm^3H_2)	4.3-4.9	3.8-4.3	4.2-5	3.5	**3.8**

6.3 Results of CFD modelling of the second reactor configuration

The very promising results above reported, led to focus the attention on the reactor and plant optimization, as described in Chapter 4. Once designed the new reactor configuration, the first efforts were devoted to its CFD modelling, and a selection of the best results is below reported.

6.3.1 CFD modelling results

The first modelling result reported is the electromagnetic field distribution after 600 s of MW heating (Figure 36).

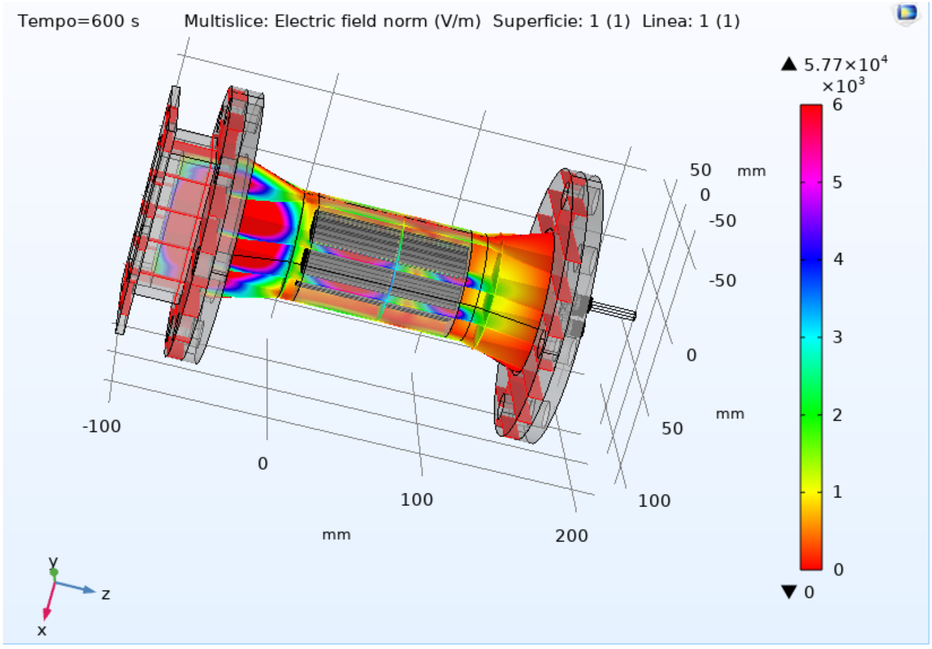

Figure 36: *Electromagnetic field in the whole reactor expressed in V/m. Microwave generator is on the left.*

The first image (Figure 36) proposed is the electromagnetic field distribution, expressed in V/m, of the inner domain within the waveguide. The representation of the result has been proposed in 3D view; as mentioned above, the system has been set up so as to have on the main surface the entrance "port" of the microwaves that will then travel along the entire waveguide. This section is the area with the highest field intensity, and therefore, considering the chosen colour scale, the one with the reddest colour. Continuing along z, it is possible to notice how the intensity is always decreasing in favour of a colour closer to blue (lower field intensity) exactly near the domain of the SiC monolith used and loaded in the centre of the waveguide itself. This behaviour of the field is clearly due to the permittivity value, part real and part imaginary, of the SiC, which from data acquired from the literature has been dictated as (9 + 14.5j). This value is synonymous with a microwave-absorbing body and therefore, in agreement with the hypothesis, explains the weakening of the field strength along the propagation axis.

The second image is the representation of the temperature and the flow field distributions inside the overall system after 300s of MW heating (Figure 37).

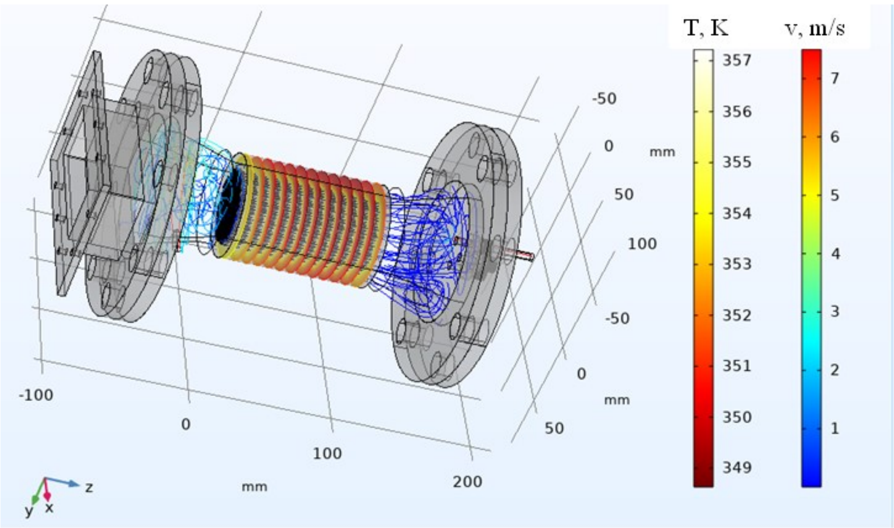

Figure 37: *temperature and velocity field distribution inside the overall system.*

From Figure 37, it is evident that the monolith is effectively able to heat by means of microwaves irradiation, and that in about 5 minutes it reaches the temperature of about 360 K. Moreover, the velocity field simulation have shown how the gas enters in all the monolith channels, without any by-pass phenomena. The simulation tool is also able to model the heating phase of the monolith. In Figure 38 the diagram reporting the temperature distribution along the monolith length is reported at increasing times (up to 600 s) of MW irradiation.

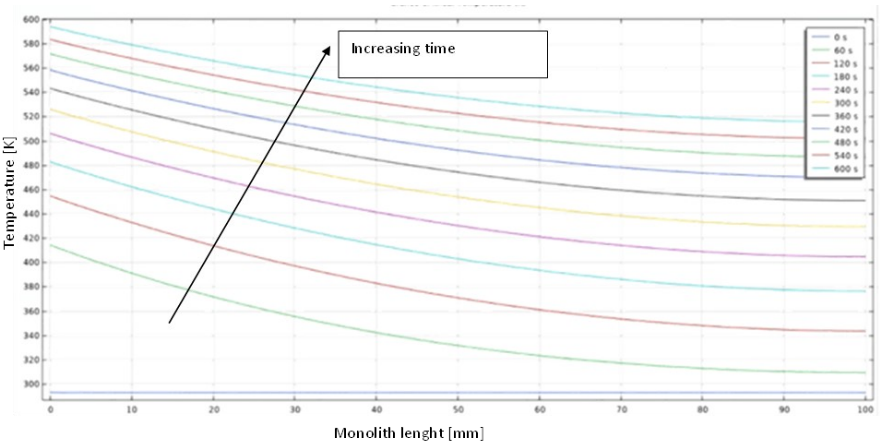

Figure 38: *temperature distribution along the SiC monolith during the microwave- assisted heating phase: the curves are parametric in the time.*

6.3.2 Validation of the CFD modelling

The simulation results have been validated with properly designed experimental tests, as described in chapters 4 and 5, aiming at mapping the temperature of the SiC monolith when it is exposed to microwaves, in which:

- A SiC monolith with the same dimensions of the catalytic one was used;
- Inert gas with the same flow rate of the simulations have been used;
- The same MW power considered in the simulations was used;

As an example of the results obtained in the mapping of the radial profile at different axial positions, the data relevant to an Ar flow rate of 2 NL/min are reported.

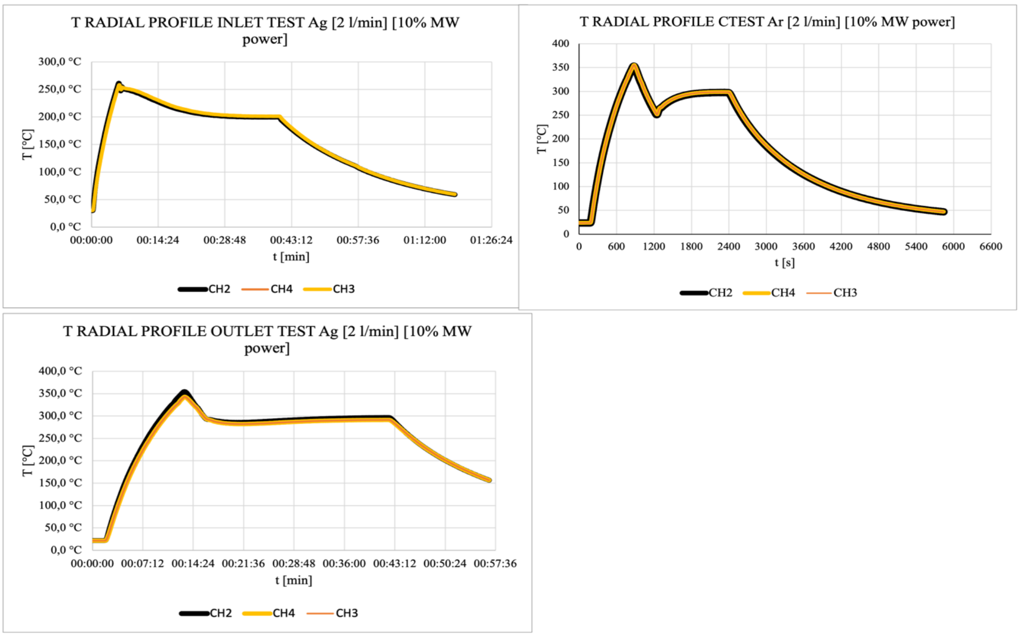

Figure 39: *Experimental results of T radial profile inside the SiC monolith. Ar flow rate 2 NL/min.*

Each MW-assisted experimental test may be divided into three zones: (i) heating (left side of the figure, with the curves having an increasing trend), (ii) stationary with T fixed at 300 °C (middle part of the figure, with the curve reaching a plateau), and (iii) cooling (right side of the figure, with the curves having a decreasing trend).

As evident, no temperature radial profile is present, since the very good thermal conductivity of silicon carbide allows an almost homogeneous heat distribution, making the radial T profile practically flat during all the phases of the MW-assisted experimental tests.

Aiming at determining the axial temperature profile, the sensors were located at the entrance (CH2) in the middle (CH3) and at the outlet (CH4) of the monolith. In Figure 40 the results of an experimental test are reported, in which the temperature is first increased with a ramp by fixing the setpoint of a temperature controller to 350°C, and then it is maintained fixed to 300°C.

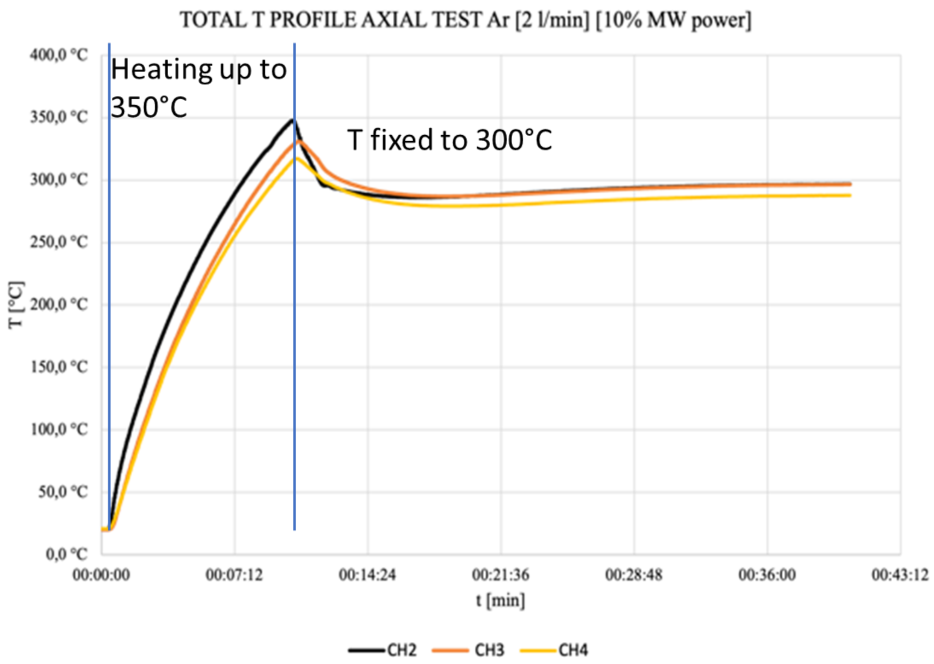

Figure 40: *Experimental results of T radial profile inside the SiC monolith. Ar flow rate 2 NL/min.*

The results have shown that an axial gradient is present during the MW-assisted heating phase, since from the outlet to the inlet a T difference of about 35°C was measured, but that during the isotherm phase this gradient practically disappears and all the monolith has the same temperature, as shown by the CFD simulations (Figure 37).

The comparison of the modelling and experimental results is shown in Figure 41. The different curves represent the temperature distribution along the monolith in the axial direction at different times (up to 600 s) of MW irradiation obtained through the CFD simulations. The dotted points represent the results of the experimental tests, with CH2, CH3 and CH4 being the fibres located in the inlet, middle and outlet section, respectively.

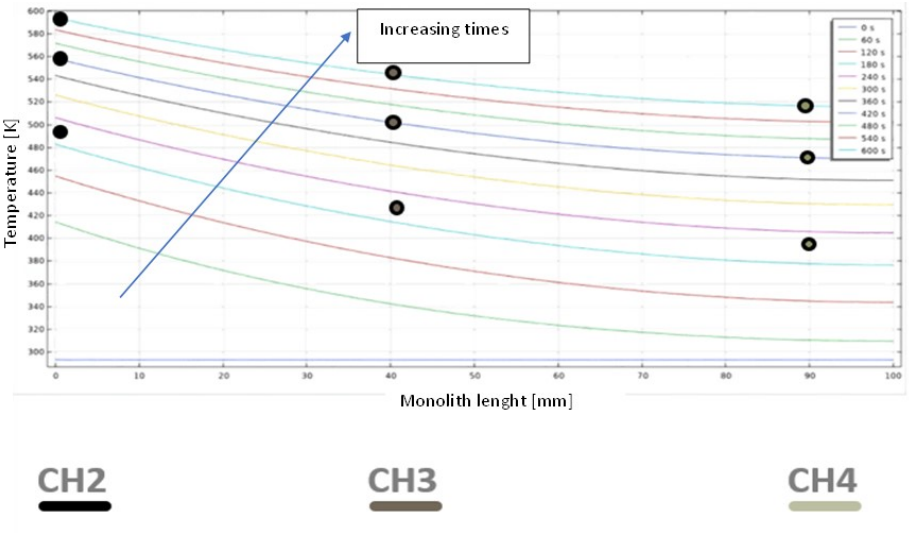

Figure 41: *comparison of the modelling (curves) and experimental (dotted points) results.*

The results reported in Figure 41 evidenced that the developed model is able to fit the experimental data: in fact, it is evident that the experimental results (the dotted points) are very close to the modelling results (the curves) in the different time intervals. For clarity reasons, these results are summarised in the following table.

Table 11: *comparison between modelling and experimental results in terms of temperature of the SiC monolith.*

Time [s]	Temperature fibre	Experimental value [K]	Modelling value [K]
240	CH2	490	505
	CH3	435	450
	CH4	415	420
480	CH2	560	560
	CH3	510	510
	CH4	490	490
600	CH2	600	600
	CH3	560	560
	CH4	535	535

6.4 Results of the MW-assisted catalytic activity tests by using the second plant configuration

Preliminary microwave-assisted heating tests were performed, in order to verify the feasibility to heat the monoliths up to the reaction temperature in the two systems. The results of the tests, performed at various flow rates by feeding N_2 at the fixed power supplied by the microwave generator of 600W and 400 W in the classical (PMW1) and optimized (PMW2) reactor respectively, are shown in Figure 42, in terms of Tout vs time.

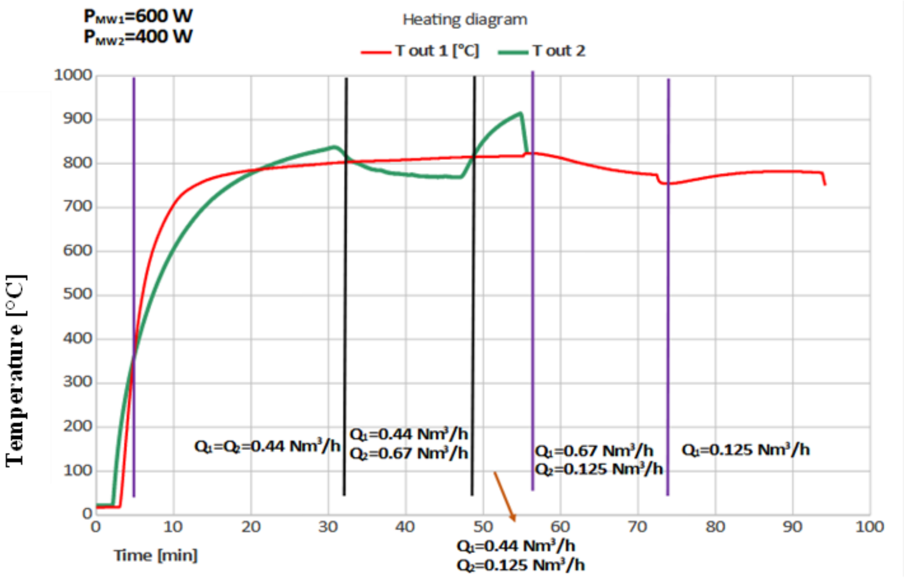

Figure 42: *Preliminary microwave-assisted heating test of the catalytic monolith NiWSiC1, obtained with two different reactor configurations.*

The above reported data evidenced the beneficial effect of the new reactor configuration. In fact, the same monolith can be heated up to the reaction temperature (about 800 °C) with a lower MW power in all the investigated flow rate values. In this way, a potential huge energy saving may be possible.

The catalytic activity tests were performed under the operating conditions reported in **Table** *7*. In particular, the MW-assisted MSR catalytic activity tests have been performed by using the lowest loaded structured catalyst (NIWSiC1) and by choosing the higher value of GHSV (5000 h^{-1}). This value has been set in order to perform the tests in the worst operating conditions for the catalyst (the higher the GHSV is, the lower the contact time is): in this way, the role of the optimized reactor configuration was clearer. Moreover, the higher the flow rate is, the higher the H_2 production is: in this way an hypothetical energy saving may be more effectively demonstrated.

The results of the microwave-assisted catalytic tests are shown in Figure 43 and Figure 44, in terms of CH_4 conversion vs temperature and H_2 yield vs temperature, respectively.

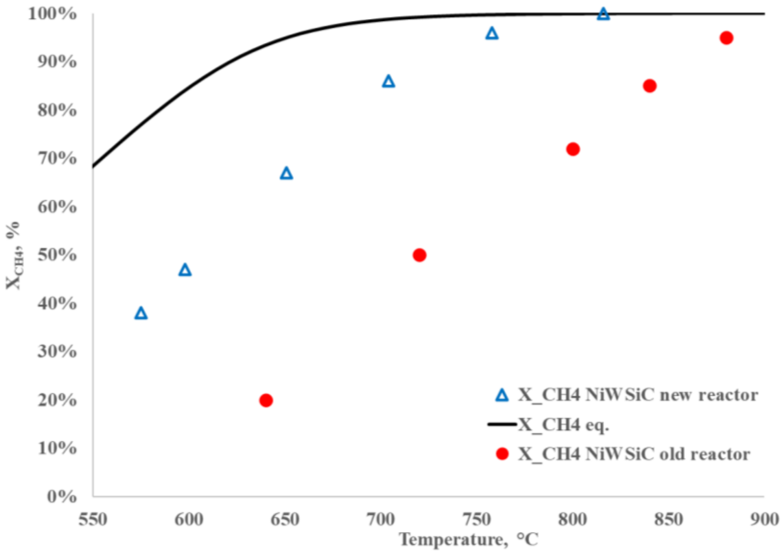

Figure 43: *Results of the microwave-assisted catalytic activity tests (GHSV = 5000* h^{-1}*) in terms of* CH_4 *conversion vs temperature for the NiWSiC1 catalyst in two reactor configurations.*

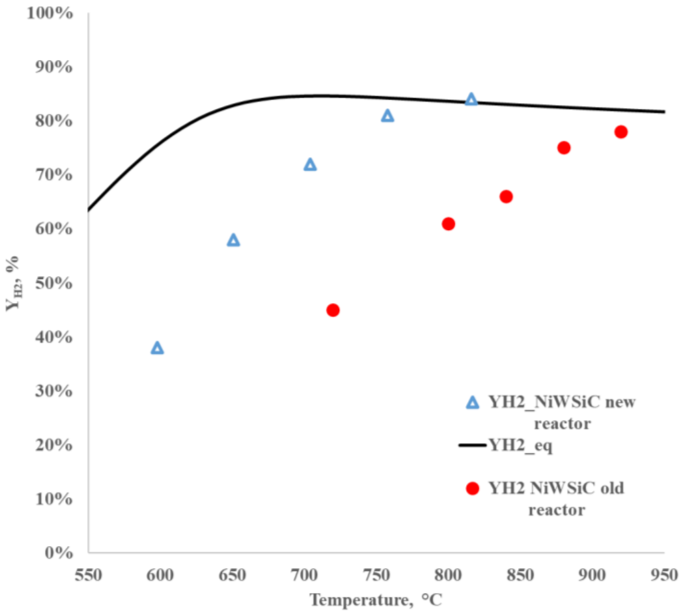

Figure 44: *Results of the microwave-assisted catalytic activity tests (GHSV = 5000 h^{-1}) in terms of H_2 yield vs temperature for the NiWSiC1 catalyst in two reactor configurations.*

The results shown in Figure 43 and Figure 44 highlight how the optimized reactor configuration positively influences the system performance. In fact, the intensified and more uniform microwave field in the reactor assured a better thermal management, which resulted in a more uniform temperature profile: in this way, higher both CH_4 conversion and H_2 yield may be obtained. In fact, with the new reactor configuration, the catalyst approaches the CH_4 conversion thermodynamic equilibrium at about 750°C, showing, in whatever case, a CH_4 conversion higher than 80% for temperature higher than 700°C.

The same catalyst has shown a significantly lower both CH_4 conversion and H_2 yield in the tests performed in the old reactor configuration. In particular, this catalyst was not able to approach the thermodynamic equilibrium values in all the investigated temperature range.

The microwave power supplied in the two tests is shown in Figure 45. The reported data highlight how the new reactor configuration resulted in a lower MW power needed for reaching the same temperature. In fact, for example, 500W and 800W are needed for having the temperature of 800°C for the new and old reactor configuration, respectively.

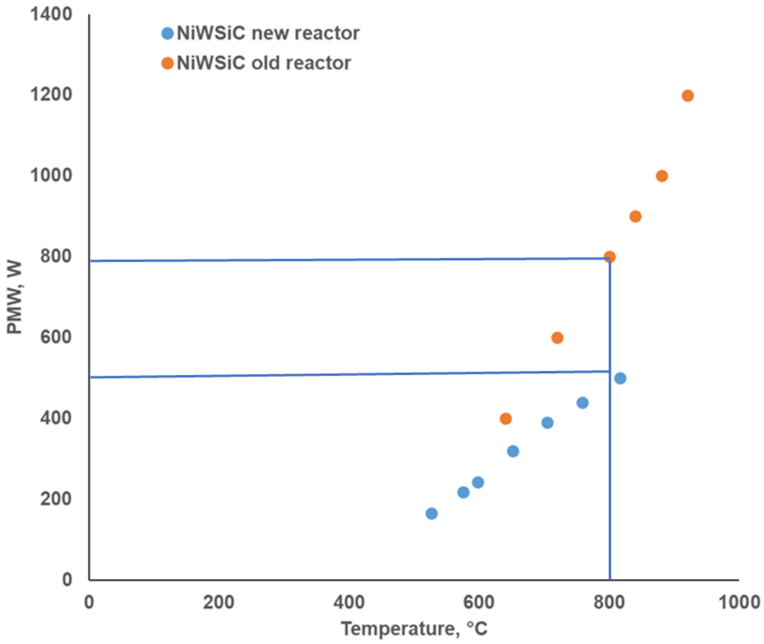

Figure 45: *Microwave power (PMW) vs temperature during the catalytic activity tests performed in the old and new reactor configuration, 5000 h*$^{-1}$.

The comparison of the two reactor configurations can give additional information regarding the advantages of the new configuration.

Once calculated through (*Equation 24* the value of $Q_{MW} - Q_{diss}$, corresponding to the heat effectively absorbed by the system, the energy efficiency can now be obtained as the ratio between this last value and the heat supplied by microwaves. The average energy efficiency for the two reactor configurations is shown in Figure 46.

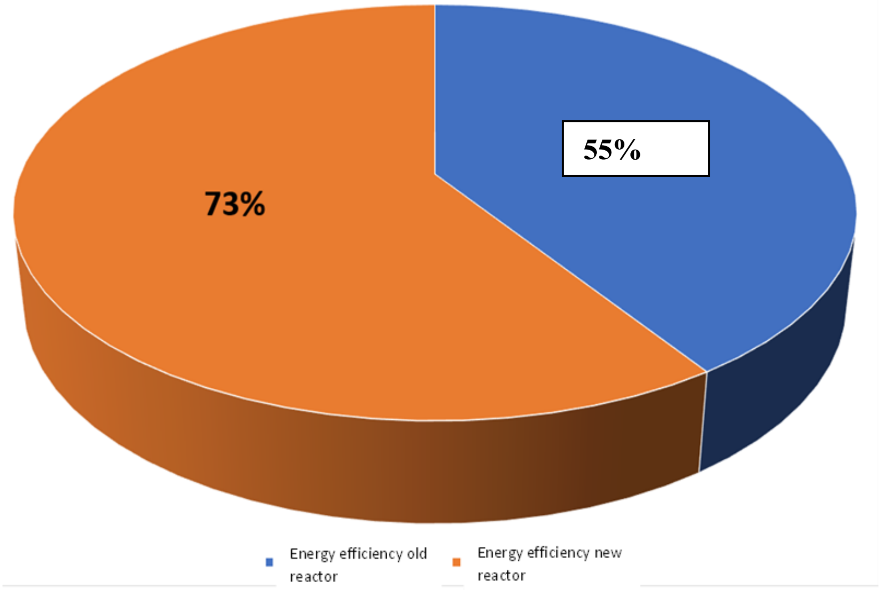

Figure 46: *energy efficiency for the MW-assisted steam reforming by using the new and the old reactor configuration.*

The data reported in Figure 46 highlight how the optimization of the reactor configuration allowed to obtain an energy efficiency of about 73%, at GHSV value of 5000 h^{-1}. This very good value confirms the importance of the reactor in a MW-assisted process. In this sense, it is noteworthy to underline that the waveguide has a far-from-negligible influence on the transport of electromagnetic waves and, consequently, has a great influence on the distribution of the field itself. It is therefore possible to exploit the geometry of the cavity and that of the waveguide to maximize the power that is transferred to the load to be heated. In fact, modifications of the cavity shape may influence the electric field. It is interesting to note that in the shape without curvatures (old reactor), the sinusoidal distribution of the electric field guarantees a certain constancy in the distribution of high intensity and low intensity zones along the propagation axis. The new reactor configuration, characterized by the presence of a restriction in the catalytic zone, allowed the modification of the propagation of the electric field with respect to a classical reactor. In fact, the bottleneck generates a central zone of high intensity of electric field rather constant in a relatively large length, which allows to ensure a certain focusing of the heating in that area. Therefore, the reactor walls may convey the waves to the catalytic zones by creating constructive interferences, resulting in an intensification of the resultant field, and in a consequent more effective employment of the catalyst. In fact, the catalyst with the lower Ni loading was able to obtain the same catalytic performance of the higher loaded catalyst with the old reactor configuration (Figure 34).

6.4.1 Evaluation of the kinetic parameters

The kinetic parameters, namely pre-exponential factor and activation energy, for the developed model are reported in Table 12.

Table 12: *Kinetic parameters for the structured catalyst.*

	k_0	Ea ($\frac{kJ}{mol}$)
Steam reforming	5585 mol/g·min·atm^2	57
Water gas shift	1065 mol/g·min	30

The model fitting of the experimental data is shown in Figure 47 for the GHSV value of 3300 h^{-1}, where the product stream composition experimentally evaluated through the mass spectrometer analysis is compared to the composition resulting from the developed model.

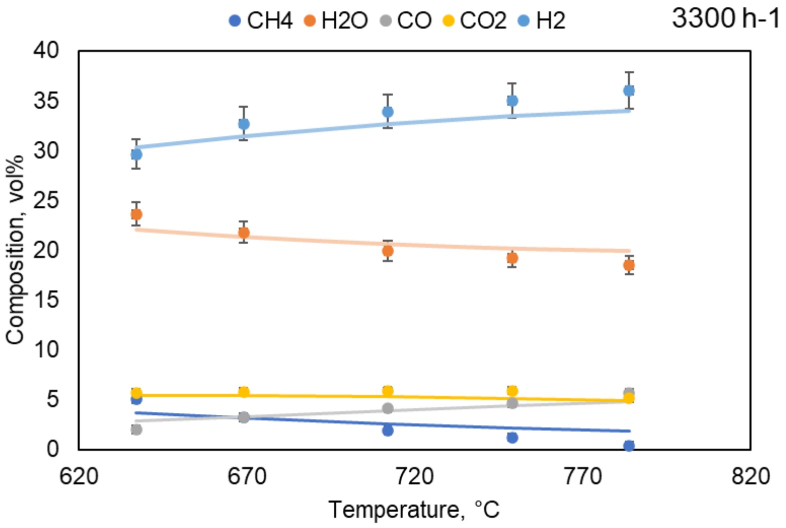

Figure 47: *Comparison of the experimental and kinetic model results for the structured catalyst NiWSiC1, GHSV = 3300* h^{-1}.

The above reported data have shown a good agreement between the modelled and the experimental values in the investigated temperature range, thus proving the feasibility of the developed kinetic model. In particular, the model is able to describe the above-discussed good extent of WGS reaction in presence of this structured catalyst. The calculated activation energy for the steam reforming reaction (about 57 kJ/mol) is lower than that reported in literature for the Ni-based commercial catalysts (about 96 kJ/mol) [156], so confirming the good performance of the prepared catalyst.

6.5 Comparisons

The performance of the MW-assisted reforming process presented in this work have been compared with the literature in terms of both catalytic performance and energy consumption. The former is reported in Table 13 with other structured catalysts tested in steam methane reforming reaction; the latter is reported in Table 14 with other MW-assisted and resistive heated reforming processes.

Table 13: *comparison of different Ni-based structured catalysts performance in MSR [157].*

Structured catalysts	**Operating Conditions**	**Catalytic performance**	**Reference**
Ni/Ce honeycomb	T = 450 - 650°C S/C = 2 P = 1 atm	X_{CH4} = 79.1 % T = 650 °C	[108]
Ni_3Al Rolled foils	T = 600 - 800 °C S/C = 1 GHSV = $0.091 m^3/(hm^2)$	X_{CH4} = 90 % @ 650 °C	[112]
Ni Rolled foils	GHSV = 455 - 2880 h^{-1} S/C = 0.62 - 2.48 T= 700 - 800 °C	X_{CH4} = 94.0 % H_2 yield = 77.6 % @ T = 800 °C, GHSV = 535 h^{-1}, S/C = 1.24	[115]
Ni Rolled foils	GHSV = 6400 h^{-1} S/C=1.362 T= 600 - 900 °C	X_{CH4} = 55.7 % @ T = 800 °C	[116]

Ni Rolled foils	GHSV = 6400 h^{-1} S/C = 1.362 T= 600 - 900 °C	X_{CH4} = 90 % @ T = 900 °C	[117]
10 %Ni/10 %MgO/Ni-foam Membrane reformer with Ni foam	P = 1-bar T = 400 - 600 °C S/C = 2	Equilibrium CH_4 conversion values @ 600 °C for the catalytic discs	[120]
10 %Ni calcium aluminate modified SiC	GHSV = 30000 h^{-1} T = 650 - 850 °C P = 1-bar S/C = 1 to 3	X_{CH4} = 97.9 % at T = 650 °C and S/C = 3 X_{CH4} = 81.3 % at T = 850 °C and S/C = 1	[125]
15%Ni/CeO_2-Al_2O_3 On a SiC monolith	GHSV = 3300 and 5000 h^{-1} T = 550 – 950 °C P = 1 bar S/C = 3	CH_4 equilibrium conversion T = 800 °C – GHSV = 3300 h^{-1} T = 850 °C – GHSV = 5000 h^{-1}	**This Ph.D. thesis**
7%Ni/CeO_2-Al_2O_3 **On a SiC monolith**	**GHSV = 5000 h^{-1}** **T = 550 – 800 °C** **P = 1 bar** **S/C = 3**	**CH_4 equilibrium conversion** **T = 750 °C – GHSV = 5000 h^{-1}**	**This Ph.D. thesis**

Table 14: *comparison of different Ni-based catalysts performance in electrified reforming processes [157].*

MW-ASSISTED REFORMING PROCESSES						
Process	**Catalyst**	**MW input**	**Operating Conditions**	**X_{CH4}; X_{CO2}**	**Energy Consumption kWh $Nm^{-3}H_2$**	**Reference**
MDR	10Ni/AC	-	CO_2/CH_4=1 WHSV = 33 L h^{-1} g^{-1} T = 650°C	X_{CH4}= 48% X_{CO2}= 51%	-	[135]
MDR	Ni/MgO/AC	-	CO_2/CH_4=1 WHSV = 33 L h^{-1} g^{-1} T = 650°C	X_{CH4}= 82% X_{CO2}= 85%	-	[135]
MDR	7Ru/$SrTiO_3$	P =	CO_2/CH_4=1	X_{CH4}=	18.58	[137]

		36.99 kW	T=940 °C.	99.5% X_{CO2}= 94%		
MDR	Ni/Al_2O_3	P= 45 - 60 W	CO_2/CH_4=1 T=800 °C. WHSV = 11,000 mL g^{-1} h^{-1}	X_{CH4}= 90% X_{CO2}= 90%	-	[139]
MDR	Pt/C	P= 45 - 60 W	CO_2/CH_4=1 T=800 °C. WHSV = 11,000 mL g^{-1} h^{-1}	X_{CH4}= 90% X_{CO2}= 90%	-	[139]
MDR	Ni/Al_2O_3-SiC	P= 45 - 60 W	CO_2/CH_4=1 T=800 °C. WHSV = 11,000 mL g^{-1} h^{-1}	X_{CH4}= 90% X_{CO2}= 90%	-	[139]
MDR	Ni/SiC	P= 45 - 60 W	CO_2/CH_4=1 T=800 °C. WHSV = 11,000 mL g^{-1} h^{-1}	X_{CH4}= 90% X_{CO2}= 90%	-	[139]
MDR	Fe/HZSM-5	P = 700 W	CO_2/CH_4=1 WHSV = 2.4 L h^{-1} g^{-1}	X_{CH4}= 63.03% X_{CO2}= 91.27%	-	[158]
MDR	$La_xSr_{2-x}CoO_{4-}$Mn	P = 140 W	CO_2/CH_4=1 WHSV = 10 L h^{-1} g^{-1}	X_{CH4}= 80% X_{CO2}= 80%	3.98	[159]
MDR	Co−Mo/TiO_2	P = 100 W	CO_2/CH_4=1 WHSV = 10 L h^{-1} g^{-1}	X_{CH4}= 81% X_{CO2}= 86%	-	[160]
MDR	Cu−Mo/TiO_2	P = 100 W	CO_2/CH_4=1 WHSV = 10 L h^{-1} g^{-1}	X_{CH4}= 76% X_{CO2}= 62%	-	[160]
MDR	Ni-Co/ZrO_2-CaO + SiC	-	CO_2/CH_4=1 WHSV = 10 L h^{-1} g^{-1} T = 800°C	X_{CH4}= 97.1% X_{CO2}= 99.2%	-	[161]

MSR	**15%Ni/CeO_2-Al_2O_3 on a SiC monolith**	**P = 800 W @ GHSV = 3300 h^{-1}** **P = 1000 W @ GHSV = 5000 h^{-1}**	**GHSV = 3300 and 5000 h^{-1}** **T = 550 – 950 °C** **P = 1 bar** **S/C = 3**	**CH_4 equilibrium conversion** **T = 800 °C – GHSV = 3300 h^{-1}** **T = 850 °C – GHSV = 5000 h^{-1}**	**3.8**	**This Ph.D. thesis**
MSR	**7%Ni/CeO_2-Al_2O_3 on a SiC monolith**	**P = 400 W**	**GHSV = 5000 h^{-1}** **T = 550 – 800 °C** **P = 1 bar** **S/C = 3**	**CH_4 equilibrium conversion @ T = 750 °C**	**2.5**	**This Ph.D. thesis**
			Resistive (Joule) heated reforming processes			
MDR	SiC heating element/ Ni/Al_2O_3	P= 218 W	CO_2/CH_4=1 T=790 °C.	X_{CH4}= 85%	5.1	[162]
MSR	SiC heating element/ Ni/Al_2O_3	P= 220 W	CH_4/H_2O=3 T=790 °C.	X_{CH4}= 80%	4.8	[162]
MDR	Stainless electrode/ Ni/La-ZrO_2	I= 12 mA V= 0.4 kV P = 5 W	T=576 K CH_4/CO_2=1	X_{CH4}= 30.2 %	18	[163]
MSR	Stainless electrode rode/ Ni/$CeZrO_2$ Ce/Zr=3	I= 3 mA EPC = 1.29 W	T=190 °C H_2O/CH_4=2	X_{CH4}= 12 %	3.98	[164]
MSR	Stainless electrode rode/ Ni/$CeZrO_2$ Ce/Zr=1	I= 3 mA EPC = 1.53 W			3.21	[164]
MSR	Stainless electrode rode/	I= 3 mA EPC =			3.75	[164]

		2.54 W				
MSR	Rh/Al_2O_3 washcoated SiSiC foam	P = 394.6 W	T = 650°C S/C = 4.1/1 GHSV=150000 $cm^3\ h^{-1}\ g_{cat}^{-1}$		2	[165]

The data reported in Table 14 highlight the good performance of the system also in terms of energy consumption, if compared with some other electrified reforming processes available in literature. In particular, it is very important to note that, besides the intrinsic energy efficiency of the magnetron (about 50-60%), the developed MW-assisted high efficiency catalytic reactor is able to allow an energy consumption (2.5 kWh/Nm^3H_2) very close to the one of the best resistive MSR (2 kWh/Nm^3H_2). This result is noteworthy since the latter process is not affected by any intrinsic energy losses (the catalyst is directly heated through Joule effect, without any other devices for energy generation).

One more comparison is possible also with the electrolysers employed for H_2 production. This comparison in terms of energy consumption expressed in kW/Nm^3H_2 is reported in **Table *15***.

Table 15: *energy consumption among the microwave-assisted steam reforming and different kinds of electrolysers for H_2 production.*

Technology	**Conventional alcaline electrolyser [61]**	**Advanced Alcaline electrolyser [61]**	**Proton exchange electrolyser [61]**	**High temperature electrolyser [61]**	**Microwave-assisted Steam Reforming (this Ph.D. thesis)**
Energy consumption (kWh/Nm^3H_2)	4.3-4.9	3.8-4.3	4.2-5	3.5	**2.5**

It is evident that the developed MW-assisted system for the steam reforming, having a high energy efficiency (about 73%), has an energy consumption lower than that of the electrolysers.

A very important benefit of this innovative microwave-assisted reforming process design is the possibility for exceptionally compact reactors. A conventional top-fired reformer producing about 220000 m^3/h (STP) of hydrogen has an overall volume of about 1100 m^3, by considering only the reforming furnace, with an efficiency of about 75%. A comparison between the conventional and microwave-assisted reforming processes can be made in terms of the total volume for H_2 production: with the MW-assisted process a total volume of about 30 L is needed for the production of 50 m^3/h (STP) of H_2, while about 250 L is needed in the case of the conventional plant. The enormous volume saving that could be obtained by changing the heat source is clearly evident, enhancing the thermal management of the system, and consequently removing a substantial portion of the reactor volume. Moreover, the scale-down of the conventional reformer is not feasible for a distributed hydrogen production, and, more importantly, the lower the plant dimension is, the lower the efficiency of the conventional process is. The innovative and compact proposed microwave-assisted steam reforming process can be effectively used for distributed H_2 production.

Chapter 6

Chapter 7

7 Conclusions

In this Ph.D. thesis the feasibility to intensify chemical processes by using MWs will be investigated, and in particular the methane reforming reaction has been chosen as reference case.

The main critical issue of the methane reforming reactions is represented by the enormous thermal duty required for the feed heating and for the reaction endothermicity, so involving a very high temperature heating medium (T>1100°C) as well as special steels for the heat transfer to the catalyst. Nevertheless, the heat transfer process is the rate limiting step, corresponding to very large reactor volume and very slow transient behaviour. In addition, the thermal constrains of this system limit the maximum temperature achievable in the catalytic bed, and consequently the hydrocarbons conversion is usually lower than 85%. This complexity results in high fixed and operative costs, and, in turn, in a reduction of the overall process efficiency.

In order to overcome the critical issues of the reforming reactor previously discussed, the application of a structured catalyst susceptible to microwaves aims to realize the direct catalyst microwave heating, removing the rate limiting step of the heat transfer and the related negative drawbacks. The possibility to fast and directly provide the heat inside the catalytic volume allows to realize a simpler reactor design, a dramatic reduction of the reaction volume, shorter start-up times and the use of cheaper materials. In particular, by selecting the catalyst carrier with the right chemical-physical properties, in terms of MW-loss factor and thermal conductivity, a very uniform temperature profile could be achieved, resulting in a more effective and selective exploiting of catalyst surface, minimizing the catalyst mass, making the system more attractive in terms of cost and compactness.

Two MW-susceptible structured catalysts with two different Ni loadings were prepared by first depositing a Ceria/Alumina slurry on SiC monoliths and then by impregnating them in a nickel nitrate solution. The prepared catalysts were tested for the microwave-assisted methane steam reforming reaction, by means of a specifically set-up laboratory plant. The preliminary heating tests have shown the possibility to heat the catalytic monoliths up to the desired reaction temperature. The activity tests, performed at two different GHSV (3300 e 5000 h^{-1}) have shown that the Ni loading influenced the catalyst performance, both in terms of methane conversion and hydrogen yield: the higher the Ni loading is, the better the performance is. The GHSV influenced the catalyst behaviour, since at the higher GHSV the performance decreased, even if the catalyst with the higher Ni loading approached the equilibrium conversion values in all the investigated GHSV conditions. The two catalytic systems have shown an average energy efficiency of 50% and 55%, at the lower and higher GHSV, respectively. The comparison of the energy consumption expressed in kW/Nm^3H_2 of the microwave-assisted steam reforming with different kinds of electrolysers for H_2 production have shown an energy consumption for the MW-assisted process comparable (and in some cases lower) with respect to that of the electrolysers. These results highlighted how an effective and feasible process intensification is possible with this innovative system, in particular for a distributed hydrogen production.

Starting from these very promising results, the role of the reactor configuration in a MW-assisted MSR has been investigated. In particular, a reactor characterized by a restriction in the catalytic zone has been designed and realized, and the performance of a Ni-based catalyst have been compared by using a classical and the optimized configuration. The activity tests, performed at a GHSV of 5000 h^{-1} have shown that the catalyst was able to approach the CH_4 conversion thermodynamic equilibrium values at about 750°C in the optimized configuration. Moreover, the optimization of the reactor configuration allowed to obtain an energy efficiency of about 73%, while a value of 55% was obtained with the classical one. This important difference confirms the importance of the reactor in a MW-assisted process.

In fact, the new reactor configuration, characterized by the presence of a restriction in the catalytic zone, allowed the modification of the propagation of the electric field with respect to a classical reactor. Therefore, the reactor walls may convey the waves to the catalytic zones by creating constructive interferences, resulting in an intensification of the resultant field, and in a consequent more effective employment of the catalyst. In fact, the catalyst with the lower Ni loading was able to obtain the same catalytic performance of the higher loaded catalyst with the old reactor configuration.

The comparison of the energy consumption expressed in kW/Nm^{3}H$_2$ of the microwave-assisted steam reforming with different kinds of electrolysers for H$_2$ production have shown an energy consumption for the MW-assisted process lower with respect to that of the electrolysers. In particular, it is very important to note that, besides the intrinsic energy efficiency of the magnetron (about 50-60%), the developed MW-assisted high efficiency catalytic reactor is able to allow an energy consumption (2.5 kWh/Nm^{3}H$_2$) very close to the one of the best resistive MSR (2 kWh/Nm^{3}H$_2$). This result is noteworthy since the latter process is not affected by any intrinsic energy losses (the catalyst is directly heated through Joule effect, without any other devices for energy generation). Therefore, when driven by renewable electricity, the proposed reactor configuration promises a high potential to address the decarbonization challenge in the near-term future. These results highlighted how an effective and feasible process intensification is possible with this innovative system, in particular for a distributed hydrogen production.

Moreover, the overall system was modelled by using COMSOL Multiphysics software in terms of electromagnetic field and temperature distribution along the SiC monolith. The comparison of the experimental and modelling results has shown that the developed model was able to fit the experimental data in terms of temperature distribution inside the SiC monolith during both the MW-assisted heating phase and during an isotherm phase.

Chapter 7

References

1. Stefanidis, G.D.; Muñoz, A.N.; Sturm, G.S.J.; Stankiewicz, A. A Helicopter View of Microwave Application to Chemical Processes: Reactions, Separations, and Equipment Concepts. *Rev. Chem. Eng.* **2014**, *30*, 233–259, doi:10.1515/revce-2013-0033.
2. Van Gerven, T.; Stankiewicz, A. Structure, Energy, Synergy, Time-the Fundamentals of Process Intensification. *Ind. Eng. Chem. Res.* **2009**, *48*, 2465–2474, doi:10.1021/ie801501y.
3. Gedye, R.N.; Rank, W.; Westaway, K.C. The Rapid Synthesis of Organic Compounds in Microwave Ovens. II. *Can. J. Chem.* **1991**, *69*, 706–711, doi:10.1139/v91-106.
4. Gedye, R.; Smith, F.; Westaway, K.; Ali, H.; Baldisera, L.; Laberge, L.; Rousell, J. The Use of Microwave Ovens for Rapid Organic Synthesis. *Tetrahedron Lett.* **1986**, *27*, 279–282, doi:10.1016/S0040-4039(00)83996-9.
5. Horikoshi, S.; Schiffmann, R.F.; Fukushima, J.; Serpone, N. *Microwave Chemical and Materials Processing: A Tutorial*; Springer Nature Singapore Pte Ltd: Singapore, 2017; doi:10.1007/978-981-10-6466-1.
6. Spencer, P.L. Means for Treating Foodstuffs. US Patent US2605383A, 29 July 1952.
7. McArthur, E.D. Electric Heating Apparatus. US Patent US1900573A, 7 March 1933.
8. Palma, V., Barba, D., Cortese, M., Martino, M., Renda S., Meloni, E. (**2020**) Microwaves and Heterogeneous Catalysis: A Review on Selected Catalytic Processes, Catalysts, 10(2), 246; 1-58, doi:10.3390/catal10020246
9. Horikoshi, S.; Serpone, N. Role of Microwaves in Heterogeneous Catalytic Systems. *Catal. Sci. Technol.* **2014**, *4*, 1197–1210, doi:10.1039/c3cy00753g.
10. Kappe, C.O. Controlled Microwave Heating in Modern Organic Synthesis. *Angew. Chem.-Int. Ed.* **2004**, *43*, 6250–6284, doi:10.1002/anie.200400655.
11. Horikoshi, S.; Hidaka, H.; Serpone, N. Environmental Remediation by an Integrated Microwave/UV-Illumination Method. 1. Microwave-Assisted Degradation of Rhodamine-B Dye in Aqueous TiO_2 Dispersions. *Environ. Sci. Technol.* **2002**, *36*, 1357–1366, doi:10.1021/es010941r.
12. Kuang, W.; Nelson, S.O. Dielectric Relaxation Characteristics of Fresh Fruits and Vegetables from 3 to 20 GHz. *J. Microw. Power E. Energy* **1997**, *32*, 114–122, doi:10.1080/08327823.1997.11688332.

13. Dissado, L. Dielectric Response. In *Springer Handbook of Electronic and Photonic Materials*, 2nd ed.; Kasap, S., Capper, P., Eds.; Springer International Publishing AG: Cham, Switzerland, **2017**, 219 – 245, doi:10.1007/978-3-319-48933-9.
14. Horikoshi, S.; Serpone, N. *Microwaves in Catalysis: Methodology and Applications*; Horikoshi, S., Serpone, N., Eds.; Wiley-VCH Verlag GmbH & Co. KGaA: Weinheim, Germany, **2016**.
15. Horikoshi, S.; Sumi, T.; Serpone, N. Unusual Effect of the Magnetic Field Component of the Microwave Radiation on Aqueous Electrolyte Solutions. *J. Microw. Power Electromagn. Energy* **2012**, *46*, 215–228, doi:10.1080/08327823.2012.11689838.
16. Sun, J.; Wang, W.; Yue, Q. Review on Microwave-Matter Interaction Fundamentals and Efficient Microwave-Associated Heating Strategies. *Materials* **2016**, *9*, 231, doi:10.3390/ma9040231.
17. Khaled, D. El; Novas, N.; Gazquez, J.A.; F. Manzano-Agugliaro. Microwave Dielectric Heating: Applications on Metals Processing. *Renew. Sustain. Energy Rev.* **2018**, *82*, 2880–2892, doi:10.1016/j.rser.2017.10.043.
18. Horikoshi, S., Serpone, N. *Microwaves in Nanoparticle Synthesis: Fundamentals and Applications*; Horikoshi, S., Serpone, N., Eds.; Wiley-VCH Verlag GmbH: Baden, Germany, **2013**.
19. Kappe, C.O. Microwave Dielectric Heating in Synthetic Organic Chemistry. *Chem. Soc. Rev.* **2008**, *37*, 1127–1139, doi:10.1039/b803001b.
20. Kappe, C.O.; Dallinger, D.; Murphree, S.S. *Practical Microwave Synthesis for Organic Chemists: Strategies, Instruments, and Protocols*; WILEY-VCH Verlag GmbH & Co. KGaA: Weinheim, Germany, **2009**, doi:10.1002/9783527623907.
21. Hajek, M. Microwave Catalysis in Organic Synthesis. In *Microwaves in Organic Synthesis*; Loupy, A., Ed.; Wiley-VCH Verlag GmbH: Baden, Germany, **2006**, 615 – 652, doi:10.1002/9783527619559.
22. Loupy, A.; Petit, A.; Bogdal, D. Microwaves and Phase-Transfer Catalysis. In *Microwaves in Organic Synthesis*; Wiley-VCH Verlag GmbH: Baden, Germany, **2006**, 287 – 326, doi:10.1002/9783527619559.
23. Laird, T. *Microwave Heating as a Tool for Sustainable Chemistry*; Leadbeater, N.E., Ed.; CRC Press: Boca Raton, FL, USA, **2011**, doi:10.1002/cssc.201100003.
24. Nain, S.; Singh, R.; Ravichandran, S. Importance of Microwave Heating in Organic Synthesis. *Adv. J. Chem. A* **2019**, *2*, 94–104, doi:10.29088/SAMI/AJCA.2019.2.94104.

25. Bond, G.; Moyes, R.B.; Whan, D.A. Recent Applications of Microwave Heating in Catalysis. *Catal. Today* **1993**, *17*, 427–437, doi:10.1016/0920-5861(93)80046-4.
26. Xu, W.; Zhou, J.; Su, Z.; Ou, Y.; You, Z. Microwave Catalytic Effect: A New Exact Reason for Microwave-Driven Heterogeneous Gas-Phase Catalytic Reactions. *Catal. Sci. Technol.* **2016**, *6*, 698–702, doi:10.1039/c5cy01802a.
27. Díaz-Ortiz; Prieto, P.; de la Hoz, A. A Critical Overview on the Effect of Microwave Irradiation in Organic Synthesis. *Chem. Rec.* **2019**, *19*, 85–97, doi:10.1002/tcr.201800059.
28. Zhang, X.; Hayward, D.O.; Mingos, D.M.P. Effects of Microwave Dielectric Heating on Heterogeneous Catalysis. *Catal. Lett.* **2003**, *88*, 33–38, doi:10.1023/A:1023530715368.
29. Haneishi, N.; Tsubaki, S.; Abe, E.; Maitani, M.M.; Suzuki, E. Enhancement of Fixed-Bed Flow Reactions under Microwave Irradiation by Local Heating at the Vicinal Contact Points of Catalyst Particles. *Sci. Rep.* **2019**, *9*, 222, doi:10.1038/s41598-018-35988-y.
30. Jonscher, A.K. Dielectric Relaxation in Solids. *J. Phys. D. Appl. Phys.* **1999**, *32*, R57–R70, doi:10.1088/0022-3727/32/14/201.
31. Cherbański, R.; Molga, E. Intensification of Desorption Processes by Use of Microwaves-An Overview of Possible Applications and Industrial Perspectives. *Chem. Eng. Process. Process Intensif.* **2009**, *48*, 48–58, doi:10.1016/j.cep.2008.01.004.
32. Roy, R.; Agrawal, D.; Cheng, J.; Gedevanlshvili, S. Full Sintering of Powdered-Metal Bodies in a Microwave Field. *Nature* **1999**, *399*, 668–670, doi:10.1038/21390.
33. Rosa, R.; Veronesi, P.; Casagrande, A.; Leonelli, C. Microwave Ignition of the Combustion Synthesis of Aluminides and FiEld-Related Effects. *J. Alloys Compd.* **2016**, *657*, 59–67, doi:10.1016/j.jallcom.2015.10.044.
34. Horikoshi, S.; Osawa, A.; Abe, M.; Serpone, N. On the Generation of Hot-Spots by Microwave Electric and Magnetic Fields and Their Impact on a Microwave-Assisted Heterogeneous Reaction in the Presence of Metallic Pd Nanoparticles on an Activated Carbon Support. *J. Phys. Chem. C* **2011**, *115*, 23030–23035, doi:10.1021/jp2076269.
35. Cheng, J.; Roy, R.; Agrawal, D. Radically Different Effects on Materials by Separated Microwave Electric and Magnetic Fields. *Mater. Res. Innov.* **2002**, *5*, 170–177, doi:10.1007/s10019-002-8642-6.
36. Stankiewicz, A.; Sarabi, F.E.; Baubaid, A.; Yan, P.; Nigar, H. Perspectives of Microwaves-Enhanced Heterogeneous Catalytic Gas-Phase Processes in Flow Systems. *Chem. Rec.* **2019**, *19*, 40–50, doi:10.1002/tcr.201800070.

37. Sarabi, E.F.; Ghorbani, M.; Stankiewicz, A.; Nigar, H. Coaxial Traveling-Wave Microwave Reactors: Design Challenges and Solutions. *Chem. Eng. Res. Des.* **2019**, *153*, 677–683, doi:10.1016/j.cherd.2019.11.022.
38. Bolt A., Dincer I., Agelin-Chaab M., **2020**, Experimental study of hydrogen production process with aluminum and water. *Int. J. Hydrogen Energy* **2020**, *45*, 14232 – 14244. 10.1016/j.ijhydene.2020.03.160
39. Siddiqui O., Ishaq H., Chehade G., Dincer I., Experimental investigation of an integrated solar powered clean hydrogen to ammonia synthesis system. *Appl. Therm. Eng.* **2020**, *176*, 115443. 10.1016/j.applthermaleng.2020.115443
40. Eveloy V. and Gebreegziabher T., A Review of Projected Power-to-Gas Deployment Scenarios, *Energies* **2018**, *11*, 1824; 1-52. doi:10.3390/en11071824
41. Hogerwaard J., Dincer I., Naterer G.F., **2020**, Experimental investigation and optimization of integrated photovoltaic and photoelectrochemical hydrogen generation. *Energy Convers. Manage.* **2020**, *207*, 112541. 10.1016/j.enconman.2020.112541
42. Razi F., Dincer I., Gabriel K., Thermal management of a new integrated copper-chlorine cycle for hydrogen production. *Energy Convers. Manage.* **2020**, *212*, 112629. 10.1016/j.enconman.2020.112629
43. Angeli S. D., Monteleone G., Giaconia A., Lemonidou A.A., State-of-the-art catalysts for CH_4 steam reforming at low temperature – review. *Int. J. Hydrogen Energy* **2014**, *39*, 1979 - 1997. http://dx.doi.org/10.1016/j.ijhydene.2013.12.001
44. Sikander U., Sufian S., Salam M.A., A review of hydrotalcite based catalysts for hydrogen production systems. *Int. J. Hydrogen Energy* **2017**, *42*, 19851 - 19868. http://dx.doi.org/10.1016/j.ijhydene.2017.06.089
45. Ma Y., Ma Y., Long G., Li J., Hu X., Ye Z., Wang Z., Buckley C.E., Dong D., Synergistic promotion effect of MgO and CeO_2 on nanofibrous Ni/Al_2O_3 catalysts for methane partial oxidation. *Fuel*, **2019**, 258, 116103 https://doi.org/10.1016/j.fuel.2019.116103
46. Palma V., Miccio M., Ricca A., Meloni E., Ciambelli P., Monolithic catalysts for methane steam reforming intensification: Experimental and numerical investigations. *Fuel* **2014**, *138*, 80–90, http://dx.doi.org/10.1016/j.fuel.2014.06.043
47. Alvarez-Galvan C, Melian M, Ruiz-Matas L, Eslava JL, Navarro RM, Ahmadi M, Roldan Cuenya B and Fierro JLG, Partial Oxidation of Methane to Syngas Over Nickel-Based Catalysts: Influence of Support Type, Addition of Rhodium, and Preparation Method. *Front. Chem.*, **2019**, 7:104, 1-16 doi: 10.3389/fchem.2019.0010

48. Pinheiro A.L., Pinheiro A. N., Valentini A., Filho J. M., de Sousa F. F., de Sousa J. R., Rocha M. da Graça C., Bargiela P., Oliveira A. C., Analysis of coke deposition and study of the structural features of MAl_2O_4 catalysts for the dry reforming of methane. *Catalysis Communications*, **2009**, *11*, 11–14. 10.1016/j.catcom.2009.08.003
49. Hu D., Liu C., Li L., Lv K-L, Zhang Y-H, Li J-L., Carbon dioxide reforming of methane over nickel catalysts supported on TiO_2(001) nanosheets. *Int. J. Hydrogen Energy* **2018**, *43*, 21345 – 21354. https://doi.org/10.1016/j.ijhydene.2018.09.188
50. Lercher, J.A.; Bitter, J.H.; Hally, W.; Niessen, W.; Seshan, K. Design of stable catalysts for methane-carbon dioxide reforming. *Stud. Surf. Sci. Catal.* **1996**, *101*, 463-472; https://doi.org/10.1016/S0167-2991(96)80257-6.
51. Pinheiro A. N., Valentini A., Sasaki J. M., Oliveira A. C., Highly stable dealuminated zeolite support for the production of hydrogen by dry reforming of methane. *Appl. Catal., A*, **2009**, *355*, 156–168 10.1016/j.apcata.2008.12.007
52. Ramezani Y., Meshkani F., Rezaei M., Promotional effect of Mg in trimetallic nickelmanganese-magnesium nanocrystalline catalysts in CO_2 reforming of methane. *Int. J. Hydrogen Energy* **2018**, *43*, 22347 – 22356. https://doi.org/10.1016/j.ijhydene.2018.09.222
53. Alrafei B., Polaert I., Ledoux A., Azzolina-Jury F., Remarkably stable and efficient Ni and Ni-Co catalysts for CO_2 methanation. *Catal. Today* **2020**, *346*, 23 – 33. https://doi.org/10.1016/j.cattod.2019.03.026
54. Oton L. F., Coelho D. C., Oliveira Alcineia C., de Araujo J. C.S., Lang R., Rodríguez-Castellón E., Rodríguez-Aguado E., Lucredio A. F., Assaf E. M., Reyna-Alvarado J., López-Galán O. A., Ramos M., Structural transformation of vanadate nanotubes into vanadate oxides nanostructures during the dry reforming of methane. *Mol. Catal.*, **2020**, *480*, 110641 https://doi.org/10.1016/j.mcat.2019.110641
55. Rezaei R., Moradi G., Study of the performance of dry methane reforming in a microchannel reactor using sputtered Ni/Al_2O_3 coating on stainless steel. *Int. J. Hydrogen Energy* **2018**, *43,* 21374 – 21385 https://doi.org/10.1016/j.ijhydene.2018.09.200
56. Chotirach M., Tungasmita S., Tungasmita D. N., Tantayanon S., Titanium nitride promoted Ni-based SBA-15 catalyst for dry reforming of methane. *Int. J. Hydrogen Energy* **2018**, *43,* 21322 – 21332 https://doi.org/10.1016/j.ijhydene.2018.09.205
57. Sepehri S., Rezaei M., Wang Y., Younesi A., Arandiyan H., The evaluation of autothermal methane reforming for hydrogen production over Ni/CeO_2 catalysts. *Int. J. Hydrogen Energy* **2018**, *43,* 22340 – 22346 https://doi.org/10.1016/j.ijhydene.2018.10.016

58. Eugenio Meloni, Marco Martino, Giuseppina Iervolino, Concetta Ruocco, Simona Renda, Giovanni Festa, Vincenzo Palma, The Route from Green H_2 Production through Bioethanol Reforming to CO_2 Catalytic Conversion: A Review, *Energies* **2022**, *15*, 2383. Doi: 10.3390/en15072383
59. Lixin Fan, Zhengkai Tu, Siew Hwa Chan, Recent development of hydrogen and fuel cell technologies: A review, *Energy Reports* **2021**, *7*, 8421 – 8446. Doi: 10.1016/j.egyr.2021.08.003.
60. Meiling Yue, Hugo Lambert, Elodie Pahon, Robin Roche, Samir Jemei, Daniel Hissel, Hydrogen energy systems: A critical review of technologies, applications, trends and challenges, *Renewable Sustainable Energy Rev.* **2021**, *146*, 111180. Doi: 10.1016/j.rser.2021.111180
61. Hanxi Wang, Jianling Xu, Lianxi Sheng, Xuejun Liu, Yue Lu, Wei Li, A review on bio-hydrogen production technology, *Int J Energy Res.* **2018**, *42*, 3442 – 3453, doi: 10.1002/er.4044.
62. Wismann S.T., Engbæk J.S., Vendelbo S.B., Bendixen F.B., Eriksen W.L., Aasberg-Petersen K., Frandsen C., Chorkendor I., Mortensen P.M., Electrified methane reforming: A compact approach to greener industrial hydrogen production. *Science* **2019**, *364*, 756 – 759. 10.1126/science.aaw8775
63. Meloni E., Martino M., Palma V., A Short Review on Ni Based Catalysts and Related Engineering Issues for Methane Steam Reforming, *Catalysts* **2020**, *10(3), 352*, 1 - 38; https://doi.org/10.3390/catal10030352
64. Ali, S.; Al-Marri, M.J.; Abdelmoneim, A.J.; Kumar, A.; Khader, M.M. Catalytic evaluation of nickel nanoparticles in methane steam reforming. *Int. J. Hydrog. Energy* **2016**, *41*, 22876–22885, doi:10.1016/j.ijhydene.2016.08.200.
65. Katheria, S.; Gupta, A.; Deo, G.; Kunzru, D. Effect of calcination temperature on stability and activity of $Ni/MgAl_2O_4$ catalyst for steam reforming of methane at high pressure condition. *Int. J. Hydrog. Energy* **2016**, *41*, 14123–14132, doi:10.1016/j.ijhydene.2016.05.109.
66. Rogers, J.L.; Mangarella, M.C.; D'Amico, A.D.; Gallagher, J.R.; Dutzer, M.R.; Stavitski, E.; Miller, J.T.; Sievers, C. Differences in the Nature of Active Sites for Methane Dry Reforming and Methane Steam Reforming over Nickel Aluminate Catalysts. *ACS Catal.* **2016**, *6*, 5873−5886, doi:10.1021/acscatal.6b01133.
67. Pechini, M.P. Method of Preparing Lead and Alkaline Earth Titanates and Niobates and Coating Method Using the Same to Form a Capacitor. U.S. Patent 3,3306,97A, 11 July 1967.
68. Khani, Y.; Shariatinia, Z.; Bahadoran, F. High catalytic activity and stability of $ZnLaAlO_4$ supported Ni, Pt and Ru nanocatalysts applied in

the dry, steam and combined dry-steam reforming of methane. *Chem. Eng. J.* **2016**, *299*, 353–366, doi:10.1016/j.cej.2016.04.108.

69. Fang, X.; Zhang, X.; Guo, Y.; Chen, M.; Liu, W.; Xu, X.; Peng, H.; Gao, Z.; Wang, X.; Li, C. Highly active and stable Ni/$Y_2Zr_2O_7$ catalysts for methane steam reforming: On the nature and effective preparation method of the pyrochlore support. *Int. J. Hydrog. Energy* **2016**, *41*, 11141–11153, doi:10.1016/j.ijhydene.2016.04.038.
70. Thalinger, R.; Gocyla, M.; Heggen, M.; Dunin-Borkowski, R.; Grünbacher, M.; Stöger-Pollach, M.; Schmidmair, D.; Klötzer, B.; Penner, S. Ni–perovskite interaction and its structural and catalytic consequences in methane steam reforming and methanation reactions. *J. Catal.* **2016**, *337*, 26–35, doi:10.1016/j.jcat.2016.01.020.
71. Yoo, J.; Park, S.; Hwan Song, J.; Yoo, S.; Kyu Song, I. Hydrogen production by steam reforming of natural gas over butyric acid-assisted nickel/alumina catalyst. *Int. J. Hydrog. Energy* **2017**, *42*, 28377–28385, doi:10.1016/j.ijhydene.2017.09.148.
72. Iglesias, I.; Baronetti, G.; Marino, F. Ni/$Ce_{0.95}M_{0.05}O_2$-d (M = Zr, Pr, La) for methane steam reforming at mild conditions. *Int. J. Hydrog. Energy* **2017**, *42*, 29735 – 29744, doi:10.1016/j.ijhydene.2017.09.176.
73. Aghayan, M.; Potemkin, D.I.; Rubio-Marcos, F.; Uskov, S.I.; Snytnikov, P.V.; Hussainova, I. Template-Assisted Wet-Combustion Synthesis of Fibrous Nickel Based Catalyst for Carbon Dioxide Methanation and Methane Steam Reforming. *ACS Appl. Mater. Interfaces* **2017**, *9*, 43553 − 43562, doi:10.1021/acsami.7b08129.
74. Park, Y.S.; Kang, M.; Byeon, P.; Chung, S.Y.; Nakayama, T.; Ko, T.; Hwang, H. Fabrication of a regenerable Ni supported NiO-MgO catalyst for methane steam reforming by exsolution. *J. Power Sources* **2018**, *397*, 318 – 324, doi:10.1016/j.jpowsour.2018.07.025.
75. Zhang, X.; Peng, L.; Fang, X.; Cheng, Q.; Liu, W.; Peng, H.; Gao, Z.; Zhou, W.; Wang, X. Ni/$Y_2B_2O_7$ (B=Ti, Sn, Zr and Ce) catalysts for methane steam reforming: On the effects of B site replacement. *Int. J. Hydrog. Energy* **2018**, *43*, 8298 – 8312, doi:10.1016/j.ijhydene.2018.03.086.
76. Chen, C.; Wang, X.; Chen, X.; Liang, X.; Zou, X.; Lu, X. Combined steam and CO_2 reforming of methane over one-pot prepared Ni/La-Si catalysts. *Int. J. Hydrog. Energy* **2019**, *44*, 4780 – 4793, doi:10.1016/j.ijhydene.2019.01.019.
77. Fang, X.; Xu, L.; Zhang, X.; Zhang, K.; Dai, H.; Liu, W.; Xu, X.; Wang, X.; Zhou, W. Effect of rare earth element (Ln = La, Pr, Sm, and Y) on physicochemical properties of the Ni/$Ln_2Ti_2O_7$ catalysts for the steam reforming of methane. *Mol. Catal.* **2019**, *468*, 130 – 138, doi:10.1016/j.mcat.2019.02.022.

78. Iglesias, I.; Baronetti, G.; Alemany, L.; Mariño, F. Insight into Ni/Ce$_{1-X}$Zr$_X$O$_{2-\delta}$ support interplay for enhanced methane steam reforming. *Int. J. Hydrog. Energy* **2019**, *44*, 3668 – 3680, doi:10.1016/j.ijhydene.2018.12.112.
79. Iglesias, I.; Forti, M.; Baronetti, G.; Mariño, F. Zr-enhanced stability of ceria based supports for methane steam reforming at severe reaction conditions. *Int. J. Hydrog. Energy* **2019**, *44*, 8121 – 8132, doi:10.1016/j.ijhydene.2019.02.070.
80. Sebai, I.; Boulahaouache, A.; Trari, M.; Salhi, N. Preparation and characterization of 5%Ni/γ-Al$_2$O$_3$ catalysts by complexation with NH$_3$ derivatives active in methane steam reforming. *Int. J. Hydrog. Energy* **2019**, *44*, 9949 – 9958, doi:10.1016/j.ijhydene.2018.12.050.
81. Dan, M.; Mihet, M.; Lazar, M.D. Hydrogen and/or syngas production by combined steam and dry reforming of methane on nickel catalysts. *Int. J. Hydrog. Energy* **2020**, doi:10.1016/j.ijhydene.2019.12.158.
82. Hu, Y.H.; Ruckenstein, E. Catalytic Conversion of Methane to Synthesis Gas by Partial Oxidation and CO$_2$ Reforming. *Adv. Catal.* **2004**, *48*, 297 – 345, doi:10.1016/S0360-0564(04)48004-3.
83. Rostrup-Nielsen, J.R. New aspects of syngas production and use. *Catal. Today* **2000**, *63*, 159 – 164, doi:10.1016/S0920-5861(00)00455-7.
84. Liu, C.-J.; Ye, J.; Jiang, J.; Pan, Y. Progresses in the Preparation of Coke Resistant Ni-based Catalyst for Steam and CO$_2$ Reforming of Methane. *ChemCatChem* **2011**, *3*, 529 – 541, doi:10.1002/cctc.201000358.
85. Ligthart, D.A.J.M.; Pieterse, J.A.Z.; Hensen, E.J.M. The role of promoters for Ni catalysts in low temperature (membrane) steam methane reforming. *Appl. Cat. A Gen.* **2011**, *405*, 108 – 119, doi:10.1016/j.apcata.2011.07.035.
86. Weststrate, C.J.; Saib, A.M.; Niemantsverdriet, J.W. Promoter segregation in Pt and Ru promoted cobalt model catalysts during oxidation–reduction treatments. *Catal. Today* **2013**, *215*, 2 – 7, doi:10.1016/j.cattod.2013.01.009.
87. Available online: https://www.britannica.com/science/promoter-catalysis
88. Morales-Cano, F.; Lundegaard, L.F.; Tiruvalam, R.R.; Falsig, H.; Skjøth-Rasmussen, M.S. Improving the sintering resistance of Ni/Al2O3 steam-reforming catalysts by promotion with noble metals. *Appl. Catal. A Gen.* **2015**, *498*, 117 – 125, doi:10.1016/j.apcata.2015.03.016.
89. Lertwittayanon, K.; Youravong, W.; Jye Lau, W. Enhanced catalytic performance of Ni/α-Al2O3 catalyst modified with CaZrO$_3$ nanoparticles in steam-methane reforming. *Int. J. Hydrog. Energy* **2017**, *42*, 28254 – 28265, doi:10.1016/j.ijhydene.2017.09.030.

90. Jaiswar, V.K.; Katheria, S.; Deo, G.; Kunzru, D. Effect of Pt doping on activity and stability of Ni/$MgAl_2O_4$ catalyst for steam reforming of methane at ambient and high pressure condition. *Int. J. Hydrog. Energy* **2017**, *42*, 18968 – 18976, doi:10.1016/j.ijhydene.2017.06.096.
91. Azancot, L.; Bobadilla, L.F.; Santos, J.L.; Cordoba, J.M.; Centeno, M.A.; Odriozola, J.A. Influence of the preparation method in the metal-support interaction and reducibility of Ni-Mg-Al based catalysts for methane steam reforming. *Int. J. Hydrog. Energy* **2019**, *44*, 19827 – 19840, doi:10.1016/j.ijhydene.2019.05.167.
92. Boudjeloud, M.; Boulahouache, A.; Rabia, C.; Salhi, N. La-doped supported Ni catalysts for steam reforming of methane. *Int. J. Hydrog. Energy* **2019**, *44*, 9906 – 9913, doi:10.1016/j.ijhydene.2019.01.140.
93. Nazari, M.; Mehdi Alavi, S. An investigation of the simultaneous presence of Cu and Zn in different Ni/Al_2O_3 catalyst loads using Taguchi design of experiment in steam reforming of methane. *Int. J. Hydrog. Energy* **2020**, *45*, 691 – 702, doi:10.1016/j.ijhydene.2019.10.224.
94. Phanawadee, P.; Laipraseard, K.; Yablonsky, G.S.; Constales, D.; Jamroonrote, W.; Jaipet, P. Estimation of the remaining lifetime of deactivated catalyst via the spatial average catalyst activity illustrated by the water–gas shift and steam methane reforming processes. *Reac. Kinet. Mech. Cat.* **2017**, *121*, 371 – 385, doi:10.1007/s11144-017-1170-6.
95. Argyle, M.D.; Bartholomew, C.H. Heterogeneous Catalyst Deactivation and Regeneration: A Review. *Catalysts* **2015**, *5*, 145 – 269, doi:10.3390/catal5010145.
96. Ochoa, A.; Bilbao, J.; Gayubo, A.G.; Castano, P. Coke formation and deactivation during catalytic reforming of biomass and waste pyrolysis products: A review. *Renew. Sustain. Energy Rev.* **2020**, *119*, 109600, doi:10.1016/j.rser.2019.109600.
97. Hashemnejad, S.M.; Parvari, M. Deactivation and Regeneration of Nickel-Based Catalysts for Steam-Methane Reforming. *Chin. J. Catal.* **2011**, *32*, 273 – 279, doi:10.1016/S1872-2067(10)60175-1.
98. Jablonski, W.S.; Villano, S.M.; Dean, A.M. A comparison of H_2S, SO_2, and COS poisoning on Ni/YSZ and Ni/K_2O-$CaAl_2O_4$ during methane steam and dry reforming. *Appl. Cat. A General* **2015**, *502*, 399 – 409, doi:10.1016/j.apcata.2015.06.009.
99. Yang, X. An experimental investigation on the deactivation and regeneration of a steam reforming catalyst. *Renew. Energy* **2017**, *112*, 17 – 24, doi:10.1016/j.renene.2017.05.018.
100. Laprune, D.; Theodoridi, C.; Tuel, A.; Farrusseng, D.; Meunier, F.C. Effect of polyaromatic tars on the activity for methane steam reforming

of nickel particles embedded in silicalite-1. *Appl. Catal. B Environ.* **2017**, *204*, 515 – 524, doi:10.1016/j.apcatb.2016.12.004.

101. Li, S.; Burel, L.; Aquino, C.; Tuel, A.; Morfin, F.; Rousset, J.-L.; Farrusseng, D. Ultimate size control of encapsulated gold nanoparticles. *Chem. Commun.* **2013**, *49*, 8507 – 8509, doi:10.1039/C3CC44843F.
102. Haynes, D.J.; Shekhawat, D.; Berry, D.; Roy, A.; Spivey, J.J. Effect of calcination temperature on steam reforming activity of Ni-based pyrochlore catalysts. *J. Rare Earths* **2019**, *38 (7)*, 711 – 718. doi:10.1016/j.jre.2019.07.015.
103. Hernandez, A.D.; Kaisalo, N.; Simell, P.; Scarsella, M. Effect of H_2S and thiophene on the steam reforming activity of nickel and rhodium catalysts in a simulated coke oven gas stream. *Appl. Cat. B Environ.* **2019**, *258*, 117977, doi:10.1016/j.apcatb.2019.117977.
104. Karthik, G.M.; Buwa, V. Particle-Resolved Simulations of Methane Steam Reforming in Multilayered Packed Beds. *AIChE J.* **2018**, *64*, 4162 – 4176, doi:10.1002/aic.16386.
105. Pashchenko, D. Experimental investigation of reforming and flow characteristics of a steam methane reformer filled with nickel catalyst of various shapes. *Energy Convers. Manag.* **2019**, *185*, 465 – 472, doi:10.1016/j.enconman.2019.01.103.
106. Park, H.-G.; Han, S.-Y.; Jun, K.-W.; Woo, Y.; Park, M.-J.; Kim, S.K. Bench-Scale Steam Reforming of Methane for Hydrogen Production. *Catalysts* **2019**, *9*, 615, doi:10.3390/catal9070615.
107. Kim, Y.; Cho, E.; Ko, C.H. Preparation of Ni-based egg-shell-type catalyst on cylinder-shaped alumina pellets and its application for hydrogen production via steam methane reforming. *Int. J. Hydrog. Energy* **2019**, *44*, 5314 – 5323, doi:10.1016/j.ijhydene.2018.08.100.
108. Fukuhara, C.; Yamamoto, K.; Makiyama, Y.; Kawasaki, W.; Watanabe, R. A metal-honeycomb-type structured catalyst for steam reforming of methane: Effect of preparation condition change on reforming performance. *Appl. Catal. A Gen.* **2015**, *492*, 190 – 200, doi:10.1016/j.apcata.2014.11.040.
109. Gouveia Gil, A.; Wu, Z.; Chadwick, D.; Li, K. Microstructured Catalytic Hollow Fiber Reactor for Methane Steam Reforming. *Ind. Eng. Chem. Res.* **2015**, *54*, 5563 − 5571, doi:10.1021/ie504953j.
110. Zhang, N.; Chen, X.; Chu, B.; Cao, C.; Jin, Y.; Cheng, Y. Catalytic performance of Ni catalyst for steam methane reforming in a micro-channel reactor at high pressure. *Chem. Eng. Process. Process. Intensif.* **2017**, *118*, 19 – 25, doi:10.1016/j.cep.2017.04.015.
111. Calisan, A.; Ogulgonen, C.G.; Yilmaz, A.; Uner, D.; Kincal, S. Steam methane reforming over structured reactors under concentrated solar irradiation. *Int. J. Hydrog. Energy* **2019**, *44*, 18682 – 18693, doi:10.1016/j.ijhydene.2019.04.033.

112. Xu, Y.; Ma, Y.; Demura, M.; Hirano, T. Enhanced catalytic activity of Ni_3Al foils towards methane steam reforming by water vapor and hydrogen pretreatments. *Int. J. Hydrog. Energy* **2016**, *41*, 7352 – 7362, doi:10.1016/j.ijhydene.2016.03.103.
113. Mundhwa, M.; Parmar, R.D.; Thurgood, C.P. A comparative parametric study of a catalytic plate methane reformer coated with segmented and continuous layers of combustion catalyst for hydrogen production. *J. Power Sources* **2017**, *344*, 85 – 102, doi:10.1016/j.jpowsour.2017.01.082.
114. Mundhwa, M.; Thurgood, C.P. Numerical study of methane steam reforming and methane combustion over the segmented and continuously coated layers of catalysts in a plate reactor. *Fuel Process. Technol.* **2017**, *158*, 57 – 72, doi:10.1016/j.fuproc.2016.12.002.
115. Hirano, T.; Xu, Y. Catalytic properties of a pure Ni coil catalyst for methane steam reforming. *Int. J. Hydrog. Energy* **2017**, *42*, 30621 – 30629, doi:10.1016/j.ijhydene.2017.10.135.
116. Xu, Y.; Harimoto, T.; Hirano, T.; Ohata, H.; Kunieda, H.; Hara, Y.; Miyata, Y. Catalytic performance of a high-cell-density Ni honeycomb catalyst for methane steam reforming. *Int. J. Hydrog. Energy* **2018**, *43*, 15975 – 15984, doi:10.1016/j.ijhydene.2018.06.175.
117. Xu, Y.; Harimoto, T.; Wang, L.; Hirano, T.; Kunieda, H.; Hara, Y.; Miyata, Y. Effect of steam and hydrogen treatments on the catalytic activity of pure Ni honeycomb for methane steam reforming. *Chem. Eng. Process. Process. Intensif.* **2018**, *129*, 63 – 70, doi:10.1016/j.cep.2018.05.004.
118. Settar, A.; Abboudi, S.; Lebaal, N. Effect of inert metal foam matrices on hydrogen production intensification of methane steam reforming process in wall-coated reformer. *Int. J. Hydrog. Energy* **2018**, *43*, 12386 – 12397, doi:10.1016/j.ijhydene.2018.04.215.
119. Ashraf, M.A.; Sanz, O.; Montes, M.; Specchia, S. Insights into the effect of catalyst loading on methane steam reforming and controlling regime for metallic catalytic monoliths. *Int. J. Hydrog. Energy* **2018**, *43*, 11778 – 11792, doi:10.1016/j.ijhydene.2018.04.126.
120. Shigarov, A.B.; Kirillov V.A.; Amosov Y.I.; Brayko, A.S.; Avakov, V.B.; Landgraf, I.K.; Urusov, A.R.; Jivulko, S.A.; Izmaylovich, V.V. Membrane reformer module with Ni-foam catalyst for pure hydrogen production from methane: Experimental demonstration and modelling. *Int. J. Hydrog. Energy* **2017***, 42,* 6713 – 6728, doi:10.1016/j.ijhydene.2016.12.057.
121. Pajak, M.; Mozdzierz, M.; Chalusiak, M.; Kimijima, S.; Szmyd, J.S.; Brus, G. A numerical analysis of heat and mass transfer processes in a macro-patterned methane/steam reforming reactor. *Int. J. Hydrog. Energy* **2018**, *43*, 20474 – 20487, doi:10.1016/j.ijhydene.2018.09.058.

122. Katheria, S.; Deo, G.; Kunzru, D. Rh-Ni/$MgAl_2O_4$ catalyst for steam reforming of methane: Effect of Rh doping, calcination temperature and its application on metal monoliths. *Appl. Catal. A* **2019**, *570*, 308 – 318, doi:10.1016/j.apcata.2018.11.021.
123. Balzarotti, R.; Ambrosetti, M.; Beretta, A.; Groppi, G.; Tronconi, E. Investigation of packed conductive foams as a novel reactor configuration for methane steam reforming. *Chem. Eng. J.* **2019**, doi:10.1016/j.cej.2019.123494.
124. Palma, V.; Ricca, A.; Meloni, E.; Martino, M.; Miccio, M.; Ciambelli, P. Experimental and numerical investigations on structured catalysts for methane steam reforming intensification. *J. Clean. Prod.* **2016**, *111*, 217 – 230, doi:10.1016/j.jclepro.2015.09.004.
125. Noh, Y.S.; Lee, K.-Y.; Moon, D.J. Hydrogen production by steam reforming of methane over nickel based structured catalysts supported on calcium aluminate modified SiC. *Int. J. Hydrog. Energy* **2019**, *44*, 21010 – 21019, doi:10.1016/j.ijhydene.2019.04.287.
126. Ashraf, M.A.; Sanz, O.; Italiano, C.; Vita, A.; Montes, M.; Specchia, S. Analysis of Ru/La-Al_2O_3 catalyst loading on alumina monoliths and controlling regimes in methane steam reforming. *Chem. Eng. J.* **2018**, *334*, 1792 – 1807, doi:10.1016/j.cej.2017.11.154.
127. Inbamrung, P.; Sornchamni, T.; Prapainainar, C.; Tungkamani, S.; Narataruksa, P.; Jovanovic, G.N. Modeling of a square channel monolith reactor for methane steam reforming. *Energy* **2018**, *152*, 383 – 400, doi:10.1016/j.energy.2018.03.139.
128. Jeong, A.; Shin, D.; Baek, S.M.; Nam, J.H. Effectiveness factor correlations from simulations of washcoat nickel catalyst layers for small-scale steam methane reforming applications. *Int. J. Hydrog. Energy* **2018**, *43*, 15398 – 15411, doi:10.1016/j.ijhydene.2018.06.059.
129. Leonzio, G. ANOVA analysis of an integrated membrane reactor for hydrogen production by methane steam reforming. *Int. J. Hydrog. Energy* **2019**, *44*, 11535 – 11545, doi:10.1016/j.ijhydene.2019.03.077.
130. Nguyen, H.M.; Sunarso, J.; Li, C.; Pham, G.H.; Phan, C.; Liu, S. Microwave-assisted catalytic methane reforming: A review. *Appl. Catal. A Gen.* **2020**, *599*, 117620. https://doi.org/10.1016/j.apcata.2020.117620
131. Zhang, X.; Lee, C.S.M.; Mingos, D.M.P.; Hayward, D.O. Carbon Dioxide Reforming of Methane with Pt Catalysts Using Microwave Dielectric Heating. *Catal. Lett.* **2003**, *88*, 129 – 139, doi:10.1023/A:1024049403422.
132. Fidalgo, B.; Arenillas, A.; Menéndez, J.A. Mixtures of Carbon and Ni/Al_2O_3 as Catalysts for the Microwave-Assisted CO_2 Reforming of CH_4. *Fuel Process. Technol.* **2011**, *92*, 1531 – 1536, doi:10.1016/j.fuproc.2011.03.015.

133. Fidalgo, B.; Menéndez, J.A. Study of Energy Consumption in a Laboratory Pilot Plant for the Microwave-Assisted CO_2 Reforming of CH_4. *Fuel Process. Technol.* **2012**, *95*, 55 – 61, doi:10.1016/j.fuproc.2011.11.012.
134. Dominguez, A.; Fernandez, Y.; Fidalgo, B.; Pis, J.J.; Menéndez, J.A. Biogas to Syngas by Microwave-Assisted Dry Reforming in the Presence of Char. *Energy Fuel* **2007**, *21*, 2066 – 2071, doi:10.1021/ef070101j.
135. Sharifvaghefi, S.; Shirani, B.; Eic, M.; Zheng, Y. Application of Microwave in Hydrogen Production from Methane Dry Reforming: Comparison Between the Conventional and Microwave-Assisted Catalytic Reforming on Improving the Energy Efficiency. *Catalysts* **2019**, *9*, 618, doi:10.3390/catal9070618.
136. Li, L.; Jiang, X.; Wang, H.; Wang, J.; Song, Z.; Zhao, X.; Ma, C. Methane Dry and Mixed Reforming on the Mixture of Bio-Char and Nickel-Based Catalyst with Microwave Assistance. *J. Anal. Appl. Pyrolysis* **2017**, *125*, 318 – 327, doi:10.1016/j.jaap.2017.03.009.
137. L.S. Gangurde, G.S.J. Sturm, M.J. ValeroRomero, R. Mallada, J. Santa maria, A.I. Stankiewicz, G.D. Stefanidis, Synthesis, characterization, and application of ruthenium-doped $SrTiO_3$ perovskite catalysts for microwave-assisted methane dry reforming *Chem. Eng. Process. – Process Intensif.* **2018**, *127*, 178 - 190
138. L. Gangurde, Process Intensification of Microwave Assisted Methane Dry Reforming Delft University of Technology (2018)
139. de Dios García, I.; Stankiewicz, A.; Nigar, H. Syngas production via microwave-assisted dry reforming of methane. *Catal. Today* **2020**, *362*, 72 – 80. https://doi.org/10.1016/j.cattod.2020.04.045
140. Wang Y.F., Tsai C.H., Chang W.Y., Kuo Y.M., Methane Steam Reforming for Producing Hydrogen in an Atmospheric-Pressure Microwave Plasma Reactor. *Int. J. Hydrogen Energy* **2010**, *35*, 135–140, doi:10.1016/j.ijhydene.2009.10.088.
141. Meloni E., Palma V., Vaiano V., Optimized microwave susceptible catalytic diesel soot trap, *Fuel* **2017**, *205*, 142 – 152 http://dx.doi.org/10.1016/j.fuel.2017.05.074
142. Eugenio Meloni, Marco Martino, Antonio Ricca, Vincenzo Palma, Ultracompact methane steam reforming reactor based on microwaves susceptible structured catalysts for distributed hydrogen production, *Int. J. Hydrogen Energy* **2021**, *46*, 13729 – 13747. Doi: 10.1016/j.ijhydene.2020.06.299
143. E. Meloni, M. Martino, P. Pullumbi, F.Brandani, V. Palma, Intensification of TSA processes using a microwave-assisted regeneration step, *Chem. Eng. Process.* **2021**, *160*, 108291. Doi: 10.1016/j.cep.2020.108291

144. A. Ramirez, J.L. Hueso, R. Mallada, J. Santamaria, Microwave-activated structured reactors to maximize propylene selectivity in the oxidative dehydrogenation of propane, Chem. Eng. J. **2020**, 124746
145. Haberman B.A., Young J.B., Three-dimensional simulation of chemically reacting gas flows in the porous support structure of an integrated-planar solid oxide fuel cell, *Int. J. Heat Mass Transfer*, **2004**, *47*, 3617–3629
146. Bai, X.; Muley, P.D.; Musho, T.; Abdelsayed, V.; Robinson, B.; Caiola, A.; Shekhawat, D.; Jiang, C.; Hu, J. A combined experimental and modeling study of Microwave-assisted methane dehydroaromatization process. *Chem. Eng. J.* **2022**, *433*, 134445. https://doi.org/10.1016/j.cej.2021.134445.
147. Goyal, H.; Mehdad, A.; Lobo, R.F.; Stefanidis, G.; Vlachos, D.G. Scaleup of a Single-Mode Microwave Reactor. *Ind. Eng. Chem. Res.* **2019**, *59*, 2516 – 2523. https://doi.org/10.1021/acs.iecr.9b04491.
148. Sturm, G.S.J.; Verweij, M.D.; Van Gerven, T.; Stankiewicz, A.I.; Stefanidis, G. On the effect of resonant microwave fields on temperature distribution in time and space. *Int. J. Heat Mass Transf.* **2012**, *55*, 3800 – 3811. https://doi.org/10.1016/j.ijheatmasstransfer.2012.02.065.
149. Chen, T.-Y.; Baker-Fales, M.; Vlachos, D.G. Operation and Optimization of Microwave-Heated Continuous-Flow Microfluidics. *Ind. Eng. Chem. Res.* **2020**, *59*, 10418 – 10427. https://doi.org/10.1021/acs.iecr.0c01650.
150. Malhotra, A.; Chen, W.; Goyal, H.; Plaza-Gonzalez, P.J.; Julian, I.; Catala-Civera, J.M.; Vlachos, D.G. Temperature Homogeneity under Selective and Localized Microwave Heating in Structured Flow Reactors. *Ind. Eng. Chem. Res.* **2021**, *60*, 6835 – 6847. https://doi.org/10.1021/acs.iecr.0c05580.
151. Robinson, J.; Kingman, S.; Irvine, D.; Licence, P.; Smith, A.; Dimitrakis, G.; Obermayer, D.; Kappe, C.O. Electromagnetic simulations of microwave heating experiments using reaction vessels made out of silicon carbide. *Phys. Chem. Chem. Phys.* **2010**, *12*, 10793 – 10800. https://doi.org/10.1039/c0cp00080a.
152. Sanz-Moral, L.M.; Navarrete, A.; Sturm, G.; Link, G.; Rueda, M.; Stefanidis, G.; Martín, Á. Release of hydrogen from nanoconfined hydrides by application of microwaves. *J. Power Sources* **2017**, *353*, 131 – 137.
153. Nigar, H.; Sturm, G.S.J.; Garcia-Baños, B.; Peñaranda-Foix, F.L.; Catalá-Civera, J.M.; Mallada, R.; Stankiewicz, A.; Santamaría, J. Numerical analysis of microwave heating cavity: Combining electromagnetic energy, heat transfer and fluid dynamics for a NaY zeolite fixed-bed. *Appl. Therm. Eng.* **2019**, *155*, 226 – 238.

154. Nechanicky M.A., Chew K.W., Sellinger A., Laine R.M., α-Silicon carbide/β-silicon carbide particulate composites via polymer infiltration and pyrolysis (PIP) processing using polymethylsilane, *J. Eur. Ceram. Soc.* **2000**, *20 (4)*, 441-451. https://doi.org/10.1016/S0955-2219(99)00177-6
155. Meloni E., Palma V., Vaiano V., Optimized microwave susceptible catalytic diesel soot trap, *Fuel* **2017**, *205*, 142 – 152 http://dx.doi.org/10.1016/j.fuel.2017.05.074
156. Zeppieri M., Villa P.L., Verdone N., Scarsella M., De Filippis P., Kinetic of methane steam reforming reaction over nickel- and rhodium-based catalysts, *Applied Catalysis A: General*, **2010**, *387 (1–2)*, 147-154. 10.1016/j.apcata.2010.08.017
157. Meloni, E., Martino, M., Palma, V. Microwave assisted steam reforming in a high efficiency catalytic reactor, Renew. Energy **2022**, *197*, 893 – 901. Doi: 10.1016/j.renene.2022.07.157
158. Fusen Zhang, Xiaorong Zhang, Zhanlong Song, Haoran Chen, Xiqiang Zhao, Jing Sun, Yanpeng Mao, Xujiang Wang, Wenlong Wang, Fe/HZSM-5 synergizes with biomass pyrolysis carbon to reform CH_4-CO_2 to syngas in microwave field, *Int. J. Hydrogen Energy* **2022**, *47*, 11153 - 11163
159. Chris M. Marin, Eric J. Popczun, Thuy-Duong Nguyen-Phan, De Nyago Tafen, Dominic Alfonso, Iradwikanari Waluyo, Adrian Hunt, Douglas R. Kauffman, Designing perovskite catalysts for controlled active-site exsolution in the microwave dry reforming of methane, *Appl. Catal., B* **2021**, *284*, 119711
160. Hoang M. Nguyen, Gia Hung Pham, Moses Tade, Chi Phan, Robert Vagnoni, Shaomin Liu, Microwave-Assisted Dry and Bi-reforming of Methane over M−Mo/TiO_2 (M = Co, Cu) Bimetallic Catalysts, *Energy Fuels* **2020**, *34*, 7284−7294
161. Ran Li, Wentao Xu, Jie Deng, Jicheng Zhou, Coke-Resistant Ni−Co/ZrO_2−CaO-Based Microwave Catalyst for Highly Effective Dry Reforming of Methane by Microwave Catalysis, *Ind. Eng. Chem. Res.* **2021**, *60*, 17458−17468
162. Renda, S., Cortese, M., Iervolino, G., Martino, M., Meloni, E., Palma, V., Electrically driven SiC-based structured catalysts for intensified reforming processes, *Catal. Today* **2022**, *383*, 31 – 43. doi: 10.1016/j.cattod.2020.11.020
163. T. Yabe, K. Mitarai, K. Oshima, S. Ogo, Y. Sekine, Low-temperature dry reforming of methane to produce syngas in an electric field over La-doped Ni/ZrO_2 catalysts, *Fuel Processing Technology* **2017**, *158*, 96 - 103.

164. Y. Sekine, M. Haraguchi, M. Matsukata, E. Kikuchi, Low temperature steam reforming of methane over metal catalyst supported on $Ce_xZr_{1-x}O_2$ in an electric field, *Catal. Today* **2011**, *171*, 116 - 125
165. Lei Zheng, Matteo Ambrosetti, Daniele Marangoni, Alessandra Beretta, Gianpiero Groppi, Enrico Tronconi, Electrified methane steam reforming on a washcoated SiSiC foam for low-carbon hydrogen production, *AIChE J.* **2022**, 17620. Doi: 10.1002/aic.17620